Quantitative Analysis of He Enrichment Processes in Peridotite Shear Zones through Sample Analyses and Numerical Modeling

A Thesis
Presented in Partial Fulfillment of the Requirements for the
Degree of Master of Science
with a
Major in Geology
in the
College of Graduate Studies
University of Idaho
by

Kate M. Kaminski

Major Professor: Eric Mittelstaedt, Ph.D.
Committee Members: Mark Kurz, Ph.D.; Jessica Warren, Ph.D.
Department Administrator: Mickey Gunter, Ph.D.

December 2016

Authorization to Submit Thesis

This thesis of Kate Kaminski, submitted for the degree of Master of Science with a Major in Geology and titled "Quantitative Analysis of He Enrichment Processes in Peridotite Shear Zones through Sample Analyses and Numerical Modeling," has been reviewed in final form. Permission, as indicated by the signatures and dates below, is now granted to submit final copies to the College of Graduate Studies for approval.

Major Professor: _____ Date: _____
Eric Mittelstaedt, Ph.D.

Committee Members: _____ Date: _____
Jessica Warren, Ph.D.

_____ Date: _____
Mark Kurz, Ph.D.

Department
Administrator: _____ Date: _____
Mickey Gunter, Ph.D.

Abstract

Recent studies of ductile shear zones in the Josephine Peridotite (SW Oregon) find higher helium concentrations in whole rock samples located where total strain is greatest and recrystallized grain sizes are smallest. Based upon these results, previous workers suggest that dynamic recrystallization may create new inter-grain voids where He can be stored. To assess the feasibility of this mechanism for enhanced He storage, we utilize a combined set of new and previous data from Shear Zones A and B of the Fresno Bench outcrop to constrain a 1D numerical model of a ductile shear zone; the combined data set includes both He concentrations as well as measured total strain across the shear zone. Our numerical model is discretized using finite differences and incorporates a non-linear, temperature-dependent viscosity, shear heating, and dynamic recrystallization. The numerical model results produce similar helium concentration profiles to those of the Josephine shear zones, but comparison of both data sets suggests that deformation occurred much more rapidly than we originally suspected. Our model provides useful insight into the incompatible diffusive behavior of helium in mantle shear zones and suggests possible mechanisms of helium enrichment in high-strain mantle material.

Acknowledgements

I wish to thank, first and foremost, my advisor Eric Mittelstaedt for his continued mentorship, guidance, and wisdom, and for providing me with incredible opportunities for educational growth during my time at the University of Idaho. My committee members, Mark Kurz and Jessica Warren, provided me with unlimited insight and advice, and they had a significant influence in the formation of this project. I would also like to thank Katie Kumamoto at Stanford University, Josh Curtice and the Isotope Geochemistry Facility at Woods Hole Oceanographic Institution, and Owen Neill at Washington State University for their assistance in data acquisition and sample processing. Finally, my heartfelt gratitude goes to the University of Idaho department of Geological Sciences for providing me with an invaluable education and research experience.

Table of Contents

List of Figures

List of Tables

1. Introduction

Noble gases in mantle rocks act as tracers of melt transport, mantle degassing, and mantle sources, offering insights into the dynamics of geologic systems (*Trull and Kurz*, 1993; *Burnard et al*., 2004; *Parman et al.*, 2005; *Shaw et al*., 2006; *Baxter et al*., 2007; *Heber et al*., 2007; *Thomas et al*., 2008; *Hart et al.*, 2008; *Davies*, 2010; *Pinilla et al.*, 2012; *Recanati et al.*, 2012; *Jackson et al.*, 2013; *Burnard et al.*, 2015). Mantle material, when erupted at the earth's surface, retains the noble gas signature of its source environment, providing the ability to trace the processes involved in the material's formation and transport (*Anderson*, 1998; *Farley and Neroda*, 1998; *Burnard et al*., 2004). In such exposed upper mantle rocks, deviations from typical noble gas isotopic ratios and concentrations indicate noble gas input from another source. To attempt to gain a deeper understanding of mantle processes, it is necessary to identify and study these anomalies.

The noble gas signature of upper mantle material erupted at mid-ocean ridges is well known (e.g., *Anderson*, 1998; *Farley and Neroda*, 1998; *Ballentine et al*., 2002; *Graham*, 2002; *Kurz et al*., 2009; *Recanati et al*., 2012), but noble gas anomalies have been found to occur in ductile mantle shear zones (e.g., *Kurz et al*., 2009; *Recanati et al.*, 2012). It is suspected that the presence of melt channels in the center of mantle shear zones (*Kelemen and Dick*, 1995) could alter the noble gas signature of erupted mantle material; incompatible noble gases, during mantle residence, will preferentially diffuse into a melt (*Farley and Neroda*, 1998; *Burnard*, 2004). This melt, if erupted on the surface, will be relatively enriched in noble gases compared to its source material, potentially causing samples to be unrepresentative of the upper mantle.

Helium is often used to understand mantle processes and sources of mantle rocks (*Anderson*, 1998; *Farley and Neroda*, 1998; *Honda and Patterson*, 1999; *Ballentine et al*., 2002; *Graham*, 2002). Thus, it is essential to understand all processes that alter the He concentration of mantle rocks before they reach the surface. One such process is the evolution of helium in ductile shear zones (i.e. *Warren et al*., 2008; *Kurz et al*., 2009; *Recanati et al*., 2012), where previous observations find that concentrations of noble gases increase with the deformation in mantle shear zones (*Kurz et al*., 2009; *Recanati et al*., 2012; *Jackson et al*., 2013). Increasing helium enrichment with increasing accumulated shear strain suggests the

existence of a mechanism for preferential transport of helium atoms toward zones of deformation.

This study seeks to investigate the potential mechanisms of helium diffusion and enrichment within small-scale ductile mantle shear zones. Experimental studies attribute observed larger helium concentrations in more deformed rocks to reduced grain size and, thus, increased grain boundary volumes, into which helium preferentially diffuses (*Hiraga et al.*, 2004; *Baxter et al*., 2007; *Burnard et al*., 2015). Dry grain boundaries likely provide long-term storage for noble gas atoms due to slow diffusion rates (*Baxter et al*., 2007), but wet grain boundaries (e.g., filled with melt), create "fast paths" for diffusion and quickly remove helium in the presence of a concentration gradient (*Trull and Kurz*, 1993; *Burnard*, 2004; *Watson and Baxter*, 2007; *Dohmen and Milke*, 2010).

To assess the role of the above mechanisms in forming sharp He concentration gradients in ductile mantle shear zones, we present analysis of samples from two harzburgite shear zones of the Josephine Peridotite. These data provide constraints on a 1D numerical model of a ductile shear zone. This work is an extension of the work of *Recanati et al*. (2012), which investigates the relationship between deformation and helium content in widely spaced (~1 m) samples across Shear Zone A (SZ A) of the Josephine Peridotite; we combine their results with our analyses of new, high spatial resolution (~5 cm) samples to expand upon their analysis of the behavior of helium within high-strain regions of shear zones. Our new data reveal a previously unresolved He concentration pattern in which peridotite bordering the shear zone is depleted relative to the centers of SZ A and SZ B, suggesting that He enrichment in shear zone centers may reflect stripping of He through diffusion of He atoms from neighboring rock.

2. Background

2.1 Previous peridotite noble gas studies

Ophiolites, obducted portions of the oceanic lithosphere, provide important constraints on lithosphere structure and mantle dynamics (*Harper*, 1984). Peridotite, the lowermost layer of ophiolites, is thought to be comprised primarily of upper mantle material. Thus, olivine, the primary mineral of peridotite, is valuable in noble gas studies (e.g., *Harper*, 1984; *Coulton et al.*, 1995; *Warren et al.*, 2008; *Sundberg et al.*, 2010; *Recanati et al.*, 2012; *Hansen et al.*,

2015). Peridotites, and other rocks formed at mid-ocean ridges, retain helium and other noble gas signatures of their source, providing the ability to determine the origin of mid-ocean ridge material and the formation and deformation of ophiolites and mid-ocean ridge basalts (*Honda and Patterson*, 1999; *Burnard et al*., 2004; *Kurz et al*., 2009). While the overall behavior of helium is well studied, there exists little data (beyond that cited below) on helium diffusion and storage solely in peridotites, which makes a study such as this one particularly useful in the investigation of mantle dynamics.

Noble gas measurements of samples from *Kurz et al*. (2009), *Recanati et al*. (2012), and *Jackson et al*. (2013) demonstrate total helium concentrations in basalts and peridotites that vary from 10^{-7} to 10^{-10} cc ^{4}He g^{-1}; these differences in He concentration have little correlation with measurement type (i.e., mineral separates vs. whole rock), but a significant correlation with degree of deformation of the host rock. For example, *Jackson et al*. (2013) measured total helium concentrations in olivine mineral separates of undeformed peridotites and found concentrations of 9.6×10^{-10} to 2.6×10^{-8} mol He/g. *Recanati et al*. (2012) also performed whole rock and mineral separate analyses (olivine and pyroxene) and found a median He concentration of 5.6×10^{-8} cc ^{4}He/g with insignificant differences between whole rock and mineral separate measurements (±0.63 cc ^{4}He/g, with whole rock samples typically more enriched in ^{4}He). In contrast to the lack of compositional control on He content, *Recanati et al*. (2012) find an anomalously high He concentration of 1.2×10^{-7} cc ^{4}He/g in the most deformed sample from the center of a peridotite shear zone. Similarly, *Kurz et al*. (2009) studied the helium content in natural peridotite samples exhibiting varying amounts of deformation. They report increasing He concentrations with deformation from 6.2×10^{-9} to 3.6×10^{-8} cc ^{4}He/g for protogranular and porphyroclastic peridotites to 5×10^{-8} and 4.4×10^{-7} cc ^{4}He/g in mylonites and ultramylonites. Although the above observations consistently find increasing He concentration in peridotites with increasing deformation, the processes controlling this enrichment are unclear.

2.2 Paths of diffusion

Noble gases can move independently from solid mantle flow via transport through defects in crystal lattices (point defects and dislocation defects) and fluids in grain boundaries (Fig. 1) (*Fisher*, 1951; *Poirier*, 2005; *Watson and Baxter*, 2007). Point defects, or atomic

vacancies, are voids in the crystal lattice through which atoms can migrate by jumping between sites (*Watson and Baxter*, 2007; *Dohmen and Milke*, 2010). Transport between point defects is slow and the defects act as slow paths of diffusion (*Watson and Baxter*, 2007; *Dohmen and Milke*, 2010). In contrast, dislocation defects (1D features created through deformation of grains by an applied stress, creating voids in the crystal lattice) provide fast diffusion paths along which atoms may migrate (*Poirier*, 2005; *Watson and Baxter*, 2007; *Watson and Baxter*, 2010). In addition to defects in the crystal structure, atoms can diffuse across grain boundaries, features of oriented dislocation defects separating crystals of differing lattice orientation. When wetted by melt or fluids, these boundaries also provide fast diffusion paths (*Poirier*, 2005; *Watson and Baxter*, 2007; *Karato*, 2008; *Watson and Baxter*, 2010).

The rate at which helium atoms diffuse along fast and slow paths differs by several orders of magnitude. Due to differences in activation energies, diffusion within mineral lattices and dry grain boundaries is slower than across or along wetted grain boundaries or defects (*Trull and Kurz*, 1993; *Baxter et al*., 2007; *Watson and Baxter*, 2007; *Dohmen and Milke*, 2010; *Jackson et al*., 2013). Diffusion rates differ significantly between these paths due to differences in activation energy. Grain boundary diffusion has a lower activation energy than lattice diffusion, although particular values are disputed (*Dohmen and Milke*, 2010; *Jackson et al*., 2013; *Burnard et al.*, 2015). The lower energy required for grain boundary diffusion yields larger diffusive length scales, meaning that helium particles diffuse further through grain boundaries than in lattice diffusion over the same time (*Jackson et al*., 2013). Diffusion rates within grain boundaries are also controlled by the composition of the intergranular transporting material (ITM), including the particular combination of fluid phases (e.g., melt or aqueous fluid), gas phases (bubbles), and dry grain boundaries (non-wetted) (*Baxter et al.*, 2007; *Watson and Baxter*, 2007). The presence of any melt within grain boundaries will increase the rate of diffusion and, if enough melt volume is present, will create a series of interconnected fast paths, allowing for rapid diffusion of helium (*Trull and Kurz*, 1993; *Baxter et al*., 2007; *Watson and Baxter*, 2007).

2.3 Residence sites of gases

There are several potential sites within a polycrystalline rock where gas atoms can be stored: (1) fluid or melt inclusions, (2) 1D and 2D defects, and (3) grain boundaries (*Watson and Baxter*, 2007).

1) Fluid or melt inclusions within mineral grains trap available gas atoms in pockets of fluid during recrystallization. In the mantle, helium and other noble gases are frequently trapped in these inclusions (*Trull and Kurz*, 1993; *Shaw et al*., 2006). *Kurz et al*. (2009) and *Recanati et al*. (2012) found that <21% of the total helium within deformed peridotite from the Josephine Peridotite and St. Paul's rocks is stored in melt and fluid inclusions, as interpreted from crushing vs. melting experiments (discussed further in section 3.2).
2) 1D and 2D defects include dislocations and subgrain boundaries, which are constantly created and removed from the crystal structure during deformation (*Baxter et al.*, 2007; *Watson and Baxter*, 2007; *Dohmen and Milke*, 2010). As deformation proceeds, defects form and increase the total stored strain energy within the material. Upon reaching sufficient stress and strain, reduction in grain size by dynamic recrystallization reduces elastic strain stored by individual grains and ultimately erases existing defects. Some studies suggest that samples with high dislocation densities are likely to have high noble gas contents (*Heber et al*., 2007; *Burnard et al*., 2015).
3) Grain boundaries can act as either fast or slow diffusion paths; the presence of a melt will enhance the rate of diffusion. In contrast, He diffuses extremely slowly through dry grain boundaries, which results in long noble gas residence times (~5.6 ky across 0.75 nm wide grain boundaries) (*Burnard*, 2004; *Baxter et al*., 2007; *Dohmen and Milke*, 2010). For dry grain boundaries, reduction in grain size via dynamic recrystallization will create a larger volume of grain boundaries than in relatively undeformed, coarse-grained rocks (*Kurz et al.*, 2009; *Recanati et al*., 2012; *Burnard et al.*, 2015), perhaps providing locations to store large volumes of gases (*Hiraga et al.*, 2004; *Baxter et al.*, 2007).

Gases may be distributed amongst the above three storage locations. However, long-term residence is likely only possible within inclusions and the grain matrix (and, potentially, dry grain boundaries); gases stored in other sites will quickly diffuse away.

2.4 Dynamic recrystallization

Four primary mechanisms control deformation of materials in the ductile regime: diffusion creep, dislocation creep, Peierls creep, and dislocation-accommodated grain boundary sliding (*Hirth and Kohlstedt*, 2003). Each mechanism changes a polycrystalline material's steady-state grain size (*De Bresser et al*., 1998; *Herwegh et al*., 2008). Materials in the diffusion creep regime (low stress, small grain size) undergo grain growth, while materials in the dislocation creep regime (high stress, large grain size) undergo grain size reduction (Fig. 3; *Karato*, 1989; *Braun et al*., 1999; *De Bresser et al*., 2001; *Yamasaki*, 2004; *Shimizu*, 2008; *Faul et al.*, 2011; *Linckens et al.*, 2014). Peierls creep, or low-temperature plasticity, occurs at low temperatures and high stresses, over a wide range of initial grain sizes, and can lead to either grain size reduction or growth (*Faul et al*., 2011). Dislocation-accommodated grain boundary sliding (disGBS) occurs in temperature and pressure conditions between grain size-sensitive diffusion creep and grain size-insensitive dislocation creep and is believed to create a dynamic balance between grain size reduction and growth (*Warren and Hirth*, 2006; *Faul et al.*, 2011; *Hansen et al*., 2011). All of the above mechanisms, excepting Peierls creep, commonly occur in deforming mantle rocks.

Grain size reduction in both the dislocation creep and disGBS regime occur through dynamic recrystallization, driven by energy stored in dislocations within grains (*Karato*, 1989). Dynamic recrystallization occurs by one of three processes: rotation, migration, and bulging of grain and subgrain boundaries (*Urai et al*., 1986; *De Bresser et al*., 2001; *Yamasaki*, 2004; *Shimizu*, 2008; *Faul et al*., 2011; *Linckens et al*., 2014). Rotation recrystallization results when new grain or subgrain boundaries form at angles larger than a critical angle Θ_c = 10-15° (*Shimizu*, 2008). The high angles cause new, low-strain grains to form through the misorientation of subgrains, although the amount of grain growth that occurs is minimal (*De Bresser et al*., 2001; *Karato*, 2008; *Shimizu*, 2008). Migration recrystallization occurs when existing grain boundaries migrate and coalesce, creating new grains through consumption of neighboring grains (*De Bresser et al.*, 2001). In this case, a

grain boundary migrates to an area of higher dislocation density and, as the boundary passes through a pre-existing grain, it leaves behind a low-strain region with few dislocations (*Karato*, 2008). Grain boundary bulging is the result of increased strain. The grain edge bends outward, creating a potential nucleus site for a new grain. Grain growth then occurs at the expense of neighboring grains, resulting in an overall decrease in grain size and a reduction in stored strain energy (*Shimizu*, 1998, 2008).

2.5 Previous models of grain size evolution

There are several models describing grain size evolution in ductile deformation. The general law for grain size evolution involves both grain growth and grain size reduction terms, and the sum of these values will determine the dominant process. Three of the major variations on the grain size evolution law are field boundary (FB), modified field boundary (mFB), and continuous recrystallization (CRX) (*Montési and Hirth*, 2003). The FB theory determines whether the system is in the grain growth or reduction regime by calculating strain rate due to diffusion and dislocation creep individually and comparing their ratio to a critical ratio R_c: if $\dot{\varepsilon}_{disl}/\dot{\varepsilon}_{diff} < R_c$, deformation conditions fall within the diffusion creep regime and grain size increases; if $\dot{\varepsilon}_{disl}/\dot{\varepsilon}_{diff} > R_c$, dislocation creep occurs and grain size decreases through dynamic recrystallization (*Montési and Hirth*, 2003). The mFB theory is similar to FB, but determines grain size evolution based upon the current grain size *d* instead of the ratio of strain rates. If $d < D$, grain growth will occur, and if $d > D$, recrystallization will occur (*Montési and Hirth*, 2003). In contrast to FB and mFB, which assume that grain size reduction and growth are exclusive, CRX assumes that the two mechanisms occur simultaneously and grain size will evolve towards its equilibrium grain size *D* (*Hall and Parmentier*, 2003; *Montési and Hirth*, 2003).

2.6 The Josephine Peridotite

The Josephine Peridotite is located within the Rogue River Siskiyou National Forest (42º 17.03 N, 123º 97.95 W) and is a unit of the Western Klamath Terrane, which extends from southwestern Oregon to northern California (*Harper*, 1984; *Evans*, 1987; *Harper et al*., 1994; *Miller and Saleeby*, 1995). The Josephine Peridotite is part of an incomplete ophiolite sequence (i.e., it does not include a crustal or gabbro section common in ophiolites) and is

composed primarily of harzburgite tectonite with lesser dunite (*Harper*, 1984; *Coulton et al*., 1995). The harzburgite is composed primarily of olivine (~60-70%) with 10-30% orthopyroxene, 0-5% clinopyroxene, and < 2% chromian spinel (*Harper*, 1984; *Recanati et al*., 2012). Within the harzburgite, olivine grains commonly range in size from 0.25-6 mm or greater (*Harper*, 1984; *Evans*, 1987). Dunite appears throughout the harzburgite (< 10% by volume) as tabular bodies and dikes, small patches, or large pods up to 0.5 km^2 (*Harper*, 1984). On average, 50% or fewer of sampled peridotites are serpentinized, with the most altered peridotites found in regions of heavy faulting and shearing (*Harper*, 1984; *Coulton et al*., 1995).

The Josephine Peridotite formed in a volcanic arc along western North America in the Middle Jurassic and was later obducted onto the western edge of the continent. Formation ages of the peridotite itself are 164-162 Ma as determined by Pb/U and $^{40}Ar/^{39}Ar$ geochronology (*Harper et al*., 1988; *Harper et al*., 1994; *Coulton et al*., 1995). From 155-135 Ma, the Nevadan orogeny deformed and uplifted the region, causing the entire ophiolite to underthrust western North America (*Harper et al*., 1994; *Coulton et al*., 1995). The ages of the shear zones of the Josephine Peridotite are not well-constrained, but it seems that shearing most likely occurred during the major deformation and metamorphic phases initiated after emplacement. The first deformation phase occurred 155-150 Ma, which involved significant displacement along both the Orleans and Madstone Cabin thrusts (*Harper et al*., 1988; *Harper et al*., 1994). The second phase of deformation occurred after the Nevadan orogeny 145-135 Ma and is evident in the very large-scale folding of the Josephine, with an average wavelength of 15 km (*Harper et al*., 1994). The widespread deformation was followed directly by an intrusive magmatic phase ~135 Ma, producing coarse-grained orthopyroxenite and metagabbro dikes that crosscut the entire unit (*Harper*, 1984).

High-temperature deformation is evident in the Josephine Peridotite on the grain scale. Individual olivine grains display deformation in kink bands on grain boundaries, and the presence of small, polygonal olivine grains may indicate recrystallization (*Harper*, 1984). Estimates suggest that the observed deformation within the peridotite occurred at an average of 1150 ºC (*Evans*, 1987).

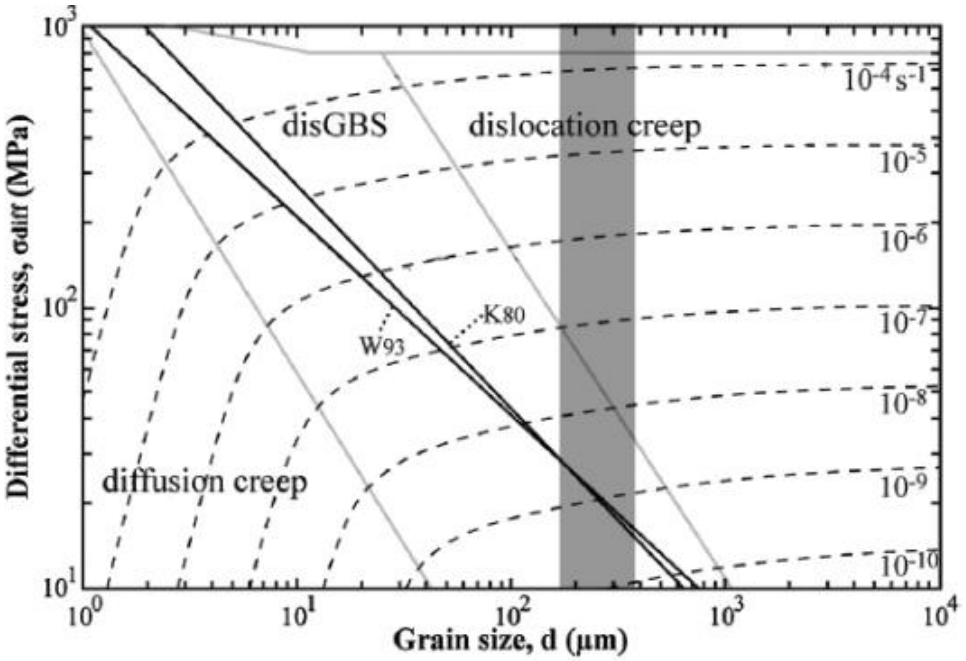

Figure 1. Olivine deformation map at 1227 ºC (1500 K) (from *Linckens et al*., 2014). Boundary values used to constrain each field are reported in Table 2. Mechanism regimes, outlined by solid gray lines, are defined by flow laws from *Hansen et al*. (2011) and *Hirth and Kohlstedt* (2003). Dashed lines are constant strain rates and black solid lines are olivine grain size piezometers by *Karato et al*. (1980) (K_{80}) and *Van der Wal et al*. (1993) (W_{93}). The gray box outlines approximate post-deformation conditions of the Josephine Peridotite.

2.7 Isotopic ratios

Generally, helium isotopic ratios (reported as R/R_A: R = sample $^3He/^4He$, R_A = standard air $^3He/^4He$) in mantle peridotites (~6-7 Ra) are similar to those of MORBs (~7-9 Ra) (*Anderson*, 1998; *Farley and Neroda*, 1998; *Ballentine et al*., 2002; *Graham*, 2002; *Kurz et al*., 2009; *Recanati et al*., 2012). Similar He isotopic ratios are observed in the Josephine Peridotite. Previous work within SZ A shows similar measured $^3He/^4He$ values in both whole rock (6.6 Ra) and mineral separates (6.7 Ra) of olivine and pyroxene (*Recanati et al*., 2012). Comparable values in both olivine and pyroxene indicate that helium isotopes do not preferentially partition to particular mineral phases within the Josephine Peridotite. Studies determined that melting experiments generally yield higher $^3He/^4He$ values than crushing, suggesting that there is more cosmogenic He present in mineral matrices than grain boundaries (*Kurz et al*., 2009; *Recanati et al*., 2012). Overall, however, the cosmogenic helium contribution is small and helium in the above Josephine samples is mostly of mantle origin (*Kurz et al*., 2009; *Recanati et al*., 2012).

3. Methods

This study utilizes both experimental methods and observations in addition to a numerical model in an attempt to constrain deformation and helium enrichment in mantle shear zones. The combination of various methods of geochemical analysis and modeling allows constraints to be placed on possible mechanisms for helium transport and storage in areas of high strain.

3.1 Sample collection and preparation

To isolate the effect of deformation on He enrichment, this study focuses on shear zones within the Josephine Peridotite due to their relatively homogeneous harzburgite lithology (e.g., *Kelemen and Dick,* 1995; *Warren et al*., 2008; *Recanati et al*., 2012, *Skemer*, 2013). The unit is composed primarily of harzburgite with interlayered dunite and occasional altered pyroxene veins, which provide indications of shear motion. Oriented drill core samples were collected across transects of two ductile shear zones within the Josephine Peridotite at the Fresno Bench outcrop. Cores were oriented normal to the observed shear motion, as indicated by pyroxenite foliation. Each core measures one to two inches in length and one inch in diameter, and was collected from either harzburgite or dunite, avoiding pyroxene vein lineations. Finer-grained samples marked the observed structural center of each shear zone, hereafter referred to as the "shear zone center" (as opposed to the geochemical center, as determined by helium content, discussed below).

In a previous study of the Josephine shear zones, *Recanati et al*. (2012) examined helium content and isotopic compositions in SZ A. They collected samples every ~1 m along a ~8.5 m transect of SZ A. Sample analysis revealed a peak in helium concentration (124.9 cc kg^{-1}) near the shear zone center (Fig. 11). However, the spatial resolution of the *Recanati et al*. (2012) samples was insufficient to assess detailed noble gas variations near this peak in He concentration. To determine variations in helium concentration near the center of SZ A, we collected new samples at ~5-10 cm intervals within the ~0.5 m-wide zone that brackets the shear zone center. Of the seven new sample cores discussed here, sample JP15-KnE-01A is a dunite (collected for compositional comparison) and JP15-KnE-02A to 07A are harzburgites (Fig. 3). Samples JP15-KnE-04A and 06A were not drilled directly adjacent to *Recanati et al*. samples, but are spaced approximately equidistant from the nearest samples on the spatial

plane perpendicular to the shear direction (referred to as the X plane). Before drilling, the trend and plunge of each sample were measured and recorded. Orientation of the shear plane was determined based on field observations and measurements (*Kumamoto,* personal communication) to be 045/90. The lineation plane indicated by pyroxenite foliation was measured at 045/50.

For comparison with SZ A, we analyzed samples from SZ B. These core samples were collected during a 2013 field study by J. Warren and colleagues, and were determined to be sufficient for our study (Fig. 4). The samples were collected along a ~7.25 m transect across the structural center of SZ B, at a mean sampling interval of 0.6 m. JP13-D34 is a dunite and is assumed to be at the center of the shear zone; all other samples are harzburgite. Shear plane orientation is 322/50 and lineation is 045/50.

In the laboratory, sample cores were reoriented and thin sections cut with the long axis parallel to shear motion and short plane normal to the shear plane. After cutting, doubly-polished thin section billets were once again reoriented to evaluate consistency between samples. The thin sections were used to quantify mineralogy, mineral modal compositions, identify microstructures, and characterize average grain size.

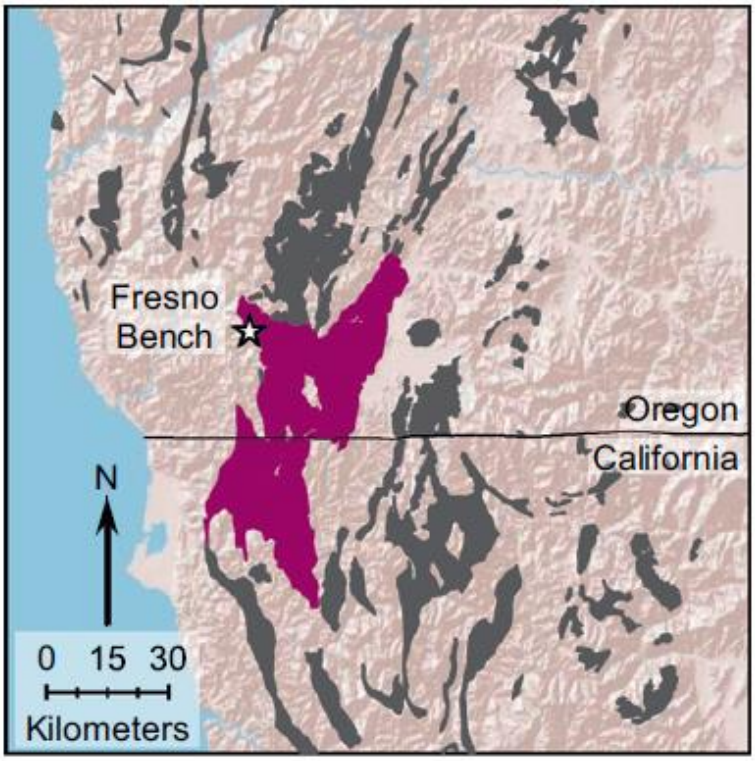

Figure 2. The Fresno Bench outcrop (highlighted in purple) within the Josephine Peridotite (from *Recanati et al*., 2012).

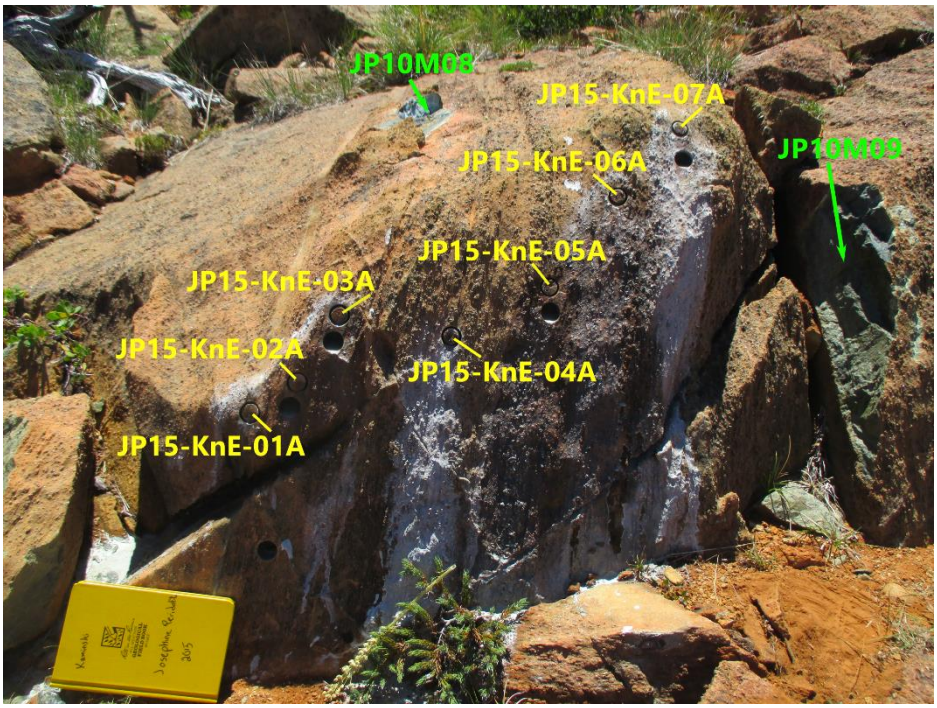

Figure 3. Shear zone A. Samples labeled in green are from *Recanati et al*. (2012). Samples in yellow were collected and analyzed in this study. Field observations place the shear zone center at approximately the location of JP10M08.

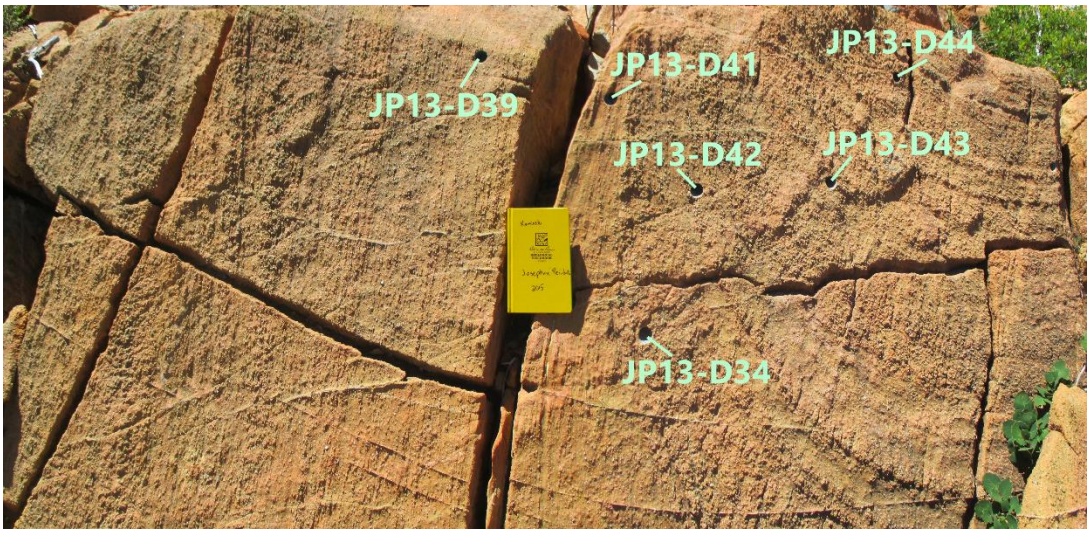

Figure 4. Shear zone B. Samples collected from 2013 field study are labeled in blue. The shear zone center is assumed to be to the right of the fracture, where sample JP13-D41 is located; a texture change is visible (harzburgite to dunite). Pyroxenite vein foliations show apparent shear motion.

3.2 Helium analysis

Whole rock bulk helium analyses were performed in the Isotope Geochemistry Facility at Woods Hole Oceanographic Institution (WHOI) following methods described by *Kurz et al*. (2004, 2009, 2014). Sample sizes obtained were too small to produce an adequate volume of olivine mineral separates; all analyses were performed on whole rock samples. Measurement of He content in our samples involved two steps: in-vacuo crushing to measure He stored in grain boundaries, followed by melting of the sample to measure He stored in inclusions and the grain matrix. To prepare samples for these analyses, whole rock pieces were chipped from samples using hammer and chisel and selected under binocular microscope to choose fractions that were unweathered and unaltered. We sonicated 200-300 mg of each sample in acetone for 15 minutes to remove oil and surface debris. Samples were then rinsed in distilled water and air-dried in a laminar flow hood. Chips were weighed and placed in stainless steel ultra-high vacuum crushers, in which they are crushed 20 to 40 times using a stainless steel slug and three electromagnets (*Kurz et al*., 1987). The resulting powders were packaged in aluminum foil boats and reweighed to account for lost volume. Each sample was then melted by heating to 1600 ºC in a double vacuum furnace. Total ^{4}He and $^{3}He/^{4}He$ were measured using the fully automated magnetic sector helium isotope mass spectrometer

(MS2) at WHOI. Blanks and air standards were simultaneously analyzed with samples. The helium data are reported relative to air standards (1.5×10^{-8} cc He, with air $^{3}He/^{4}He$ ratio of 1.384×10^{-6}). Results from these experiments are reported in Tables 2 and 3.

3.3 Thin section characterization

Back-scatter electron maps were made of selected samples (JP15-KnE-01A, -02A, -04A, -06A, -07A) using the JEOL 8500F field emission electron microprobe at Washington State University. Images were processed in MATLAB© to calculate modal abundances. Maps were converted to grayscale and minerals previously identified with optical microscopy were identified by their respective grayscale values. The proportion of each mineral was then calculated by integration of the area of each mineral and the mode given as a fraction of the total back-scatter map. Calculated values are reported in Table 6.

The mean grain size of each thin section was assessed using the stereology-based line-intercept method of *Lehto et al*. (2014; 2016), which statistically estimates 3D grain size. To facilitate identification of grain size, we isolated olivine grains in each BSE map by creating a binary image with olivine grains set to white and other minerals set to black. Through this threshold-based method, we assessed mean olivine grain size. The method of *Lehto et al*. (2014; 2016) measures the width of individual grains along four, uniformly spaced transects striking at 0º, 45º, 90º, and 135º relative to the top of the BSE image. This produces a distribution of grain size measurements, which is then used to calculate a probability function and standard deviation of mean grain size (Appendix A). These grain sizes are, however, approximations due to the fact that veins of serpentine often cross-cut olivine grains and may skew the average estimated grain size.

3.4 Shear strain calculations

To calculate total shear strain across each shear zone, we use pyroxene foliation measurements collected in the field. These foliation data are rotated and projected into the X-Z reference frame, which displays spatial data reoriented onto a plane parallel to shear direction (X-axis) and perpendicular to the shear plane (Z-axis) (*Warren et al*., 2008; *Recanati et al*., 2012). The result is a kinematic cross section of the shear zone, which allows us to reorient all samples with respect to JP10M08 and interpret shear motion (Fig. 5). These

projected planes are 315º/50º for SZ A and 322º/50º for SZ B (Appendix B). For both shear zones, center samples are sub-horizontal in the X-Z plane (parallel to the shear direction) at 1-2º.

Total shear strain across each shear zone is calculated using the change in foliation orientation in the projected reference frame. The shear strain ε is assessed as

$$\varepsilon = cot\,\alpha' - cot\,\alpha \qquad (1)$$

where α is the angle of the marker layer from horizontal and α' is the angle of the deflection angle of the deformed layers, measured counterclockwise from the shear plane (Fig. 6; *Ramsay and Graham*, 1970; *Warren et al*., 2008).

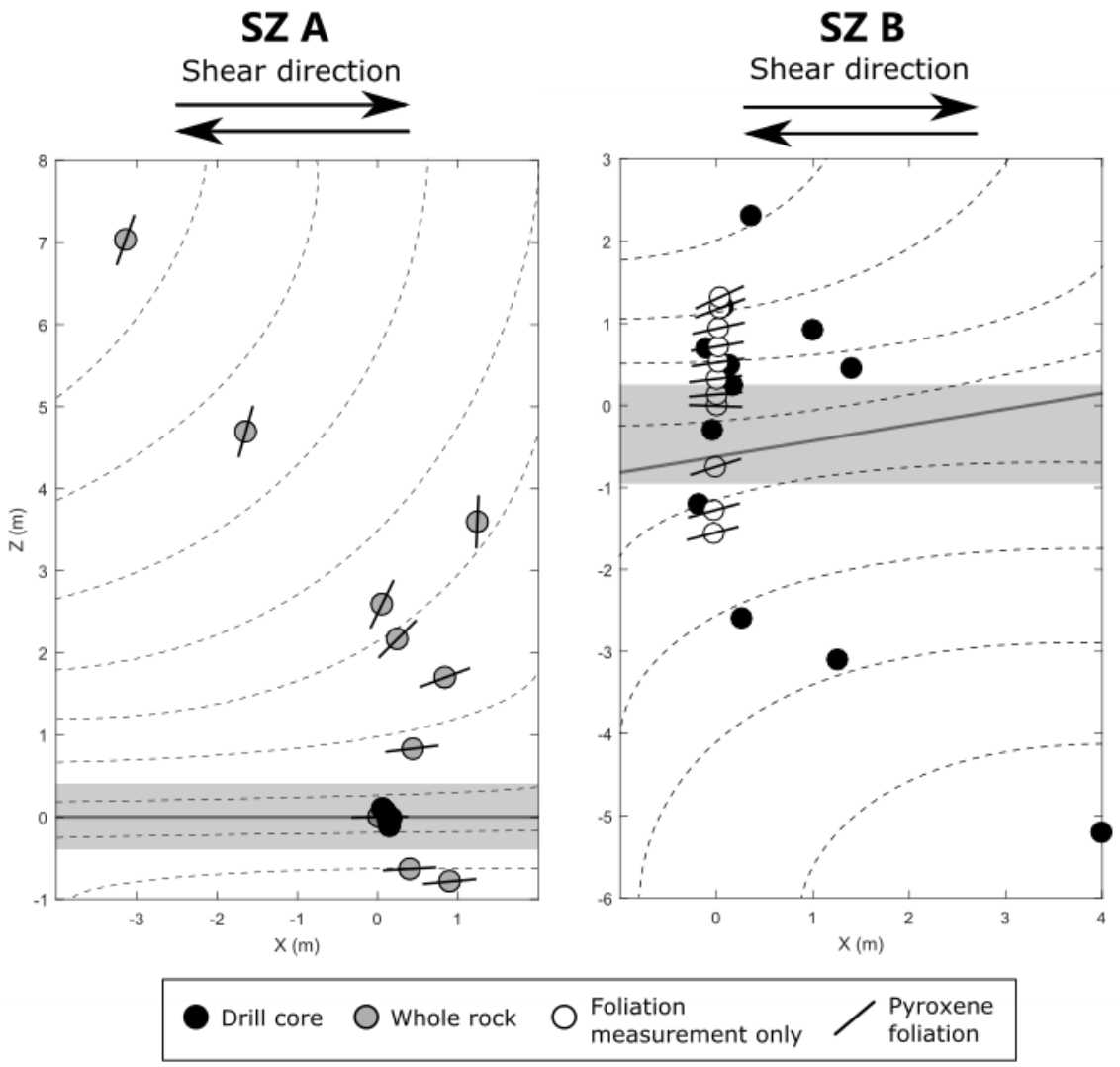

Figure 5. SZ A and B samples oriented in the kinematic reference frame provides an estimation of shear direction (dashed lines) using the orientation of pyroxene foliations (short, black lines). The dark gray, horizontal line at zero on the Z-axis is the shear plane (270/90 and 261/90, respectively), and the wide, gray bar denotes the shear zone center as defined by shear localization.

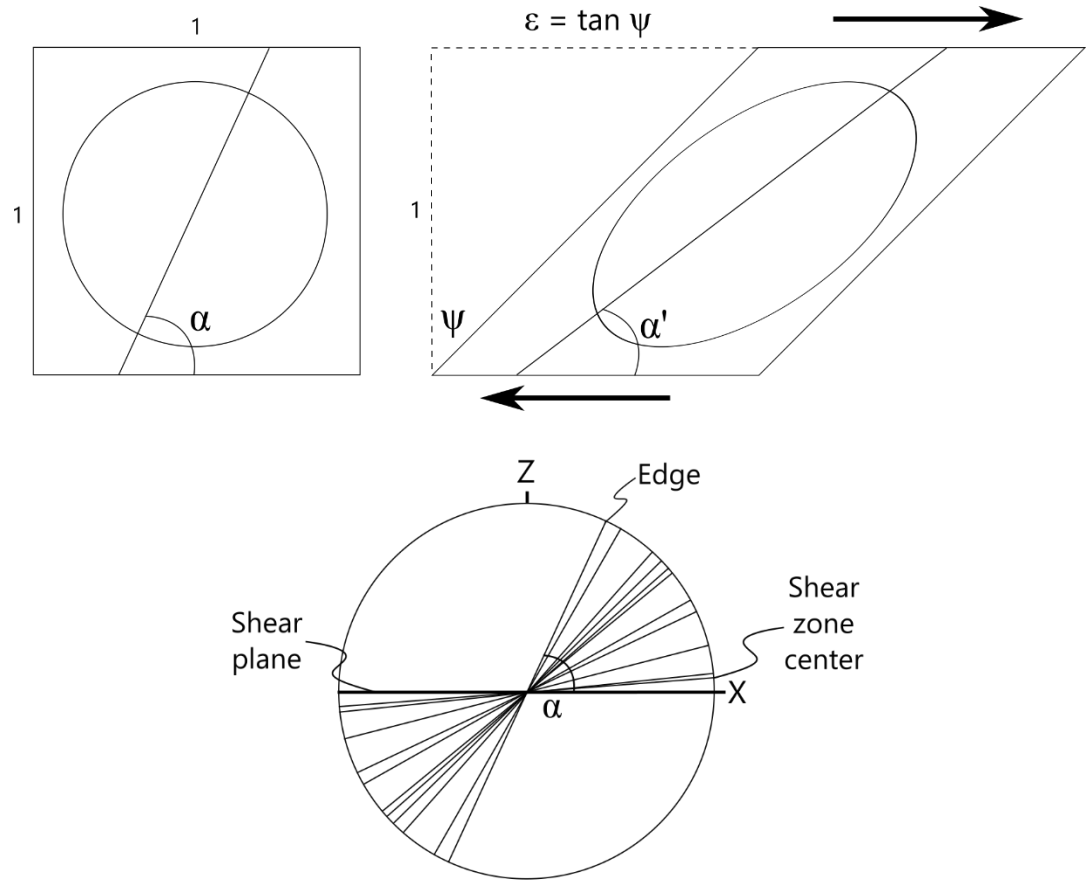

Figure 6. Conceptual illustration of the method used to determine deflection angle of pyroxene foliation as described in 3.3. The angle of deflection from the shear plane is calculated for the shear zone center (α) and deformed layers (α′), and used to calculate shear strain ε across the shear zone (after *Ramsay and Graham*, 1970; *Warren et al.*, 2008).

3.5 Conceptual model

To constrain processes that control He concentrations in SZs A and B, we develop a 1D numerical model based upon the following conceptual model of shear zone processes (Fig. 7). Initially, the shear zone is comprised of undeformed mantle material possessing the properties of a typical upper mantle peridotite (Table 1). Model boundaries are subjected to equal and opposite velocities to drive shear deformation. As deformation proceeds, reduction in the peridotite viscosity through shear heating, a non-linear dependence on strain rate (dislocation creep), and grain size reduction by dynamic recrystallization cause shear strain to localize to the shear zone center. The increased temperatures and localized deformation may result in the creation of a melt channel, which may act as a conduit for melt from the mantle (e.g., *Keleman and Dick*, 1995). Samples of dunite at the centers of both SZ A and SZ B support the presence of melt, as dunite forms through precipitation reactions in mantle melt

channels (dissolution of pyroxene and recrystallization of olivine; *Savelieva et al*., 2008). Helium is strongly incompatible and will preferentially enter the liquid phase, leaving the rock surrounding the melt channel depleted (*Farley and Neroda*, 1998; *Burnard*, 2004); this depletion of He from rock surrounding the melt channel creates a helium concentration gradient that will drive He diffusion toward the shear zone center. As long as deformation proceeds, at sufficiently high strain rates and temperatures, melt will remain in the shear zone center and He diffusion will persist, effectively stripping the neighboring rock of helium. Once deformation ceases, however, the system will cool, causing melt solidification and slowing of He diffusion. When the temperature falls below the helium closure temperature, the He concentration established during deformation will be retained. The resulting helium concentrations across the shear zone will be a function of the duration of shearing, the shear zone temperature, deformation localization and simultaneous decrease in grain size, and the grain size- and temperature-dependent rates of helium diffusion.

During deformation of the mantle shear zone, several processes will result from deformation in the disGBS and dislocation creep regimes, as indicated by the initial conditions of the Josephine Peridotite. A single helium atom residing in the crystal lattice of an olivine before deformation may be located in a fluid inclusion (Fig. 8, 9). The fluid inclusion is initially strain free, but deformation subjects the entire grain to increasing shear strain. In response to increasing strain accumulation, dislocations form within the grain interior, creating new, high-strain areas, into which the helium atom diffuses via point defects. Eventually, increasing elastic stresses within the grain reach the threshold to initiate dislocation creep. At this point, grain size reduction will proceed as the system tries to reduce the overall strain through the mechanisms of dynamic recrystallization, resulting in a reduction in average grain size and an increase in grain boundary volume. From the dislocation defect, which has been healed via recrystallization, the helium atom must then diffuse to another location, to either an inclusion in the newly formed grain or the ITM within a grain boundary. However, with a smaller grain size and increased total volume of grain boundaries, there is a greater chance that the atom will partition into the ITM.

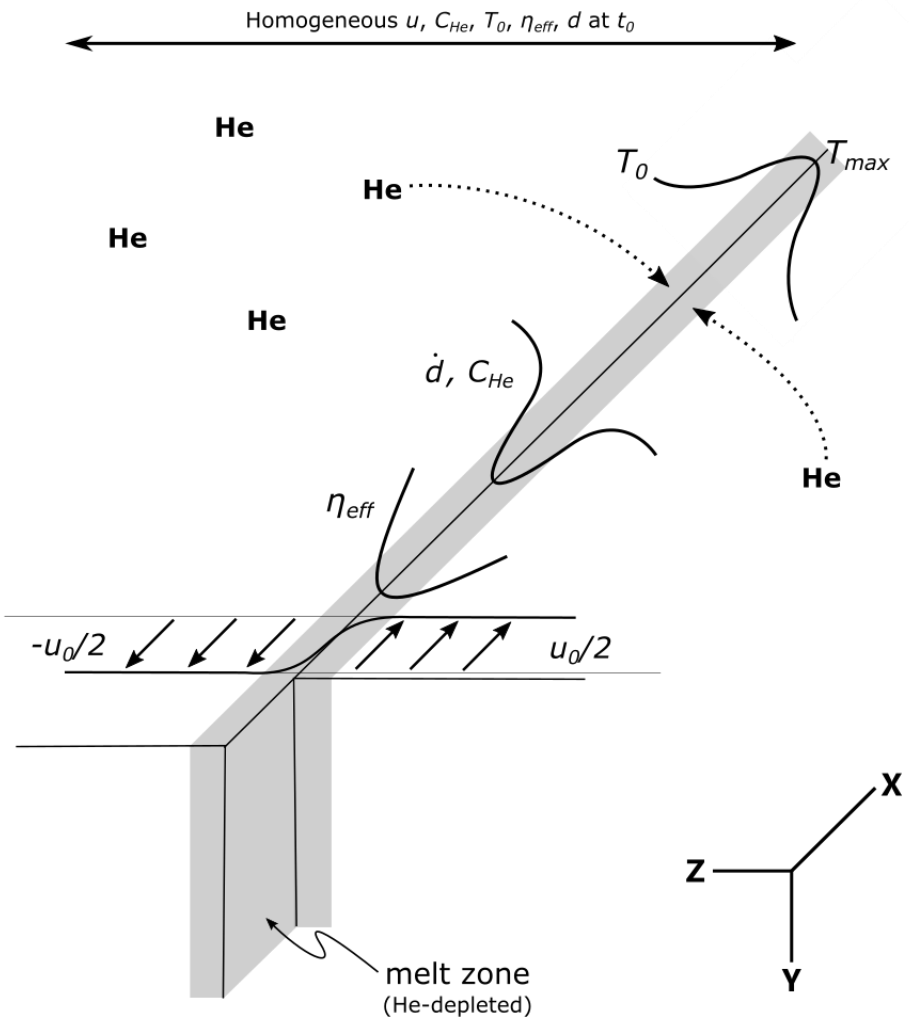

Figure 7. Cartoon of the shear zone model tested. The gray region is the shear zone center (similar to Fig. 10 and 11) where shear strain is highest and potentially containing a narrow melt channel which acts as a conduit for mantle fluids. Initially, the shear zone is characterized by total helium concentration (C_{He}), constant temperature (T_0), effective viscosity (η_{eff}), and grain size (d). Upon initiation of deformation, increased temperatures due to shear heating, the non-linear flow law, and decrease grain size cause strain localization at the shear zone center. The melt channel at the center acts as a helium sink and pulls He from the surrounding material. The resulting concentration gradient creates a melt enriched in He surrounded by a zone of sheared rock with significantly lower helium concentrations.

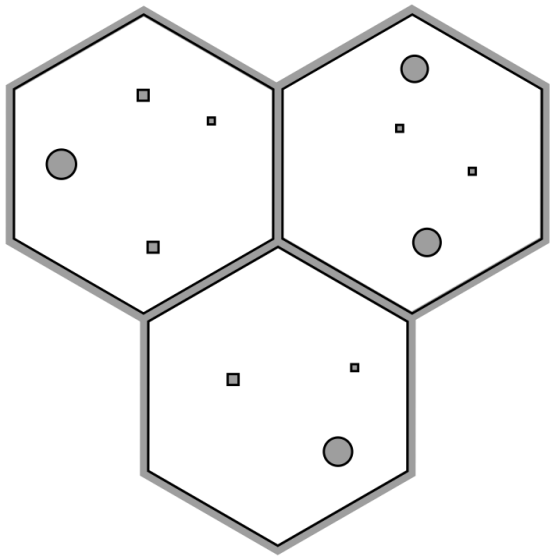

Figure 8. Inter- and intragrain storage sites in olivine grains. The white hexagons are schematic grains (the shape of olivine is mathematically approximated as tetrakaidecahedral) and the gray regions between grains represent the ITM (containing grain boundaries and, if present, fluid and/or gas phases). Filled gray circles within grain matrices are fluid inclusions and filled gray squares are point defects or dislocation defects. (After *Watson and Baxter*, 2007; *Hiraga and Kohlstedt*, 2009).

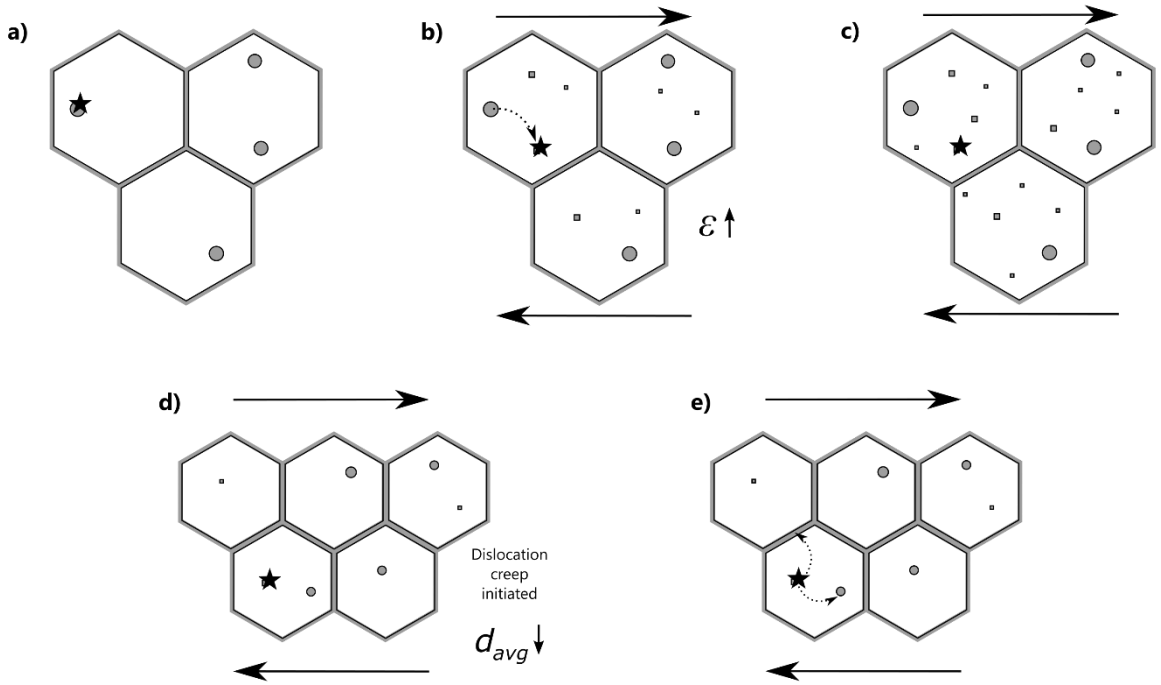

Figure 9. Cartoon of a potential path of a helium atom (black star) as described in section 3.5. Grain structure and features are the same as in Fig. 8. a) A helium atom is located in an inclusion. b) The mineral grains are subject to shear deformation (arrows), and shear strain, ε, accumulates resulting in the formation of more dislocations (gray squares). The helium atom diffuses into a nearby dislocation

where the strain energy is lower than in the inclusion. c) Dislocations continue to accumulate with increasing strain. d) Once strain reaches the maximum elastic strain and stress allowed by the material, the system will undergo dislocation creep deformation, as a means to reduce total strain. Mean grain size (d_{avg}) will decrease and dislocation defects will be "healed." e) Once dislocations are healed, the helium atom will diffuse to a new residence site, for example, a newly-formed inclusion or the grain boundary ITM.

3.6 Numerical modeling

We present a one-dimensional (1D) model of a ductile shear zone to quantify the roles of deformation, grain size evolution, shear heating, and diffusion on helium concentrations observed in shear zones A and B within the Josephine Peridotite. The model uses the MATLAB© "backslash" operator to solve the equations of conservation of mass, momentum, and energy under the Boussinesq Approximation and discretized using finite differences. Our numerical domain is 10 m-wide with a grid resolution of 0.001 m. This is ~10-20 times the width of the primary shear deformation observed in the field. Boundary conditions include imposed equal, but opposing, velocities and fixed temperature (T = 800 ºC) at the edges of the domain. During each time step, convergence of the non-linear system is achieved through Picard iterations.

The rate of helium diffusion into the central part of the shear zone inversely correlates to average grain size. Individual grains are separated by the ITM, initially composed of dry grain boundaries. For our calculations of grain size and evolution rates, we assume that at the high temperatures of the mantle and deformation conditions, our shear zone is relatively dry, in that there is no excess water residing in grain boundaries (*Watson and Baxter*, 2007). In our model, we assume that before the initiation of deformation, grain boundaries are melt-free and thus small (e.g., <1 nm), but once deformation begins, it is possible that melt may be present, so we find 0.75 nm a reasonable estimate for grain boundary width; this width is equivalent to two monoatomic layers, typical of the grain-grain interface width in rocks (e.g., *Hiraga and Kohlstedt*, 2009; *Recanati et al*., 2012).

Initial and boundary conditions of the model are constrained by those of typical upper mantle rocks and values estimated for the Josephine Peridotite (Table 1). Prior to deformation, we assume constant values of viscosity, grain size, temperature, and ^{4}He concentration across the Z-axis of the shear zone. Initial ^{4}He concentrations and grain sizes are set equal to values measured in samples furthest from center of Josephine shear zones. To simulate the presence

of a fluid phase (e.g., melt) at the shear zone center, we impose a ^{4}He concentration of zero at the centermost gridpoint. This boundary condition effectively assumes rapid helium transfer from fluid to solid and that the melt acts as a sink due to the incompatibility of helium.

Table 1. Initial values and boundary conditions of the model based on conditions typical of mantle peridotite.

Symbol	Definition	Value/Units	Source
A_{disl}	Flow law pre-exponential constant	9×10^{3} Pa s^{-ndisl}	
A_{diff}	Flow law pre-exponential constant	7.8×10^{-1} Pa s	
B_{disl}	Strain rate pre-exponential constant	6.5×10^{-16} Pa^{-ndisl} s^{-1}	5,7,10
B_{diff}	Strain rate pre-exponential constant	7.7×10^{-8} m^{mdiff} Pa^{-ndiff} s^{-1}	5,7,10
b	Burgers vector	6×10^{-10} m	3
β	Interface segregation factor		
C_i	Initial total helium concentration	1×10^{-11} cc kg^{-1}	
c_p	Specific heat	1300 J kg^{-1} K^{-1}	5
d_0	Initial grain size	1000 µm	2
d	Rate of grain size evolution	m^2 s^{-1}	
D_0	Diffusion constant	1×10^{-7} m^2 s^{-1}	13
$D_{0\,LAT}$	Lattice diffusion constant	1.15×10^{-8} m^2 s^{-1}	13
$D_{0\,GB}$	Grain boundary diffusion constant	2.5×10^{-12} m^2 s^{-1}	13
D	Diffusion coefficient	m^2 s^{-1}	
D_{LAT}	Lattice diffusion coefficient	m^2 s^{-1}	
D_{GB}	Grain boundary diffusion coefficient	m^2 s^{-1}	
δ	Grain boundary width	0.75×10^{-9} m	9,11,12
E_{disl}	Dislocation creep activation energy	5.3×10^{5} J mol^{-1}	3,5,7,10
E_{diff}	Diffusion creep activation energy	3.75×10^{5} J mol^{-1}	7,10
E_{LAT}	Lattice diffusion activation energy	1.11×10^{5} J mol^{-1}	13
E_{GB}	Grain boundary diffusion activation energy	1.17×10^{3} J mol^{-1}	13
$\dot{\varepsilon}$	Strain rate	10^{-10} - 10^{-14} s^{-1}	2
$\dot{\varepsilon}_c$	Critical strain rate	0.05	1
$\dot{\varepsilon}_{II}$	Second invariant of strain rate	s^{-1}	
G_0	Grain growth coefficient	8×10^{-27} m^n s^{-1}	9
h	Shear heating term	W m^{-3}	
K	Partition coefficient		
k	Thermal conductivity	3.3×10^{-4} W m^{-1} K^{-1}	6
κ	Thermal diffusivity	7.92×10^{-11} m^2 s^{-1}	5
m_{disl}	Dislocation grain size exponent	0	2,4,5,7
m_{diff}	Diffusion grain size exponent	2 - 3	5,7
n_{disl}	Dislocation stress exponent	3.5	2,5,7
n_{diff}	Diffusion stress exponent	1	2,5,7
η	Mantle viscosity	10^{21} Pa s	
p	Stress exponent of grain size	3.2	2,9
ρ	Mantle density	3200 kg m^{-3}	
R	Universal gas constant	8.314 J mol^{-1} K^{-1}	
r	Grain size constant	1.18	8
σ	Shear stress	Pa	
T_0	Initial temperature	1073 K	
t	Time	s	
u	Velocity	m s^{-1}	
μ	Shear modulus	8.13×10^{10} Pa	3
V_{GB}	Grain boundary volume	m^3	
V_{LAT}	Lattice volume	m^3	
x	Distance	m	

1 *Braun et al., 1999* ***2*** *Cross et al., 2015* ***3*** *Riedel and Karato, 1997* ***4*** *Karato and Wu, 1993* ***5*** *Yamasaki et al., 2004* ***6*** *Yuen et al., 1978* ***7*** *Hirth and Kohlstedt, 2003* ***8*** *Turcotte and Schubert* ***9*** *Montési and Hirth., 2003* ***10*** *Precigout et al., 2007* ***11*** *Hiraga et al., 2004* ***12*** *Watson and Baxter, 2007* ***13*** *Burnard et al., 2015*

3.6.1 Viscosity

Deformation is assumed to occur by either dislocation or diffusion creep and, generally, depends on temperature, grain size, and strain rate:

$$\eta = A\left(\frac{d_0}{b}\right)^{\frac{m}{n}}(\dot{\varepsilon}_{II})^{\frac{1-n}{n}}\exp(\frac{-E}{nRT}) , \quad (2)$$

where A is a pre-exponential constant, d_0 is initial grain size, b is the Burgers vector, $\dot{\varepsilon}_{II}$ is the second invariant of the strain rate tensor, m and n is a mechanism specific exponents (i.e. dislocation or diffusion creep) governing grain size and strain rate dependence, E is activation energy, and R is the universal gas constant. At each point in the model, we harmonically average the effects of dislocation and diffusion creep to define an effective viscosity, η_{eff}:

$$\eta_{eff} = \left(\frac{1}{\eta_{disl}} + \frac{1}{\eta_{diff}}\right)^{-1} . \quad (3)$$

This formulation allows the weakest flow law to govern deformation within the shear zone.

3.6.2 Conservation equations

To simulate deformation in a ductile shear zone, we solve the equations of conservation of momentum, mass, and energy. These equations are, respectively,

$$\nabla \cdot \sigma + \rho\vec{g} = 0 , \quad (4)$$

$$\nabla \cdot \vec{u} = 0 , \quad (5)$$

and

$$\nabla \cdot (k\nabla T) + \rho h = \rho c_p(\frac{\partial T}{\partial t} + u \cdot \nabla T) , \quad (6)$$

where σ is the stress tensor, g is acceleration due to gravity, u is shearing velocity, k is thermal conductivity, T is temperature, ρ is mantle density, h is shear heating, c_p is heat capacity, and t is time. In the conservation of momentum, we take the second term to be zero by assuming that there are no lateral density differences across the horizontally oriented shear zone. In addition, we assume that velocities only vary along the shear zone, allowing us to eliminate all terms that depend upon other conditions, yielding

$$\nabla \cdot \sigma = 0 \quad (7)$$

and, in one dimension,

$$\frac{\partial \sigma_{xx}}{\partial x} = 0 , \quad (8)$$

which we solve as

$$\frac{\partial}{\partial x}\left(\eta \frac{\partial u}{\partial x}\right) = 0\,. \quad (9)$$

In the conservation of volume equation, velocity is solved along the y-axis, parallel to shear motion. In our model, however, velocity varies only along the x-axis, and thus (5) is automatically satisfied. In the conservation of energy equation, the second term in parentheses on the right is that of advection, which is zero in our model, as motion does not occur parallel to our numerical domain, so (6) becomes:

$$\frac{\partial}{\partial x}\left(k \frac{\partial T}{\partial x}\right) + \rho h = \rho c_p \left(\frac{\partial T}{\partial t}\right). \quad (10)$$

The shear heating term *h* is estimated using

$$h = \tau_{xy} \frac{\partial u}{\partial x}\,. \quad (11)$$

The contribution of shear heating is re-calculated within each Picard iteration to ensure that this term is consistent with the calculated viscosity.

3.6.3 Stress and strain rate

Evolving viscosity in our model affects stress and strain rate (and later recrystallized grain size) according to the relationship

$$\sigma = \eta \dot{\varepsilon}, \quad (12)$$

using effective viscosity from Eq. 10 and total strain rate from Eq. 16. This stress is then used to calculate strain rate for each deformation regime, following the general flow law equation:

$$\dot{\varepsilon} = A\sigma^n \, exp(\frac{-E}{RT}) \quad (13)$$

(*Hirth and Kohlstedt*, 2003; *Warren and Hirth*, 2006; *Hansen et al*., 2011).

3.6.4 Helium diffusion

To evaluate the changing concentration of He across the shear zone due to diffusion into an assumed melt transport zone at the shear zone center (dunite samples in SZ A and B), we use Fick's second law of non-steady diffusion

$$\frac{\partial C}{\partial t} = D \frac{\partial^2 C}{\partial x^2}\,, \quad (14)$$

(*Trull and Kurz*, 1993; *Watson and Baxter*, 2007) where *C* is helium concentration and *D* is the diffusion coefficient of helium

$$D = D_0 exp(\frac{-E_{He}}{RT}) , \quad (15)$$

where D_0 is an empirically determined pre-exponential constant, *E* is the activation energy of helium within olivine, *R* is the universal gas constant, and *T* is temperature (*Fisher*, 1951; *Dodson*, 1973; *Hiraga et al*., 2004; *Wang et al*., 2015). Although we use Fick's second law to model single-phase diffusion of helium through mantle peridotite, diffusion in natural mantle rocks is more complicated. Materials are generally heterogeneous, with varying grain size, noble gas concentration, and mineral concentrations and modes. To account for some of these complications, while maintaining the simplicity of single-phase diffusion, we calculate a bulk diffusion that combines diffusion through both grain lattices and boundaries in polyphase systems (*Poirier*, 2005; *Watson and Baxter*, 2007; *Burnard et al*., 2015). We also assume that the entire shear zone has an initial homogeneous concentration of helium prior to deformation (which we determine individually for SZs A and B based on the helium concentration of the sample furthest from each shear zone center). After deformation begins, focused melt infiltration at the shear zone center is assumed to act as a sink for He in the host rock with a boundary condition of $C(t)$=0 at x=0. In a natural system such as the Josephine Peridotite, gases must diffuse through a heterogeneous material, often consisting of multiple mineral phases with different diffusivities, varying grain sizes (and thus diffusive length scales), presence of fluids, and concentration gradients. The effective bulk diffusivity is then:

$$D^{bulk} \approx D^{LAT} + \beta(3\delta/d)D^{GB} \quad (16)$$

where δ is average grain boundary width, d is current grain size, and β, the interface segregation factor, is

$$\beta_i = \frac{C_i^{GB}}{C_i^{LAT}} \quad (17)$$

(*Watson and Baxter*, 2007; *Hart et al*., 2008; *Dohmen and Milke*, 2010; *Burnard et al*., 2015). It is expected that during mantle melting, β is approximately equal to 1, and the gases partitioned between lattice and boundary are in equilibrium (*Jackson et al*., 2013); we make a similar assumption to simplify our calculations. Grain boundary width δ is held constant throughout the simulations at 0.75 nm (*Hiraga and Kohlstedt*, 2009; *Recanati et al*., 2012). The interface segregation factor is the inverse of the partition coefficient *K*:

$$K = \frac{C_i^{LAT}}{C_i^{GB}} \quad (18)$$

(*Burnard et al*., 2015). In the literature, values of *K* are reported on the order of 10^{-3} to 10^{-5} in olivine (*Trull and Kurz*, 1993; *Parman et al*., 2005; *Jackson et al*., 2013). Experimental *K* values range from 3.8×10^{-5} to 1.4×10^{-3} (Table D.2) (*Parman et al*., 2005; *Heber et al*., 2007; *Jackson et al*., 2013). Because the partition coefficient describes the incompatible behavior of noble gases, such low K_{He} values indicate that helium will preferentially partition to grain boundaries during mantle melting or deformation conditions (*Heber et al*., 2007). However, in addition to the value of *K*, partitioning of helium between the matrix and grain boundaries depends on the volume ratio V_{GB}/V_{LAT}, which describes the volume of grain boundaries and lattices occupied by gas (*Hiraga et al*., 2004; *Jackson et al.*, 2013; *Burnard et al.*, 2015). *Hiraga et al*. (2004) and *Burnard et al*. (2015) give empirical relations for these volumes as

$$V_{GB} = 1.73\delta d^2 \quad (19)$$

$$V_{LAT} = 0.52d^3 \quad (20)$$

for tetrakaidecahedral grains.

Hart et al. (2008) use a similar method as Eq. 14 in their study of diffusive length scales of helium. However, they also include a helium production term on the right-hand side of the equation, *P(t)*. This variable considers the production of ^{4}He from the radioactive decay of U and Th. Considering the half-life of U^{238} is 4.4×10^9 years, we ignore this term for the relatively short timescale of this study (a maximum of ~35 My considering the deformation history of the Josephine Ophiolite).

It is worth noting that helium diffusion in olivine is slightly anisotropic, favoring the [100] and [001] directions (*Cherniak and Watson*, 2012; *Wang et al.*, 2015). However, we consider bulk diffusion to be isotropic on the outcrop scale considered in our study.

3.6.5 Grain size

The general law for grain size evolution ($\dot{d}$) is

$$\dot{d} = \dot{d}_{grow} - \dot{d}_{reduc}, \quad (21)$$

where

$$\dot{d}_{grow} = G_0 p^{-1} d^{1-p} - \dot{\varepsilon} d/\dot{\varepsilon}_c \quad (22)$$

$$\dot{d}_{reduc} = G_0 p^{-1} d^{1-p} - B_{disl} \sigma^{n_{disl}} d/\dot{\varepsilon}_c, \quad (23)$$

G_0 is the grain growth coefficient, p is the grain growth exponent, d is the current grain size, $\dot{\varepsilon}$ is the strain rate accommodated by the dominant creep mechanism, $\dot{\varepsilon}_c$ is the critical strain rate for microstructure evolution, B_{disl} is a dislocation mechanism-specific constant, and $\sigma^{n_{disl}}$ is the current stress raised to the dislocation stress exponent (*Braun et al*., 1999; *Hall and Parmentier*, 2003; *Montési and Hirth*, 2003; *Austin and Evans*, 2007; *Cross et al*., 2015). Of the three grain size evolution laws discussed in Section 2.6, we consider the CRX theory to be the most applicable for our study because it does not treat grain growth and reduction exclusively, as FB and mFB do (*Hall and Parmentier*, 2003; *Montési and Hirth*, 2003; *Austin and Evans*, 2007). Using the CRX-specific equation, our combined grain size evolution equation is

$$\dot{d} = (G_0 p^{-1} d^{1-p} - \dot{\varepsilon}_{disl} d/\dot{\varepsilon}_c) + (G_0 p^{-1} d^{1-p} - B_{disl} \sigma^{n_{disl}} d/\dot{\varepsilon}_c) \quad (24)$$

which utilizes both grain growth through diffusion creep and grain size reduction through dislocation creep. This model incorporates evolving temperature, grain size, and $\dot{\varepsilon}_{disl}$ (calculated using Eq. 13) at every iteration. Once this rate of grain size evolution has been calculated across the domain, the change in grain size for that time step is added to the current grain size to yield a new grain size.

3.6.6 Non-dimensionalization

Once discretized, each of the above equations is non-dimensionalized using initial values of temperature, length, mass, time, and composition:

$$\bar{L} = x_0 \qquad \bar{T} = \frac{x_0}{u_0} \qquad \bar{M} = \frac{\eta_0 x_0^2}{u_0} \qquad \bar{K} = T_0 \qquad \bar{C} = C_i,$$

where x_0 is the domain size, u_0 is initial velocity, η_0 is initial viscosity, T_0 is temperature at the boundaries, and C_i is the initial He concentration. These values yield units of m, s, kg, T, and cc kg^{-1}, respectively. Using these scaling terms, non-dimensionalized viscosity becomes

$$\bar{\eta} = \left(A \frac{\bar{L}\bar{T}}{\bar{M}} \bar{T}^n\right) \left(\frac{d_0 \bar{L}^{-1}}{b\bar{L}^{-1}}\right)^{\frac{m}{n}} \left(\frac{du}{dx} \bar{T}\right)^{\frac{1-n}{n}} \exp\left(\frac{-E_a}{nR\bar{T}\bar{K}}\right). \quad (25)$$

This equation can be solved for both viscosity due to dislocation and diffusion creep to solve for non-dimensionalized effective viscosity:

$$\bar{\eta}_{eff} = \left(\frac{1}{\bar{\eta}_{disl}} + \frac{1}{\bar{\eta}_{diff}}\right)^{-1} \quad (26)$$

Which can then be used to solve conservation of momentum:

$$\frac{\partial}{\partial x}\left(\bar{\eta}_{eff}\frac{\partial u}{\partial x}\bar{T}\right)=0\ . \quad (27)$$

The shear heating term and conservation of energy equations are

$$\bar{h}=\bar{\eta}_{eff}\left(\frac{\partial u}{\partial x}\bar{T}\right)^2 \quad (28)$$

and

$$\left(\frac{\partial k}{\partial x}\frac{\bar{T}^3\bar{K}}{\bar{M}}\right)\left(\frac{\partial^2 T}{\partial x^2}\frac{\bar{L}^2}{\bar{K}^2}\right)+\rho\frac{\bar{L}^3}{\bar{M}}\bar{h}=\rho\frac{\bar{L}^3}{\bar{M}}c_p\frac{\bar{T}^2\bar{K}}{\bar{L}^2}\left(\frac{\partial T}{\partial t}\frac{\bar{T}}{\bar{K}}\right). \quad (29)$$

Total strain rate becomes

$$\dot{\varepsilon}=\left(A\frac{\bar{L}\bar{T}}{\bar{M}}\bar{T}^n\right)\left(\sigma^n\frac{\bar{M}}{\bar{L}\bar{T}}^n\right)\exp(\frac{-E}{RT\bar{K}}) \quad (30)$$

and the diffusion equations are

$$\bar{D}=\left(D_0\frac{\bar{T}}{\bar{L}^2}\right)\exp(\frac{-E_{He}}{RT\bar{K}}) \quad (31)$$

$$\frac{\partial C}{\partial t}\frac{\bar{T}}{\bar{C}}=\bar{D}\frac{\partial^2 C}{\partial x^2}\frac{\bar{L}^2}{\bar{C}^2}\ . \quad (32)$$

Finally, the non-dimensionalized grain size evolution rate equation becomes

$$\dot{\bar{d}}=(G_0\frac{\bar{T}}{\bar{L}^{n_{diff}}}p^{-1}\frac{d^{1-p}}{\bar{L}^{1-p}}-\frac{\dot{\varepsilon}d}{\dot{\varepsilon}_c}\frac{\bar{T}}{\bar{L}})+(G_0\frac{\bar{T}}{\bar{L}^{n_{disl}}}p^{-1}\frac{d^{1-p}}{\bar{L}^{1-p}}-\frac{B_{disl}\sigma^{n_{disl}}d}{\dot{\varepsilon}_c}\left(\frac{\bar{M}}{\bar{L}\bar{T}^2}^{n_{disl}}\bar{T}\right)\frac{\bar{M}}{\bar{L}\bar{T}}\bar{L}^{-1}). \quad (33)$$

4. Results

4.1 Helium results

4.1.1 Shear zone A

Helium concentration from crushing and melting experiments of SZ A and B are summarized in Tables 2 and 3 and complete results are listed in Appendix D. In SZ A samples, 5-12% of total ^{4}He is released by crushing, similar to values measured by *Recanati et al*. (2012). Total ^{4}He concentrations in these samples have a median value of 51.8 ncc STP g^{-1} and a range of 26.0 to 106.1 ncc STP g^{-1}. Sample 04A, located 0.03 m to the right of the structural SZ center (sample M08; 124.9 ncc g^{-1}), has the highest ^{4}He concentration of samples measured in this study (106.1 ncc STP g^{-1}). Combining our data with that of *Recanati et al*. (2012), we find a complex pattern of total ^{4}He concentrations near the SZ center (Fig. 10, 11). Approaching the shear zone center, total ^{4}He concentrations decrease from equilibrium values over a small domain and then increase sharply at the center.

$^{3}He/^{4}He$ values vary at the center of SZ A, with a median value of 6.48 ± 0.12 Ra (Fig. 12). In all samples, $^{3}He/^{4}He$ values obtained by melting are higher than those from crushing (7.89 ± 0.10 Ra and 6.48 ± 0.12 Ra, respectively), consistent with the findings of *Recanati et al*. (2012).

Table 2. Helium results of SZ A from whole rock analyses (nd = not determined).

	Crush			Melt			Total			
Sample	^{4}He ncc/g	^{3}He/^{4}He Ra	± R/Ra	^{4}He ncc/g	^{3}He/^{4}He Ra	± R/Ra	^{4}He ncc/g	Fraction released by crush	Mean grain size (µm)	Distance from center (m)
JP10M06	5.4	6.76	0.14	48.5	8.04	0.11	54.1	0.10	482	-0.78
JP10M07	7.4	6.65	0.12	49.2	8.60	0.12	56.9	0.13	nd	-0.64
JP10M08	5.5	6.56	0.12	115.3	7.16	0.09	121.1	0.05	289	0
JP10M08	4.6	6.47	0.14	104.6	6.84	0.10	109.7	0.07	289	0
JP10M08	6.1	6.52	0.12	118.3	7.26	0.09	124.9	0.08	289	0
JP10M09	5.2	6.63	0.13	49.1	8.29	0.11	54.7	0.10	642	0.85
JP10M12	6.0	6.41	0.12	60.7	8.16	0.11	67.1	0.09	780	2.62
JP10M13	7.5	6.60	0.12	48.5	8.14	0.11	56.8	0.13	1022	3.61
JP10M14	3.9	6.39	0.13	22.6	10.95	0.17	26.8	0.15	797	4.74
JP10M15	4.8	6.84	0.12	47.4	8.90	0.12	52.5	0.09	838	7.07
JP15-KnE-01A	3.8	6.48	0.12	64.4	7.40	0.10	68.2	0.06	268	-0.11
JP15-KnE-02A	1.8	6.38	0.15	24.2	9.50	0.12	26.0	0.07	237.51	-0.06
JP15-KnE-03A	1.4	6.48	0.17	29.8	9.00	0.11	31.2	0.05	nd	-0.01
JP15-KnE-04A	13.2	6.74	0.10	92.9	7.63	0.10	106.1	0.12	234.89	0.03
JP15-KnE-05A	3.5	6.28	0.13	48.3	6.51	0.10	51.8	0.07	nd	0.06
JP15-KnE-06A	2.8	6.39	0.12	35.5	9.01	0.11	38.3	0.07	236.58	0.08
JP15-KnE-07A	6.2	6.56	0.11	68.4	7.89	0.10	74.6	0.08	401	0.10

Table 3. Helium results of SZ B from whole rock analyses.

	Crush			Melt			Total		
Sample	^{4}He ncc/g	^{3}He/^{4}He Ra	± R/Ra	^{4}He ncc/g	^{3}He/^{4}He Ra	± R/Ra	^{4}He ncc/g	Fraction released by crush	Distance from center (m)
JP13-D35	6.1	6.81	0.11	36.0	9.62	0.12	42.1	0.15	-5.20
JP13-D36	1.9	6.60	0.15	15.4	14.19	0.18	17.3	0.11	-3.11
JP13-D37	5.9	6.59	0.11	40.0	9.04	0.11	45.9	0.13	-2.60
JP13-D38	3.5	6.28	0.12	73.3	5.32	0.07	76.8	0.05	-1.20
JP13-D39	3.9	6.45	0.12	34.5	8.08	0.10	38.4	0.10	-0.29
JP13-D34	1.5	5.42	0.16	11.8	13.71	0.18	13.3	0.11	0.92
JP13-D40	2.0	6.57	0.15	16.4	11.67	0.15	18.4	0.11	0.45
JP13-D41	2.2	6.12	0.13	24.9	9.82	0.12	27.1	0.08	0.25
JP13-D42	2.5	5.84	0.13	44.0	7.89	0.01	46.5	0.05	0.50
JP13-D43	1.9	6.13	0.14	18.9	10.97	0.14	20.8	0.09	0.70
JP13-D44	2.6	5.97	0.12	22.3	9.66	0.12	24.9	0.10	1.20
JP13-D45	3.3	6.11	0.11	25.4	10.97	0.14	28.7	0.11	2.31

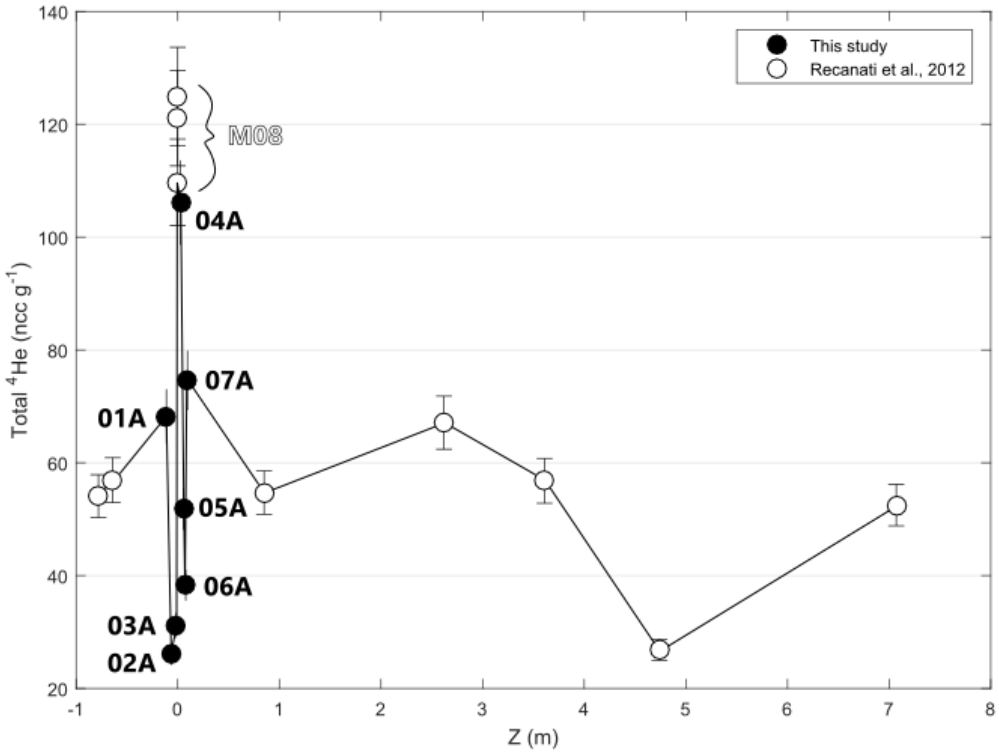

Figure 10. Samples from SZ A demonstrate a peak in total ^{4}He concentrations (ncc STP g^{-1}) at the structural center of the shear zone. Z is the distance from sample JP10M08 (assumed to be at the SZ center). Values from SZ A include new (black circles) and previously reported samples (white circles; *Recanati et al*., 2012). The structural shear zone center correlates with the highest helium values.

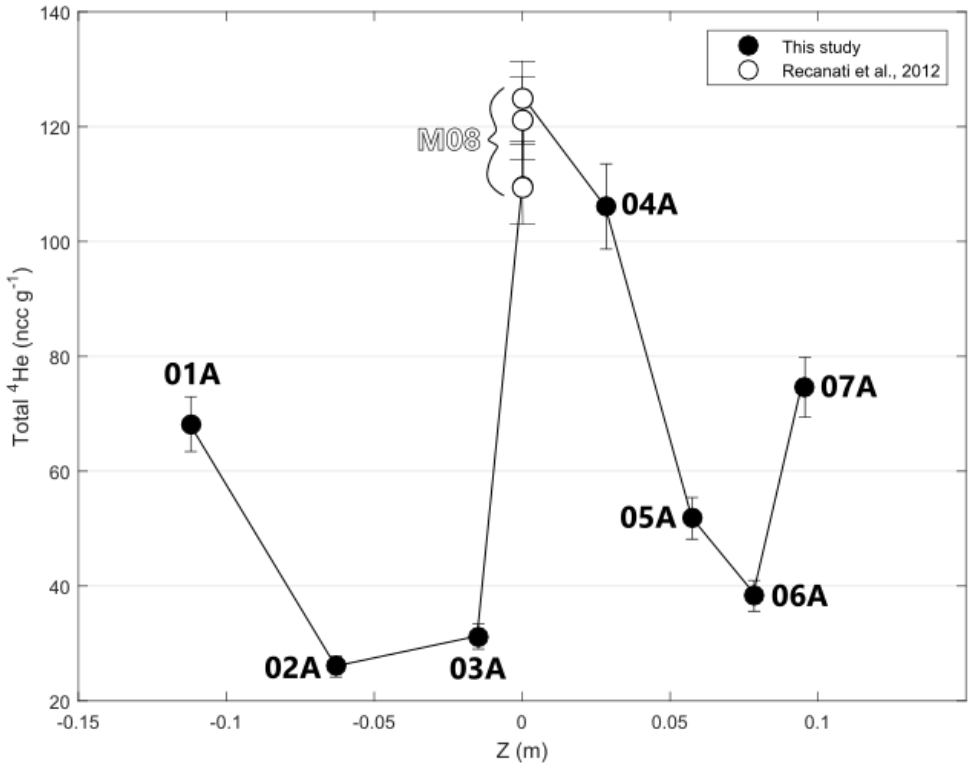

Figure 11. ^{4}He concentrations peak (124.9 ncc g^{-1}) at the center of SZ A, but display relative lows in the bordering samples. This change in concentration occurs over a distance of ~0.07 m.

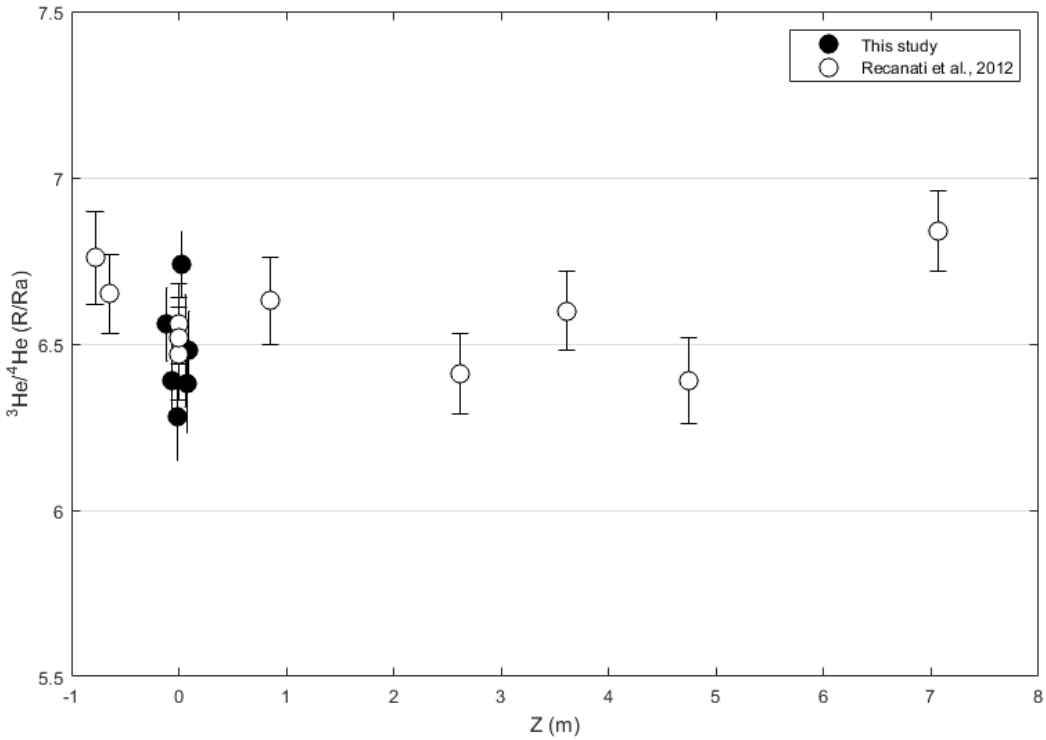

Figure 12. Helium isotope ratios across SZ A are consistent, demonstrating little variability or dependence on distance from the shear zone center.

4.1.2 Shear zone B

The fraction of total helium released by crushing in SZ B is 5-15%. Total ^{4}He at the presumed center (0 m, Fig. 13) is 27.9 ncc STP g^{-1}, approximately half the value seen in SZ A. The highest total ^{4}He value is located approximately one meter to the left of the structural shear zone center (D38; 76.8 ncc g^{-1}). On the opposite side of the SZ center (~0.6 m), we find a sharp increase in ^{4}He concentration in sample D42, bordered by low ^{4}He concentrations; this peak in helium concentrations corresponds to the location of the maximum calculated shear strain (Fig. 25).

Values of ^{3}He/^{4}He are slightly lower than in SZ A, with a median of 6.20 ± 0.13 Ra (Fig. 14). Melting of these samples yields higher ^{3}He/^{4}He values than in SZ A, with a median of 9.74 ± 0.12 Ra, indicating SZ B is more enriched in ^{3}He relative to ^{4}He than SZ A.

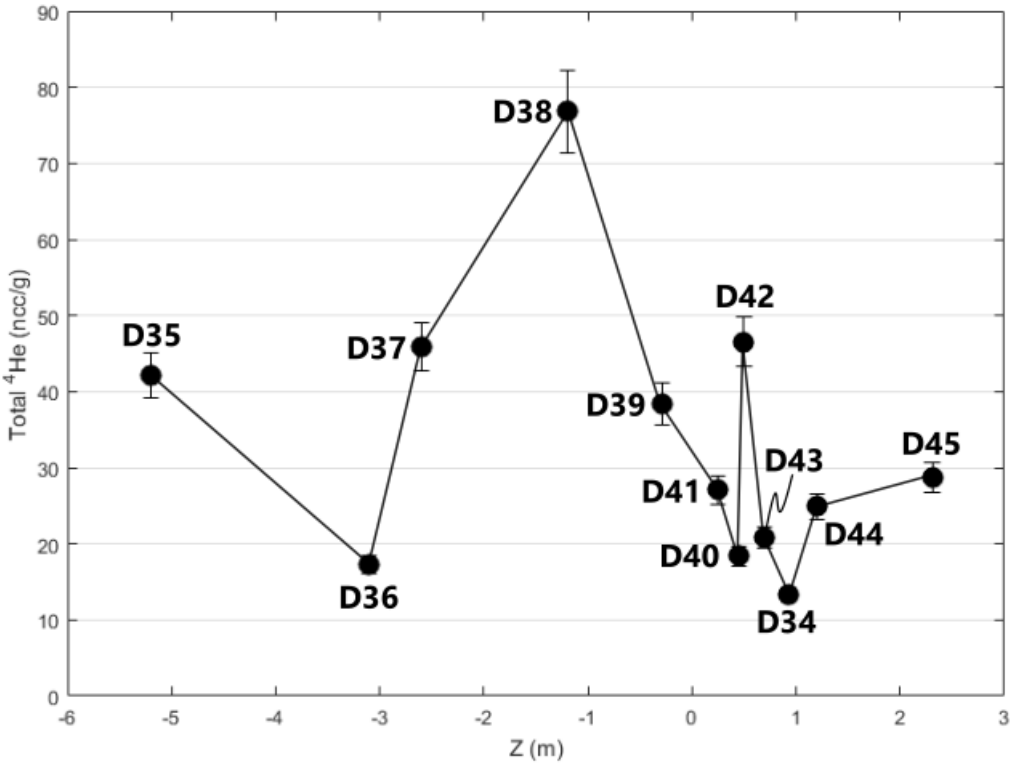

Figure 13. Variability in ^{4}He concentration in SZ B. What is presumed to be the shear zone center based on structural observations in the field does not correlate with the helium data; here, the highest peak in He concentration occurs at ~-1 m. As in SZ A, significant decreases in ^{4}He are observed immediately bordering the highest peak in concentration.

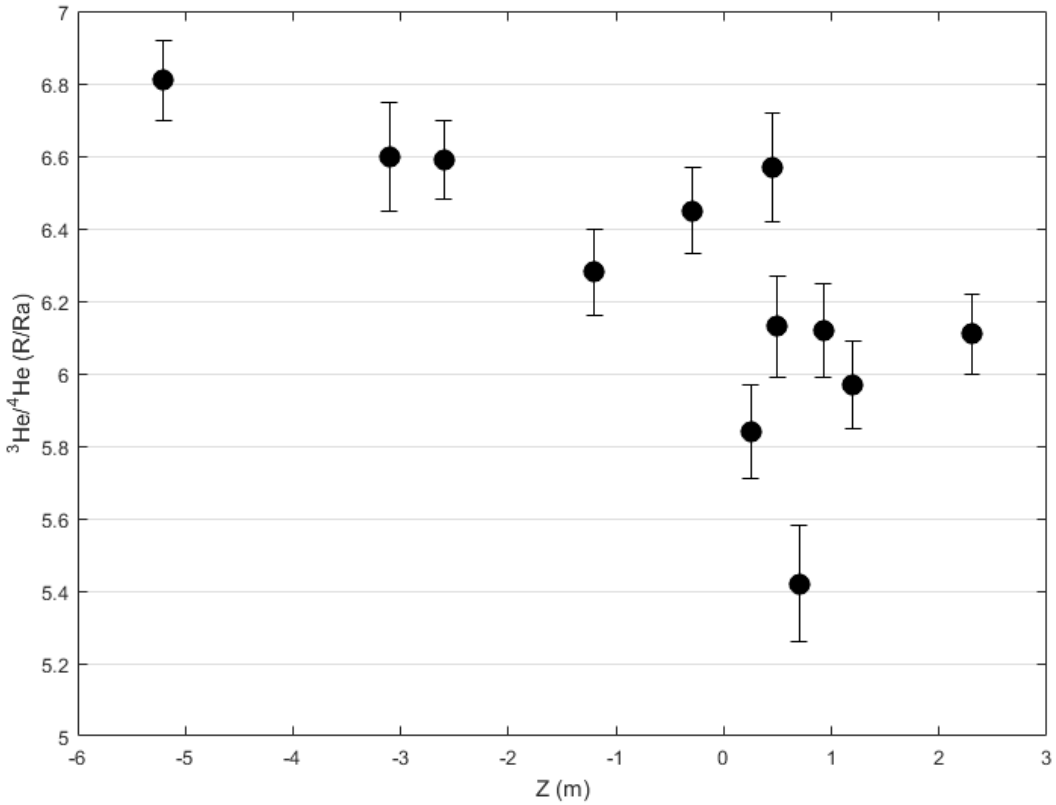

Figure 14. Helium isotope ratios across SZ B. $^{3}He/^{4}He$ ratios were obtained by crushing whole rock samples. The data exhibit a decreasing trend towards Z = 1 m, roughly correlating with the highest strain in SZ B (Fig. 25).

Table 4. Location and orientation results for shear zone A samples of this study (na = not applicable; nd = not determined).

	Sample	Mean grain size (μm)	X (m)	Z (m)	Shear plane	Rot & proj shear plane	Field strike/dip	Field trend/plunge	Rot & proj strike/dip	Rot & proj trend/plunge	Shear strain (%)	α	α'	Source
Shear zone A	JP10M06	482	0.90	-0.78	45/90	270/90	217/90	nd	265/90	nd	1103	87	5	1
	JP10M07	nd	0.37	-0.64			220/90	nd	267/90	nd	1774		3	
	JP10M08	289	0.00	0.00			226/88	nd	269/90	nd	6433		1	
	JP10M09	642	0.43	0.85			217/88	nd	263/90	nd	848		7	
	JP10M10	nd	0.85	1.70			226/63	nd	249/90	nd	259		21	
	JP10M11	nd	0.24	2.19			218/40	nd	225/90	nd	96		45	
	JP10M12	780	0.07	2.62			202/25	nd	206/90	nd	44		64	
	JP10M13	1022	1.26	3.61			30/2	nd	183/90	nd	0		87	
	JP10M14	797	-1.66	4.74			35/12	nd	196/90	nd	24		74	
	JP10M15	838	-3.16	7.07			75/20	nd	200/90	nd	31		70	
	JP15-KnE-01A	268	0.07	-0.10			nd	221/7	nd	09/90	nd		nd	2
	JP15-KnE-02A	237	0.08	-0.08			nd	213/9	nd	53/90	nd		nd	
	JP15-KnE-03A	nd	0.07	-0.06			nd	218/18	nd	22/90	nd		nd	
	JP15-KnE-04A	234	0.13	-0.03			nd	225/16	nd	21/90	nd		nd	
	JP15-KnE-05A	nd	0.16	0.01			nd	219/24	nd	29/90	nd		nd	
	JP15-KnE-06A	236	0.15	0.06			nd	224/19	nd	24/90	nd		nd	
	JP15-KnE-07A	401	0.14	0.11			nd	220/30	nd	35/90	nd		nd	
1 Recanati et al., 2012; 2 This study														

Table 5. Location and orientation results for shear zone B samples of this study (na = not applicable; nd = not determined).

	Sample	Mean grain size (μm)	X (m)	Z (m)	Shear plane	Rot & proj shear plane	Field strike/dip	Field trend/plunge	Rot & proj strike/dip	Rot & proj trend/plunge	Shear strain (%)	α	α'	Source
Shear zone B	JP13-D35	nd	3.99	-5.20	52/90	261/90	nd	28/63	nd	254/90	nd	25.4	nd	2
	JP13-D36	nd	1.26	-3.11			nd	217/68	nd	252/90	nd		nd	
	JP13-D37	nd	0.26	-2.60			nd	208/71	nd	249/90	nd		nd	
	JP13-D38	nd	-0.18	-1.20			nd	218/78	nd	261/90	nd		nd	
	JP13-D39	nd	-0.05	-0.29			nd	223/84	nd	269/90	nd		nd	
	JP13-D34	nd	1.00	0.92			nd	50/85	nd	258/90	nd		nd	
	JP13-D40	nd	1.39	0.45			nd	223/70	nd	257/90	nd		nd	
	JP13-D41	nd	0.17	0.25			nd	217/68	nd	252/90	nd		nd	
	JP13-D42	nd	0.13	0.50			nd	202/48	nd	228/90	nd		nd	
	JP13-D43	nd	-0.11	0.70			nd	26/24	nd	211/90	nd		nd	
	JP13-D44	nd	0.06	1.20			nd	275/06	nd	185/90	nd		nd	
	JP13-D45	nd	0.35	2.31			nd	45/09	nd	191/90	nd		nd	
	JP15-D01f	na	-0.03	-1.56			211/73	nd	253/90	nd	328		17	
	JP15-D02f	na	-0.03	-1.28			209/78	nd	255/90	nd	569		15	
	JP15-D03f	na	-0.02	-0.74			206/77	nd	252/90	nd	317		18	
	JP15-D04f	na	0.00	0.00			222/89	nd	272/90	nd	166		-2	
	JP15-D05f	na	0.00	0.14			212/89	nd	265/90	nd	925		5	
	JP15-D06f	na	0.01	0.31			210/88	nd	263/90	nd	2017		7	
	JP15-D07f	na	0.01	0.52			209/87	nd	262/90	nd	5366		8	
	JP15-D08f	na	0.02	0.72			208/86	nd	260/90	nd	13555		10	
	JP15-D09f	na	0.02	0.94			206/84	nd	258/90	nd	1415		13	
	JP15-D10f	na	0.03	1.18			197/81	nd	249/90	nd	138		21	
	JP15-D11f	na	0.03	1.31			196/76	nd	245/90	nd	0		25	
1 Recanati et al., 2012; 2 This study														

4.2 Thin section characterization

4.2.1 Shear zone A

The angular difference between strike of the foliation and shear planes, α, varies from 87º outside the shear zone to 1º at the structural shear zone center. We calculate total shear strains of 0 to 6433%, respectively. Sample M08 is the most deformed, and samples M12 to M15 are relatively undeformed (strain < 50%) (Fig. 15).

Analysis of the BSE maps yields mean grain sizes and mineral modal compositions, summarized in Table 8 and Appendix A. Grain sizes in SZ A range from 234 to 401 μm, with a minimum grain size of 234 μm in the centermost sample, 04A (Table 6). Modal compositions demonstrate that all samples are composed of primarily (≥ 70%) olivine, and are pyroxene-poor (< 3%) (Fig. 16, 17). Note that we do not differentiate between orthopyroxene and clinopyroxene in these samples. Samples from this study are more serpentinized than previous samples from SZ A; our samples contain 21-29% serpentine (Fig. 16, 19), compared to 1-4% seen by *Recanati et al*. (2012). Minor mineral phases include oxides (< 3%) and spinel (< 1%).

To assess potential storage capacity of helium within grains, we calculate the ratio of grain boundary to grain lattice volumes (V_{GB}/V_{LAT}) for each sample using mean grain sizes. Using Eq. 19 and 20 and an assumed grain boundary width of 0.75 nm (*Hiraga and Kohlstedt*, 2009; *Recanati et al*., 2012), V_{GB}/V_{LAT} ratios range from 6×10^{-6} to 11×10^{-6}, with the largest ratio occurring at the centermost samples (Fig. 21). There is a correlation between V_{GB}/V_{LAT} and decreasing grain size (Fig. 22) and V_{GB}/V_{LAT} and increasing total ^{4}He concentration (Fig. 23).

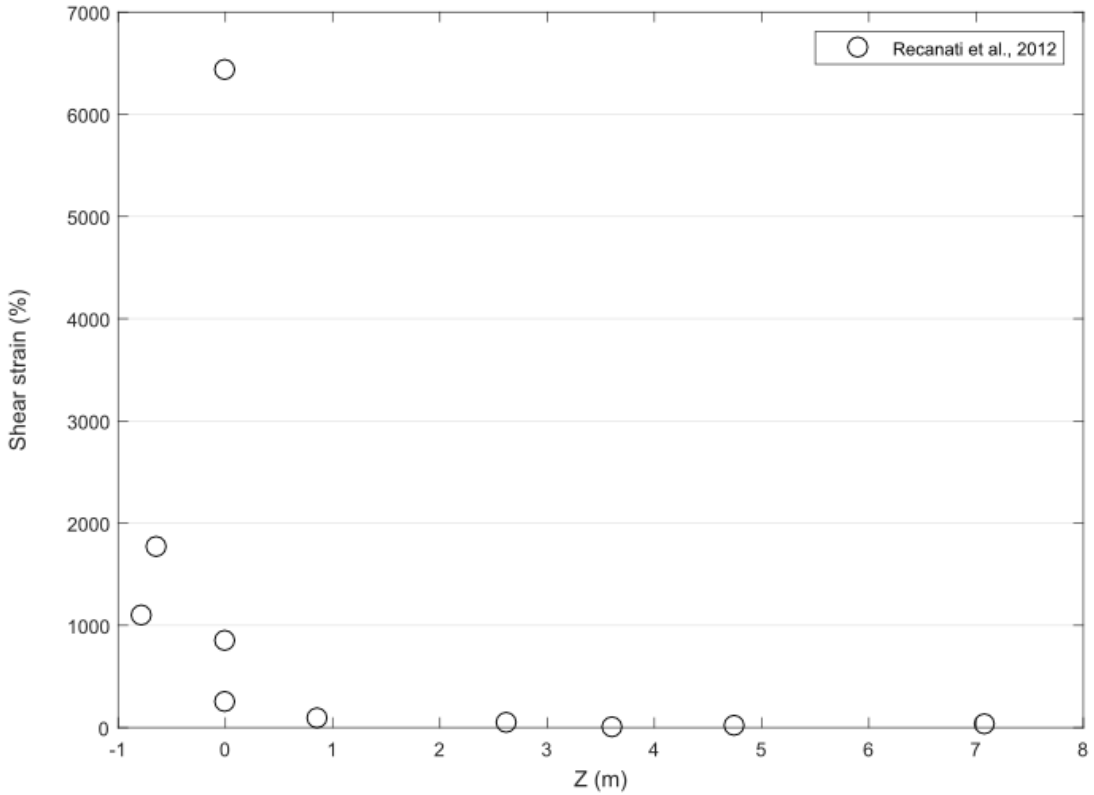

Figure 15. Total shear strain across SZ A indicates that the shear zone center is located at the approximate location of the observed structural center.

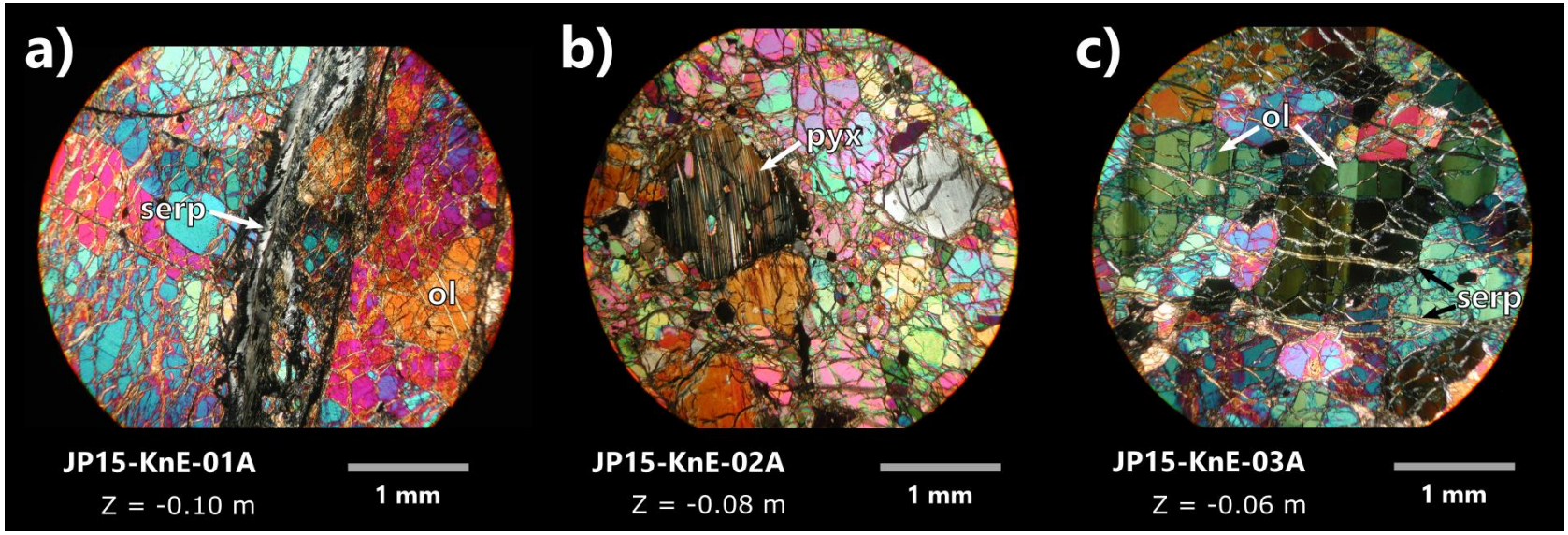

Figure 16. SZ A thin sections under cross-polarized light, 5x magnification, demonstrating mineral phases present in the Josephine Peridotite. A) Sample JP15-KnE-01A. Olivine (ol) is the dominant mineral phase, with individual fractured grains displaying unique birefringence, and is altered by cross-cutting veins of serpentine (serp). B) Sample JP15-KnE-02A. An altered pyroxene (pyx) amongst olivine. C) Sample JP15-KnE-03A. Olivine subgrains are indicated by regions of different birefringence within a single crystal. Small serpentine veins cut through olivine grains.

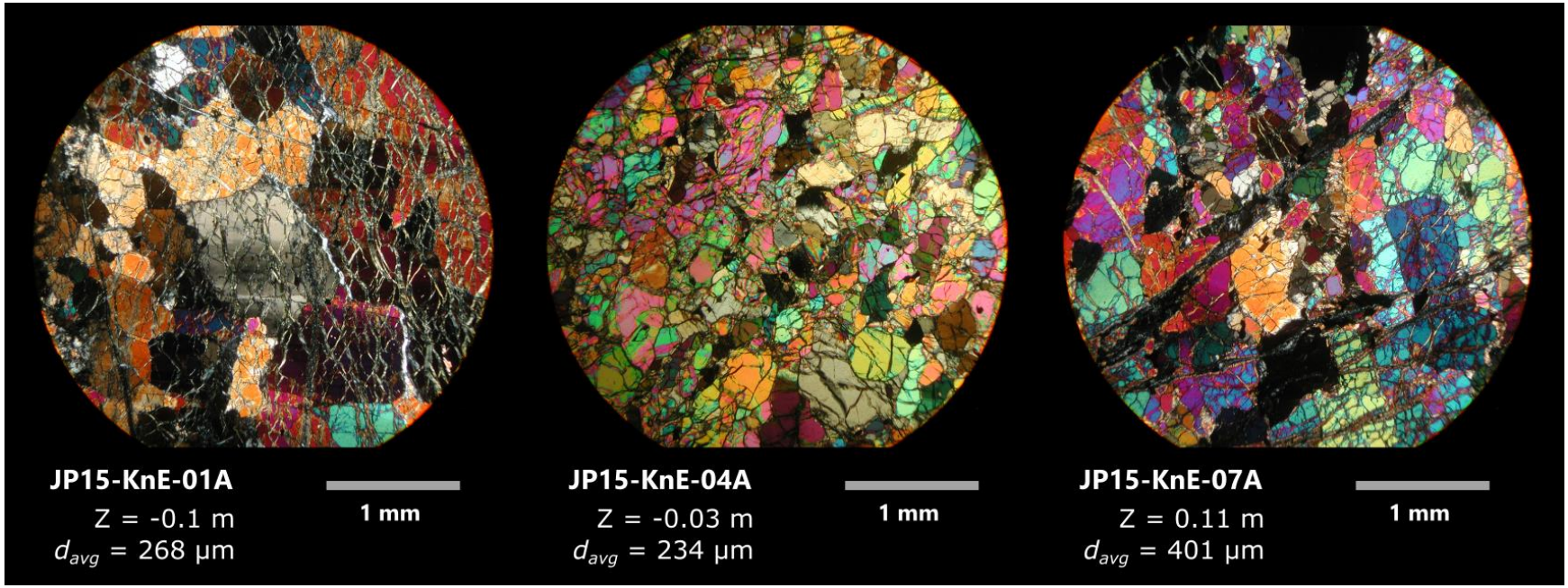

Figure 17. Relative grain size in SZ A demonstrated in edge (01A, 07A) and center (04A) samples (cross-polarized light, 5x magnification).

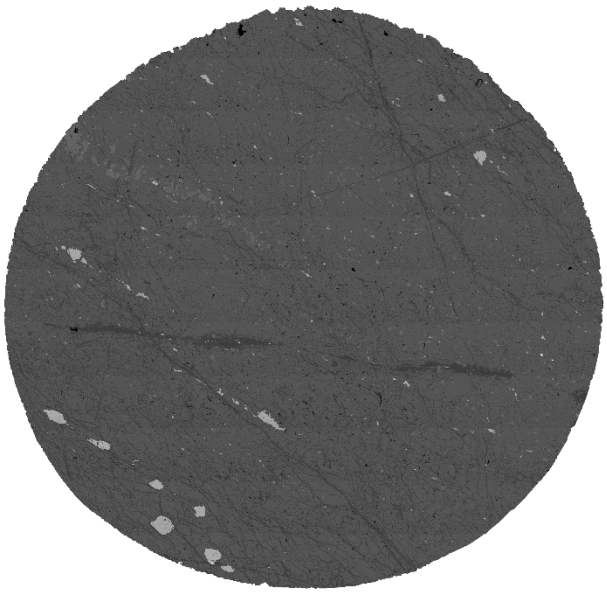

Figure 18. Back-scatter electron map of sample JP15-KnE-04A. The majority of the sample is composed of olivine with dark stripes of serpentine and large, light gray grains of pyroxene.

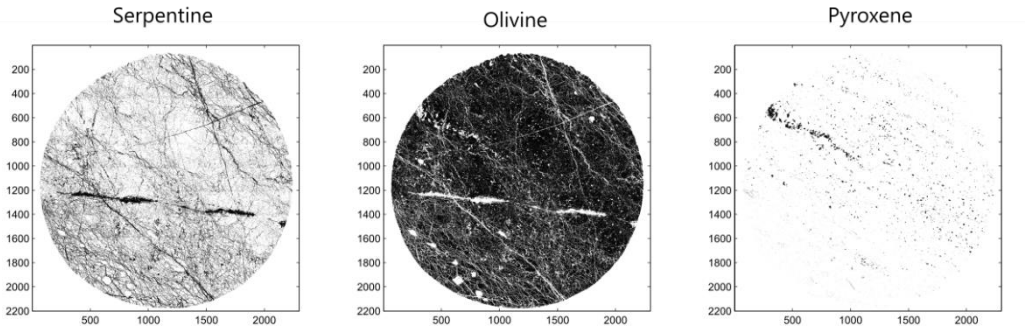

Figure 19. Modal compositions of sample JP15-KnE-04A. Total composition of each mineral was estimated by thresholding particular grayscale values corresponding to each mineral. The percentage of present minerals in each sample is summarized in Table 6.

Table 6. Mineral modal compositions for each sample in SZ A as determined using BSE images. All values are given in percentages.

	Percent mineral modal composition					
	Olivine	Serpentine	Pyroxene	Spinel	Oxides	Grain size (µm)
JP15-KnE-01A	70.7	28.0	0.9	0.1	0.3	268
JP15-KnE-02A	68.5	28.7	1.5	0.3	0.9	237
JP15-KnE-03A	nd	nd	nd	nd	nd	nd
JP15-KnE-04A	74.8	21.6	1.7	0.9	0.9	234
JP15-KnE-05A	nd	nd	nd	nd	nd	nd
JP15-KnE-06A	66.2	27.2	2.6	1	2.9	236
JP15-KnE-07A	74.8	23.1	1.6	<0.01	0.4	401

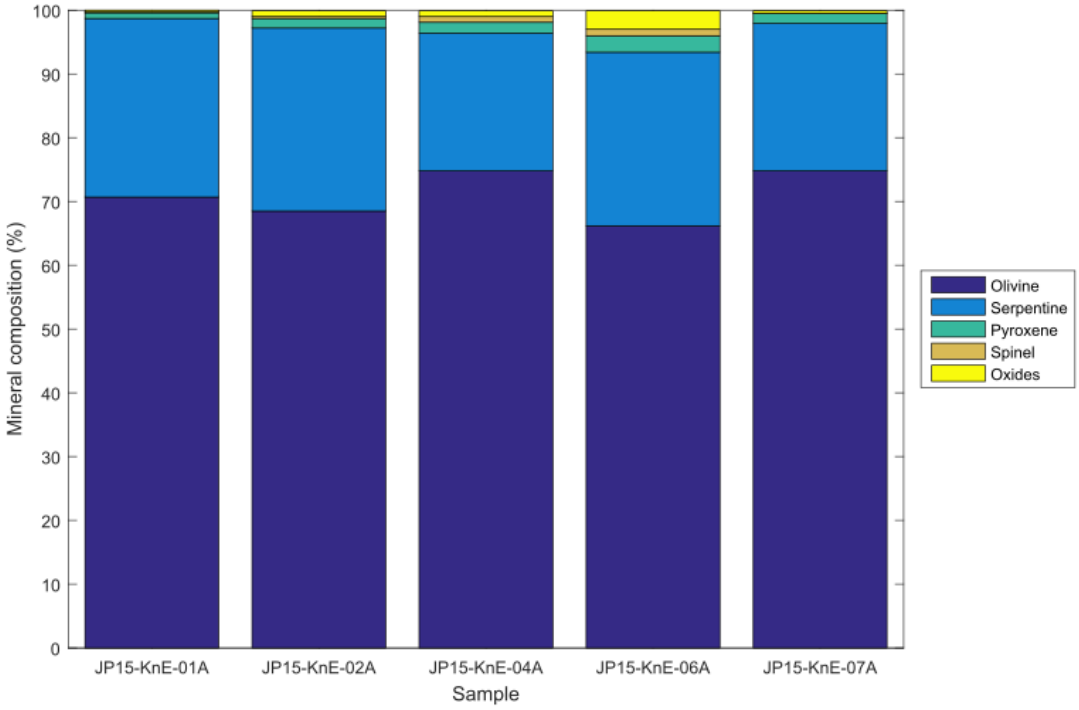

Figure 20. Modal distribution of minerals of SZ A samples. The shear zone center is essentially homogeneous with 66-75% olivine and < 3% pyroxene.

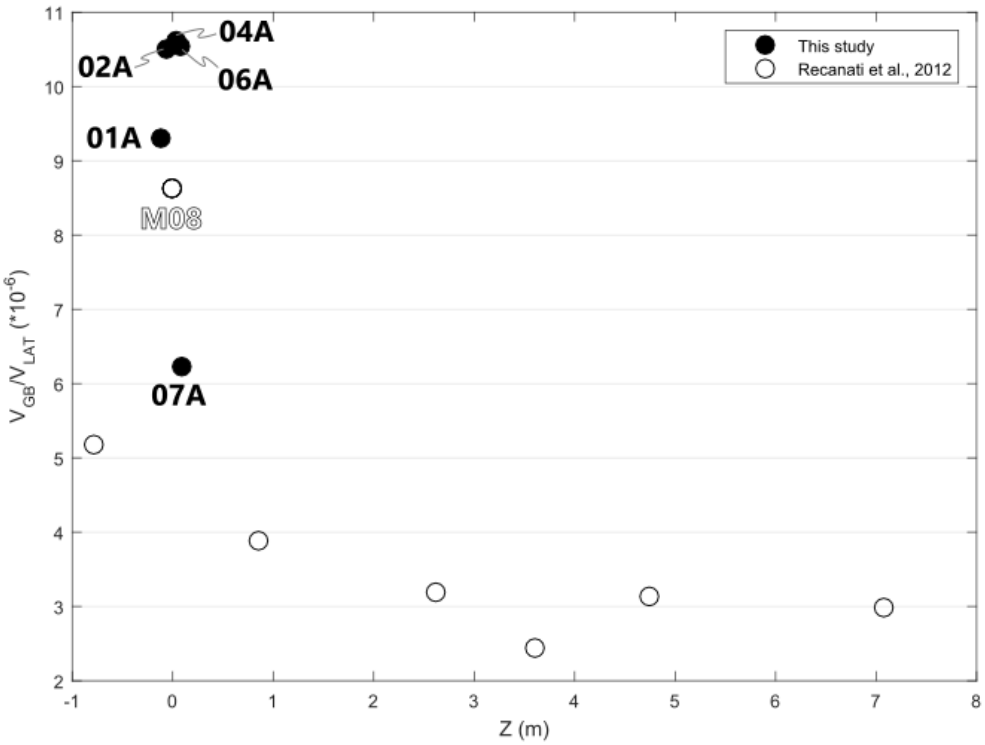

Figure 21. V_{GB}/V_{LAT} ratios across SZ A shows that the highest V_{GB}/V_{LAT} values are located in the shear zone center, where grain sizes are smallest and a larger volume of grain boundaries are present.

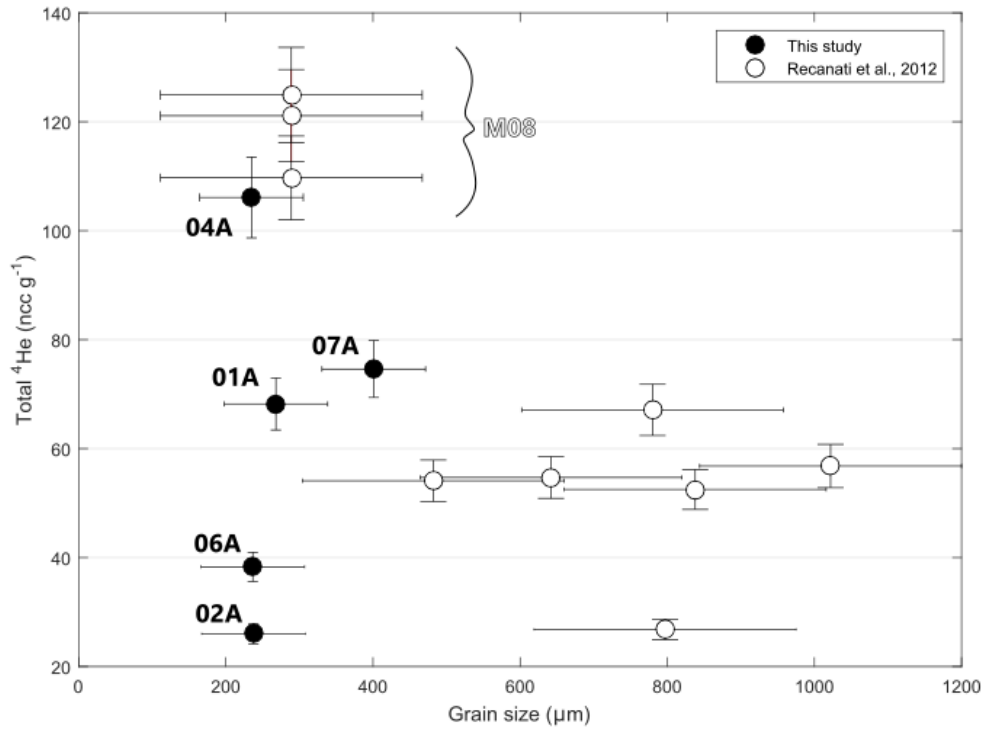

Figure 22. A loose correlation exists between decreasing grain size and increasing total concentration of ^{4}He, potentially indicating that as mean grain size reduces, the volume of grain boundaries increases, resulting in more numerous sinks for helium. Two outliers, 02A and 06A, disrupt this trend, which may have implications for the behavior of helium storage directly outside the shear zone.

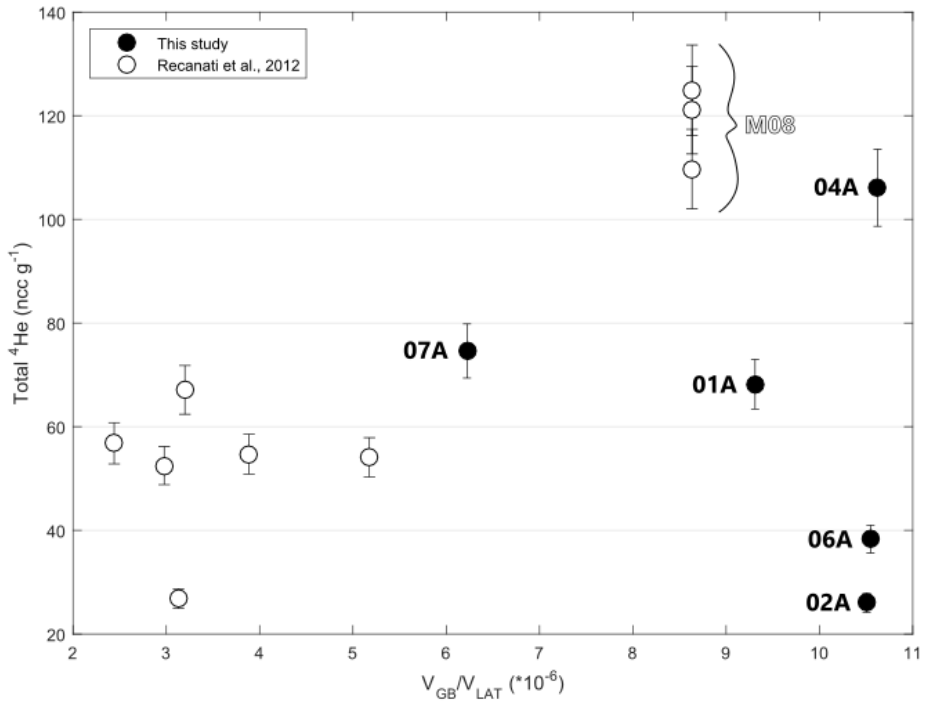

Figure 23. Total ^{4}He concentration generally increases as a function of V_{GB}/V_{LAT}, suggesting that in most samples where grain boundary volume increases, more He is stored. However, 02A and 06A do not follow this trend, indicating that despite increased storage capacity, He concentrations are not as high in these samples.

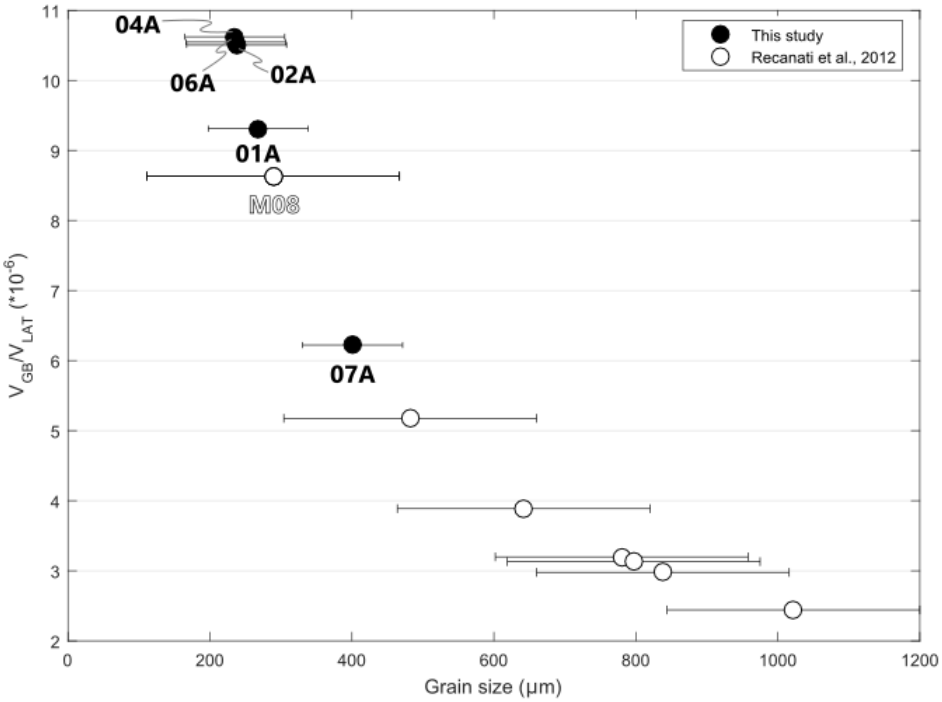

Figure 24. V_{GB}/V_{LAT} versus grain size in SZ A. As V_{GB}/V_{LAT} is calculated directly from grain size, the inverse relationship demonstrated here simply reiterates the fact that an increase in grain size reduces the ratio of grain boundary to grain lattice volume.

4.2.2 Shear zone B

The greatest value of α outside of SZ B is 16º and at the center is 1º, resulting in a maximum total shear strain of 13555% (Fig. 25). We calculate a maximum strain in SZ B that is significantly higher than for SZ A due to the slightly smaller deflection angle of the centermost sample. However, it is also likely that there is error associated with deflection angle measurement; we estimate that errors in our field measurements could be up to ±3º. SZ B samples appear mineralogically similar to SZ A samples in thin section, so we did not assess mineral modes with BSE maps.

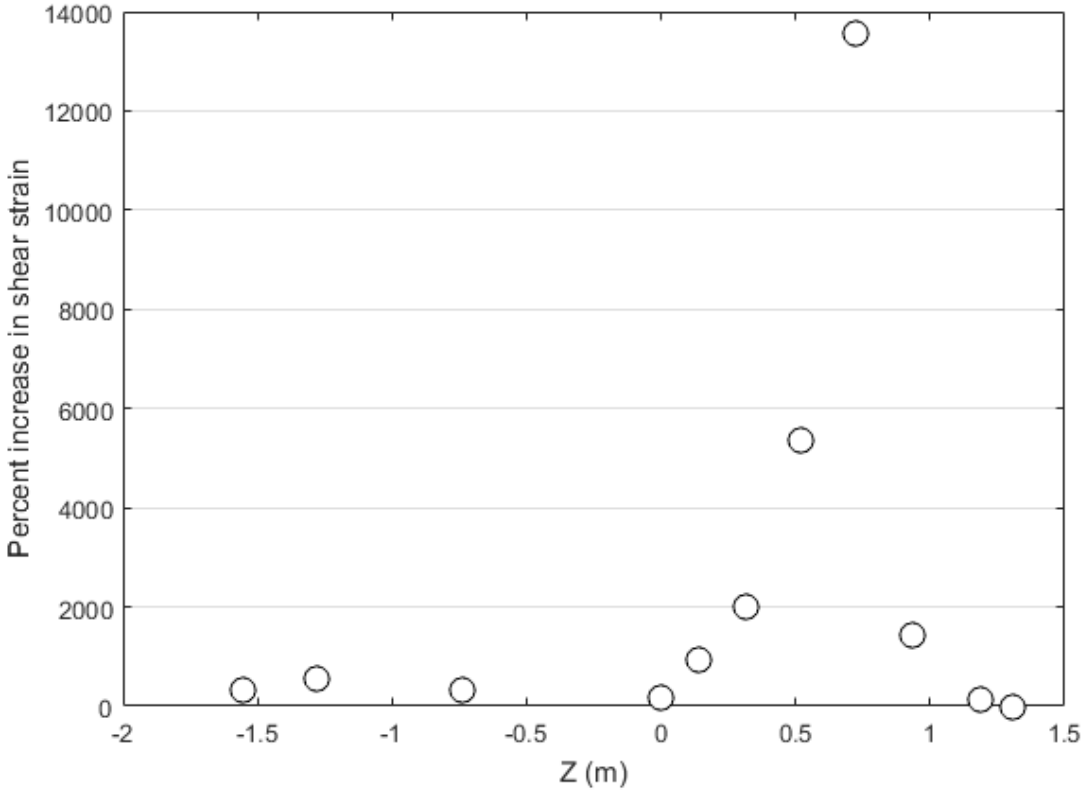

Figure 25. Consistent with SZ A, highest shear strain in SZ B indicates shear zone center and, thus, the structural center observed in the field (0 m) does not correlate with highest strain, placing the true shear zone center at ~0.7 m.

4.3 Numerical model results

We conducted two sets of model runs to test helium diffusion behavior under varying conditions. The first set of simulations were run until they reached a maximum strain of 140, consistent with the largest calculated strain in the Josephine shear zones. These tests produced minimum grain sizes of ~565 μm at the center, much larger than seen in the Josephine

Peridotite. The second set of simulations were run until the predicted minimum grain size reached 200 μm, consistent with the minimum measured grain size in SZ A. In these grain size-limited runs, maximum strains reached ~328, but depend upon the imposed shear rate. For each set of simulations, boundary velocities were varied from 1 to 8 m yr^{-1}. In all simulations, velocity profiles (Fig. 26) demonstrate localization of shearing at the center, occurring more rapidly with faster rates of deformation. Resulting temperatures reach higher values in the shear zone center with increasing velocities, ranging from 987 to 1375 ºC (1260 to 1648 K, corresponding to velocities to 0.1 and 8 m yr^{-1}, respectively). These temperatures are approximately within the range estimated for deformation of the Josephine Peridotite (915-1365 ºC; *Evans*, 1987). Minimum viscosities at the center of the shear zone vary with shear rate, from 1×10^{17} to 2×10^{15} Pa s for velocities of 1 and 8 m yr^{-1}, respectively. The deformation conditions of the modeled shear zone initially fall into dislocation creep, resulting in a negative rate of grain size evolution (i.e., decreasing grain size; Fig. 29). Faster initial velocities lead to a greater rate of grain size reduction (Fig. 31), and those cases reach the minimum grain size faster (due to shorter model time).

Helium diffusion coefficients increase towards the shear zone center, due to the imposed concentration gradient, reduction in grain size, and shear localization. The coefficient of grain boundary diffusion indicates that helium diffuses faster in boundaries than in lattices by about two orders of magnitude, and the bulk diffusion coefficient, calculated from these two factors (Eq. 16), reaches a maximum rate at the shear zone center (1×10^{-11} and 4×10^{-12} m^2 s^{-1} in grain size- and strain-limited runs, respectively). Helium concentration calculated by these diffusion coefficients shows total ^{4}He evolving towards the imposed center concentration of zero. The general pattern of helium concentration in our models displays similar lows to those observed in the Josephine samples. However, the width of these lows is much larger than observed in the Josephine shear zones, suggesting that, if melt-controlled diffusion is responsible for the observed helium concentrations, melt was present in the shear zone for a shorter period of time.

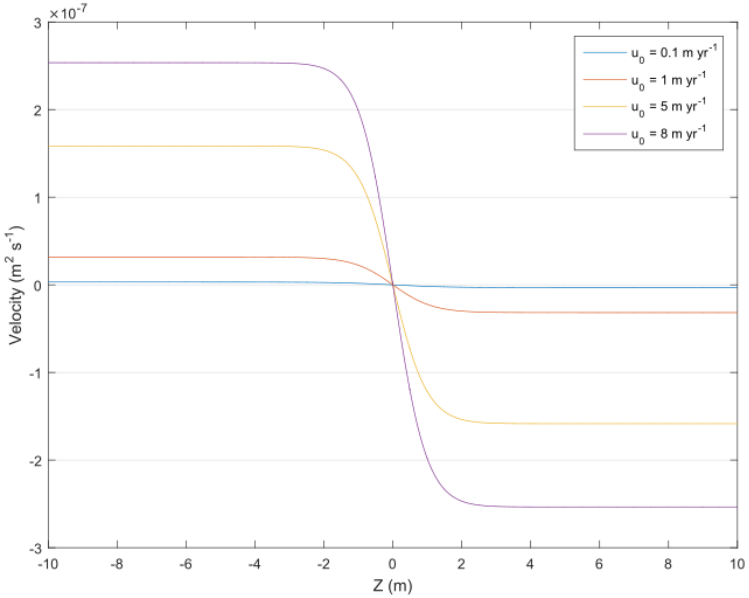

Figure 26. Velocity profile of model runs; faster initial shearing velocities localize more rapidly and result in faster deformation.

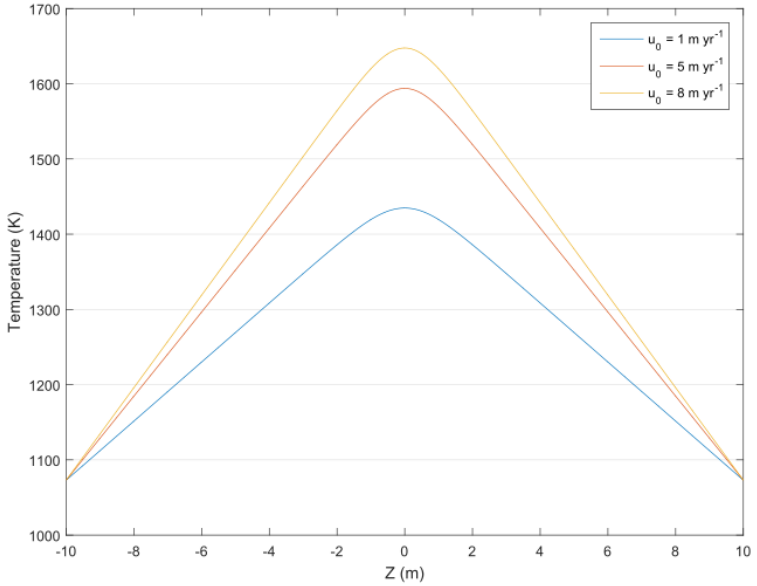

Figure 27. Due to faster shear localization, model runs with faster initial velocities reach higher temperatures at the shear zone center.

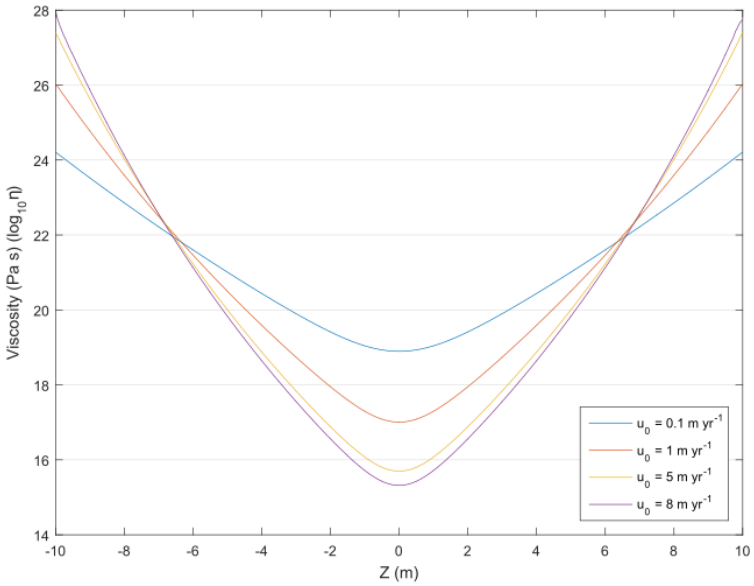

Figure 28. Viscosity, which is both velocity- and temperature-dependent, reaches lower viscosities in model runs with faster initial velocities.

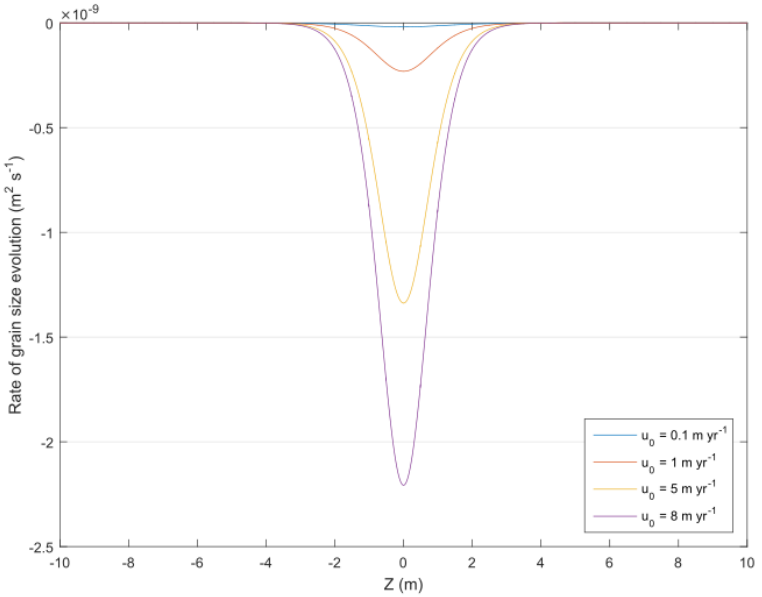

Figure 29. Evolution rates vary between model runs; faster initial shearing velocities result in a faster rate of grain size reduction.

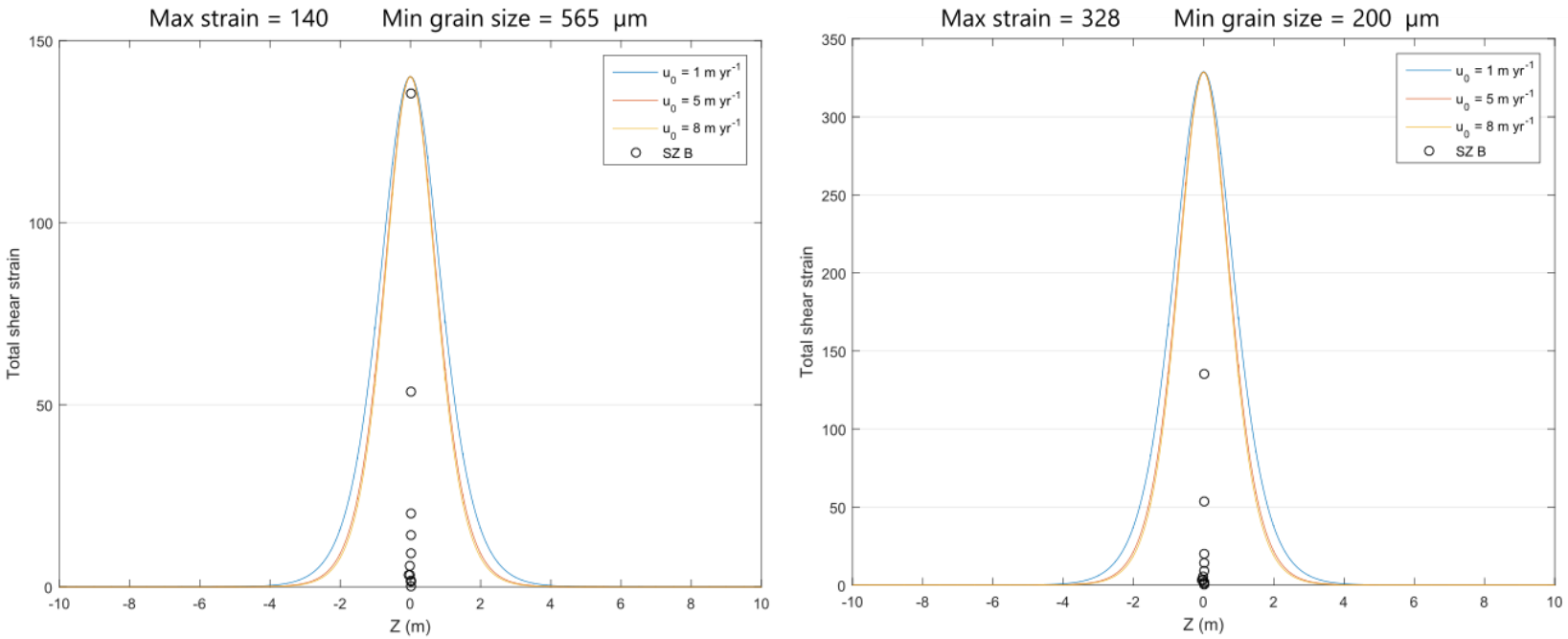

Figure 30. SZ B total strain overlaid on model results of strain-limited (left) and grain size-limited (right) experiments. The limiting strain in the first panel was taken from SZ B, which reached the highest strain seen in either Josephine shear zone (~140). However, when allowing the model to evolve to minimum grain sizes similar to SZ A (200 µm), total shear strain in the shear zone center reached ~330.

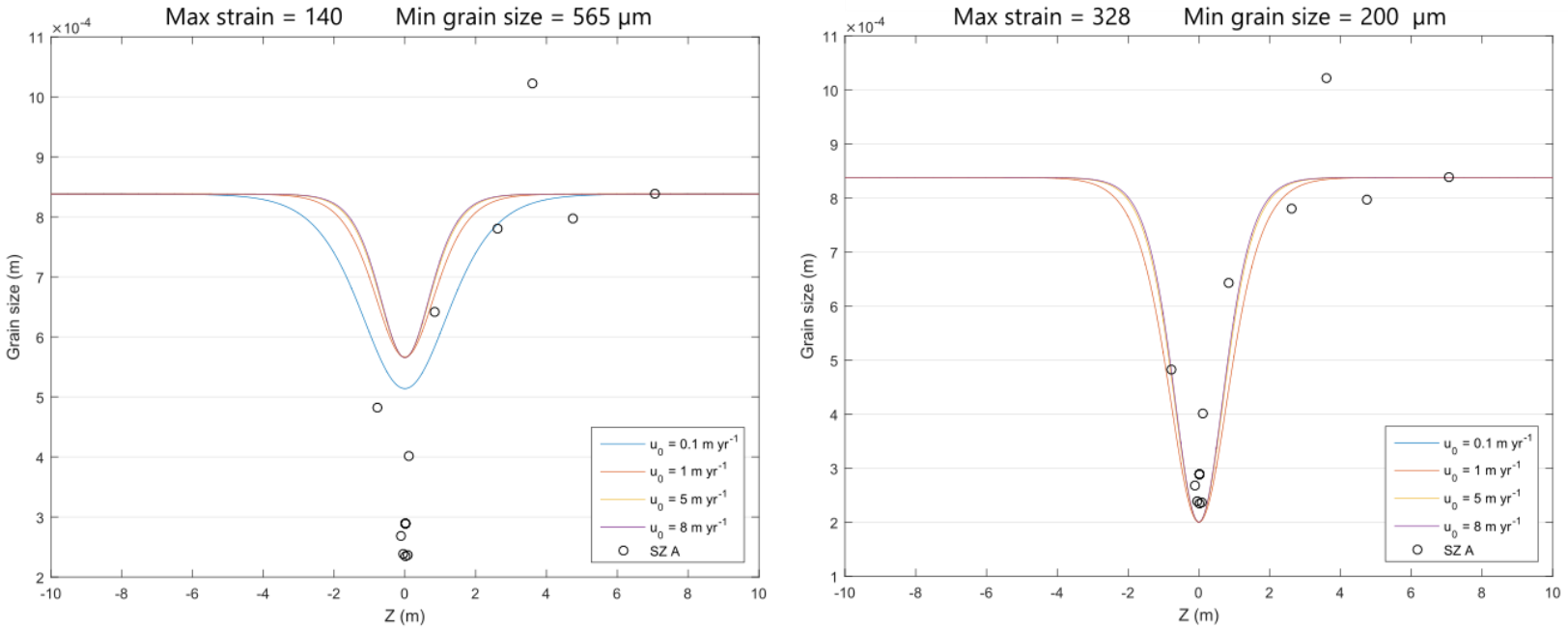

Figure 31. SZ A grain size overlaid on model results of strain-limited (left) and grain size-limited (right) experiments. The strain-limited runs reach a minimum grain size of 565 µm, compared to the smallest grain size seen in SZ A, 234 µm. The grain size-limited runs show that strain must reach values >300 to achieve the grain sizes seen in our Josephine samples. Because the grain size-limited runs were allowed to run until minimum grain size reached 200 µm, these results more accurately match the SZ A samples.

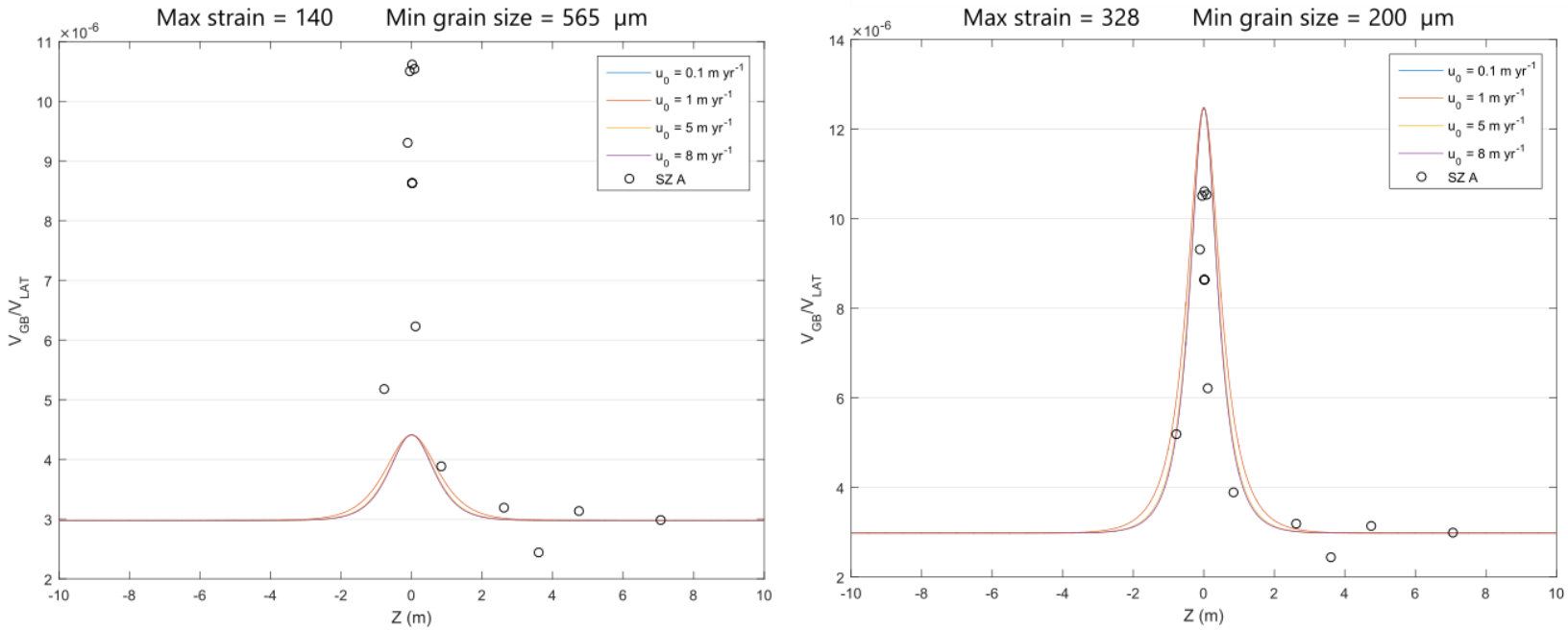

Figure 32. SZ B V_{GB}/V_{LAT} overlaid on model results of strain-limited (left) and grain size-limited (right) experiments. Ratios of strain-limited results are significantly lower than those measured in SZ B.

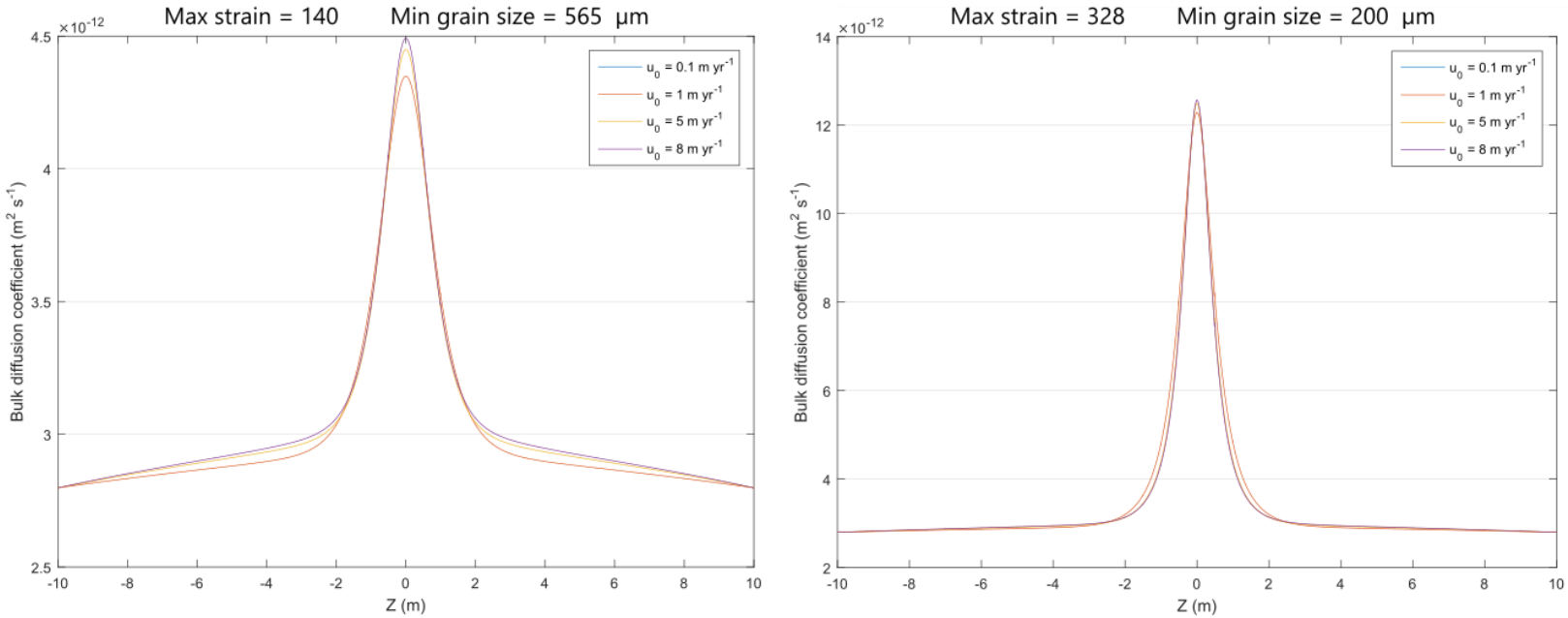

Figure 33. Bulk diffusion coefficient of strain-limited (left) and grain size-limited (right) runs (note different scales). Both experiments achieve diffusion coefficients of the same order, but the grain size-limited runs reach slightly higher values.

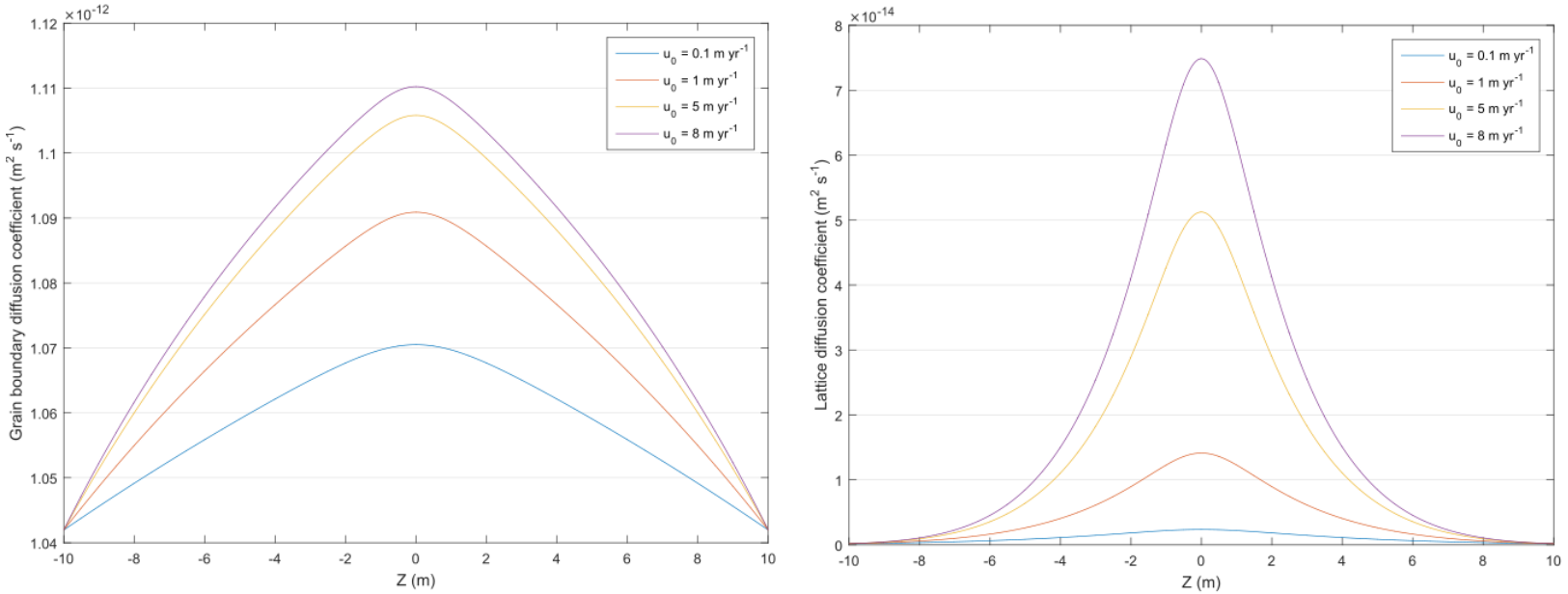

Figure 34. Diffusion coefficients of helium in grain boundaries (left) and lattices (right). Diffusion in grain boundaries is faster than in lattices by about two orders of magnitude at the deformation conditions of the Josephine Peridotite.

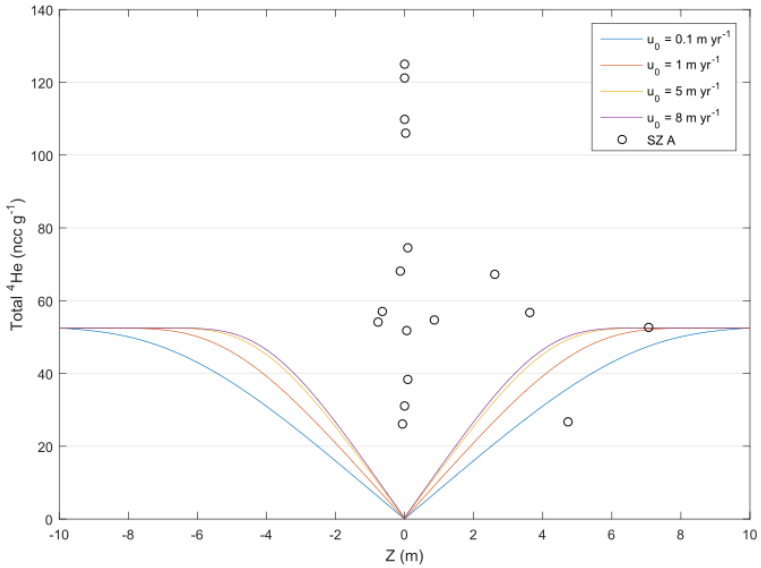

Figure 35. By setting a concentration of zero ^{4}He at Z=0, we create a melt channel in the shear zone center. Due to its incompatible nature, helium will preferentially diffuse into this melt and out of the material outside the shear zone. However, the shearing velocities tested do not accurately recreate the ^{4}He profile seen in SZ A. The shear zone center as defined by helium variation is ~0.2 m, but at the velocities shown here, such a narrow concentration gradient is not possible. Additionally, helium concentrations attained by our model cannot recreate the peak in ^{4}He at the shear zone center, where shear strain is highest.

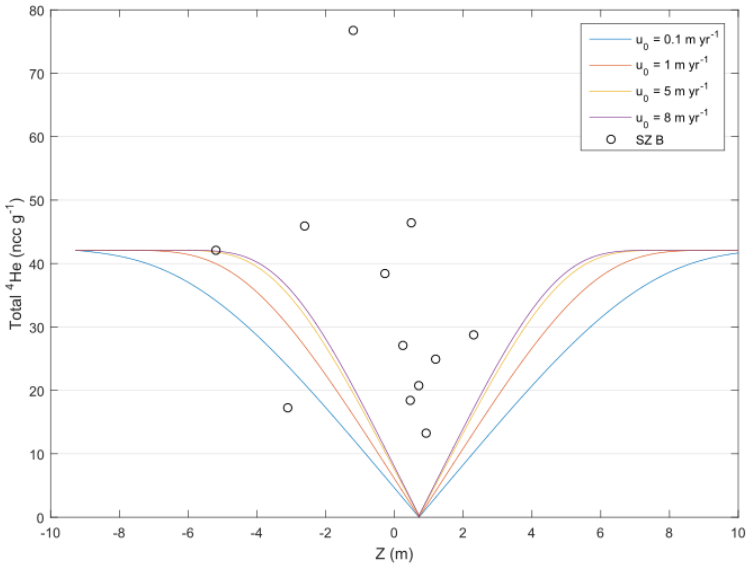

Figure 36. As in Fig. X, we define a concentration of zero ^{4}He at Z=0 to impose a melt channel in the shear zone center. Similar to SZ A, the velocities tested in our model cannot recreate the ^{4}He profile seen in SZ B: the variation in helium occurs over a distance of ~1 m, but the velocities tested here do not create such a narrow profile. The peak in in ^{4}He at the shear zone center, where shear strain is highest, also remains unexplained by the model.

5. Discussion

5.1 Helium in the Josephine Peridotite

Our bulk rock helium results from the Josephine Peridotite reveal the fine resolution behavior of helium concentration across a ductile mantle shear zone. Both SZ A and SZ B display helium concentration profiles with helium-depleted rock surrounding peaks in He concentration at the SZ center. Peaks in He concentration occur in locations with observed dunite, supporting the presence of He-enriched melt at the shear zone centers. The similar He pattern observed in both shear zones suggests the same processes likely control helium enrichment in both shear zones, and possibly at peridotite shear zones in general. The sharp variations we observe in total helium concentration have not been reported previously and, thus, provide new insight into the behavior of helium diffusion in ductile shear zones, as well as the He concentration of melts traversing these shear zones and potentially erupting on the surface.

Based upon our observations of significant helium enrichment in shear zone centers and helium depletion in rocks bordering shear zone centers, we suggest that the presence of a liquid melt phase (either transported from the mantle or due to temperatures greater than the peridotite solidus) initiates He diffusion from the surrounding rock into the melt, effectively stripping He out of the country rock. Creating the observed helium concentration variability with such a process, however, requires rapid, short-lived diffusion of helium into the melt, followed by prompt cooling after the cessation of shearing and melt transport, in order to trap mobile helium in the shear zone center. Such a situation would require a decrease from deformation temperatures of ~1100 ºC to below the He closure temperatures in olivine (224-273 ºC, Appendix E; *Baxter*, 2010) to prevent further diffusion (although rates do decrease exponentially with decreasing temperature).

5.1.1 Implications for helium storage

Our observations provide new constraints on the storage locations of helium in the Josephine Peridotite shear zones. Crushing experiments release helium stored in grain boundaries, subgrain boundaries, and preexisting cracks, while melting releases helium in grain matrices, inclusions, and dislocations. However, in both shear zones in this study, total ^{4}He released by crushing is 4-15%. While studies suggest that grain boundaries can

potentially store large volumes of gas, our crushing and melting experiments demonstrate that a majority of helium in samples is released during melting; large amounts of He are instead stored within grain matrices. Therefore, our data do not support the theory that grain boundaries store a significant volume of noble gases in ductilely deformed rocks, despite the increased grain boundary volume at shear zone centers.

Although we are unable to definitively determine helium storage locations within the grain matrix, crushing and melting experiments suggest that in our samples, a majority of total ^{4}He is stored within grains. Three likely sites for helium storage includes vacancies or point defects in the grain lattice, dislocation defects (linear orientations of point defects), and fluid or melt inclusions. We cannot comment on storage in point defects, as atomic-level vacancies are difficult to identify and require electron microscopy. Dislocations are not expected to store a large volume of gas either; *Recanati et al*. (2012) found that dislocation density varied by < 10% in the four samples they examined and that densities were slightly lower in their most deformed sample (M08). They attribute these lower densities to "healing" of dislocations during dynamic recrystallization. Thus, dislocations and subgrain boundaries do not appear to be the primary locations of ^{4}He storage in highly deformed Josephine shear zones. Finally, helium may be stored in fluid or gas inclusions. We did not observe any visible inclusions in thin section at magnifications of 50x under optical microscopy, but we cannot definitively rule out the presence of small inclusions. However, if present, such small inclusions are unlikely to store a significant amount of gas (*Hiraga et al*., 2004; *Recanati et al*., 2012). In contrast to our results, studies at other locations find evidence of dislocations and inclusions storing some gas (e.g., *Heber et al*., 2007; *Burnard et al*., 2015), but these sites do not appear to store significant gases in the Josephine shear zones.

While samples of the Josephine Peridotite do not support experimentally-determined results of long-term grain boundary residence sites, it is possible that ^{4}He concentrations in boundaries were preserved over shorter time-scales. While the deformation history of the Josephine Peridotite is not confirmed, it is possible that deformation of the shear zones in this study occurred entirely during the Nevadan Orogeny (155-135 Ma); helium within the system could have migrated out in the millions of years that followed. Closure temperatures of helium in olivine are low (224-273 ºC) and, assuming a conservative cooling rate of 20 ºC Ma^{-1} (typical of continental crust; *Turcotte and Schubert*, 2002), and the maximum estimated

temperature of deformation (1365 ºC), we can determine that it would take approximately 57 Ma to cool below the helium closure temperature. During that time, while temperatures are still high and helium is still mobile, it is extremely likely that helium could diffuse away from the system or between grain boundaries and lattices, residing in lattices for longer timescales. Helium concentrations seen in the Josephine shear zones may not be representative of the concentrations immediately after shearing.

From this information, we propose that dry grain boundaries are potential storage sites of noble gases on short timescales, but over longer periods (i.e. the time required for the Josephine Peridotite to cool after deformation, ~57 Ma), or if wetted, are unlikely to retain helium. Rather, any helium residing within grain boundaries would diffuse out of the shear zone or into grain lattices, and, thus, we suggest that long-term storage of helium occurs in lattices in the Josephine shear zones.

5.1.2 Complications in our diffusion conceptual model

In SZ A, samples 02A and 06A are outliers in nearly all relationships, providing inconsistencies that require explanation. Trends from SZ A suggest that as grain size decreases, grain boundary volume increases and theoretically provides additional storage for noble gases (long- or short-term as determined by wetted or dry grain boundaries, respectively). However, despite the small grain sizes of 02A and 06A (237 and 236 μm, respectively), similar to center sample 04A (234 μm), they contain 26.0 and 38.3 ncc g^{-1} total ^{4}He, compared to 04A with 106.1 ncc g^{-1} total ^{4}He. According to our conceptual model, 02A and 06A are characteristic of samples directly bordering the melt channel, represented by the dunite in SZ A. We proposed that the melt channel at the center of the shear zone would become enriched at the expense of the adjacent material, creating a helium profile across the shear zone center with low concentrations bordering an anomalously high helium concentration in the center, where helium became trapped after shearing ceased and the material cooled. This theory would explain the ^{4}He concentration of samples 02A and 06A, and the estimated ^{4}He concentration in our model produce a similar overall helium profile as in SZs A and B. The model ^{4}He concentration profile is, however, wider than that of SZs A and B, possibly suggesting that helium diffusion has occurred for too long in our simulations.

The other discrepancy requiring explanation from our Josephine shear zone samples is the disagreement in SZ B between the samples with the highest shear strain and highest ^{4}He concentration. Unlike in SZ A, in which the sample with the highest strain and highest ^{4}He concentration are the same, the highest helium concentration (76.8 ncc g^{-1} ^{4}He, D38) occurs outside the shear zone center as defined by shear strain. Within the center of SZ B, there is a smaller peak: this relatively enriched sample has a ^{4}He concentration of 46.5 ncc g^{-1} ^{4}He (D42), with samples of 13.3 ncc g^{-1} (D34) and 18.4 ncc g^{-1} (D40) ^{4}He on either side. These SZ B samples are similar to the trend in SZ A and thus we assume that D38 is an anomaly not explained by our conceptual model of helium diffusion within the shear zone. We suspect that this second peak could be the resulted of a second finger of melt, not directly correlated with the region of maximum strain. From the previous data, we conclude that our current model cannot predict all of the complexities seen in the Josephine shear zones, but that other processes likely play a role in the evolution of helium within the Josephine shear zones.

5.2 Numerical Model

Our combined results of helium in the Josephine Peridotite shear zones and helium diffusion and concentration in our numerical results support our conceptual model. However, the width of depleted He concentrations bordering the shear zone center as estimated by our model is inconsistent with the Josephine shear zone concentrations. This incongruity suggests that it is unlikely that melt was present throughout the entire shearing process, but instead was present for a brief period of time. Two alternative hypotheses driving diffusion of helium include:

1) The length of time over which deformation occurs is far less than we initially suspected; shearing does not last long enough to allow helium concentrations to approach steady-state, producing narrow ^{4}He concentration profiles as seen in the Josephine shear zones, or
2) At the beginning of deformation, there is no melt present in the shear zone. During deformation, the maximum temperature at the shear zone center reaches the peridotite solidus temperature and localized melting occurs, initiating helium diffusion.

In hypothesis (1), we suggest that faster shearing velocities would reduce the shearing time required to match observed strain and grain sizes. We can limit the length of deformation to determine how quickly to terminate shearing to produce a ^{4}He profile width similar to those seen in SZs A and B. The approximate helium profile widths we need to replicate are ~0.2 m in SZ A and ~1 m in SZ B; widths achieved in our model are ~8 m, suggesting that in our initial model, diffusion was either occurring too slowly or over too long of a period, allowing helium concnetrations to approach steady state and create a wider helium profile than observed in the Josephine Peridotite. At a shearing velocity of 1 m yr^{-1}, the time required to produce the helium profile widths observed in the Josephine shear zones is <6.5 years, corresponding to total shear strains of ≤0.5 (Fig. 37). Besides the fact that such a velocity is unrealistic, as plate velocities greater than ~0.2 m yr^{-1} are not observed on Earth (*Monroe et al*., 2007), the achieved total strain and temperature at the shear zone centers are not sufficient to match Josephine shear zone deformation conditions. While hypothesis (1) succeeds in reproducing the widths of helium profiles in the Josephine shear zones, the conditions under which they are achieved are unrealistic.

Hypothesis (2) requires that melt is not present in the shear zone at the onset of deformation, and is only produced once temperatures exceed the peridotite solidus. Studies have determined an empirical solution for the solidus temperature (i.e., *Hirschmann*, 2000; *Katz et al*., 2013), the temperature at which partial melt forms, based on experiments on natural and synthetic dry peridotites, defined as

$$T_{solidus} = aP^2 + bP + c\ , \qquad (34)$$

where *a*, *b*, *c* are regressed constants and *P* is the pressure on the system (GPa) (*Hirschmann*, 2000; *Katz et al*., 2013). Based on these parameters, at pressures estimated for deformation of the Josephine Peridotite, $T_{solidus}$ = 1151 – 1176 ºC. Assuming the lower bound, we allow the model to proceed and, once this temperature is reached, we impose a helium concentration of zero at the shear zone center to initiate helium diffusion. The simulation proceeds until a minimum grain size of 200 μm is reached; the resulting helium concentration profile is presented in Fig. 38. At a shear velocity of 5 m yr^{-1}, 12.7 ky of deformation are required to produce the required grain size, but this proves to be too long as helium concentrations reach steady state and, thus, do not replicate the profiles of the Josephine shear zones. While melting mantle material by evolving towards the solidus temperature may not be a plausible

hypothesis, the presence of a melt within the shear zone center is still not completely out of the question. An alternative version of hypothesis (2) involves the injection of melt, from the mantle, through the shear zone, initiating helium diffusion. Unlike the melt channel in our conceptual model, this melt flux would be a short-term event, residing in the shear zone for a brief period of time, which would limit the amount of helium diffusion and potentially produce narrow helium profiles characteristic of SZs A and B. This process incorporates a body of melt, such as the dunite samples in SZs A and B, which would temporarily initiate helium diffusion, and could be frozen in place if shear zone temperatures rapidly dropped. This melt is then enriched in helium at the expense of the material directly adjacent to it.

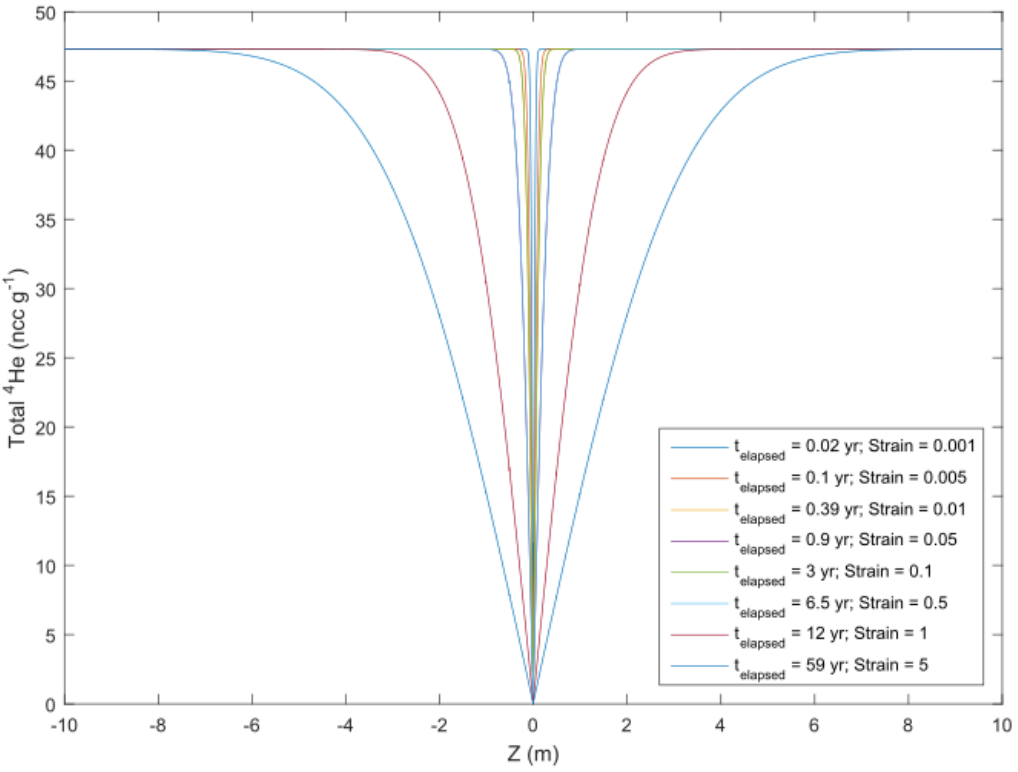

Figure 37. Results of hypothesis (1), in which we assume that the width of Josephine helium concentration profiles are due to rapid shearing over short time periods. At a shearing velocity of 1 m yr^{-1}, the helium profiles of SZs A and B are achieved after elapsed times of 0.1 and 6.5 years, respectively. These time scales correspond to extremely low total strains, which cannot produce the minimum grain sizes observed in the Josephine Peridotite.

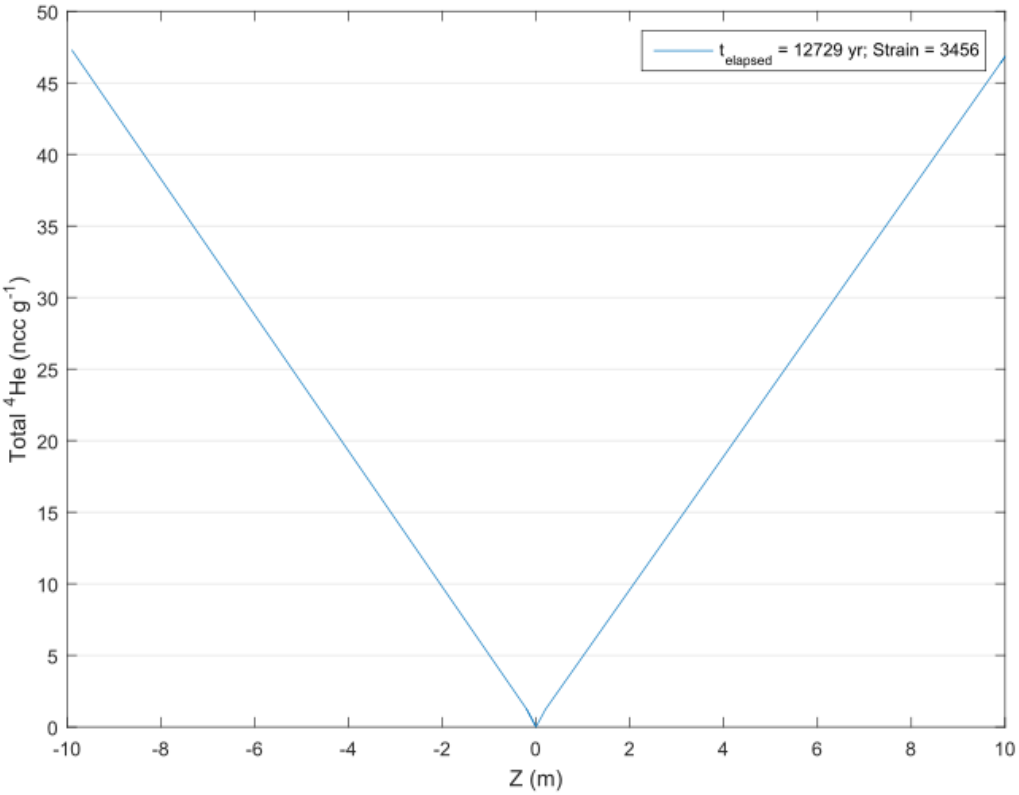

Figure 38. Experiments in which helium diffusion is initiated by surpassing the peridotite solidus results in a steady state concentration. This simulation proceeds for >12 ky, until the minimum grain size reaches 200 μm. The resulting helium profile is not consistent with SZs A and B.

5.3 Helium isotopes

Isotopic ratios are useful in determining the origin of mantle material, and $^{3}He/^{4}He$ values of both Josephine shear zones suggest they have a similar mantle source, with comparable mean crush ratios (SZ A: 6.48 ± 0.12 Ra; SZ B: 6.20 ± 0.13 Ra). Similar to *Recanati et al*. (2012), we suggest that these isotopic values indicate a predominately mantle source for the Josephine Peridotite, likely derived during a period of residence within a fore-arc mantle wedge or a beneath a back-arc basin spreading ridge, as proposed by *Recanati et al*. (2012). In contrast, SZ B has significantly higher melting $^{3}He/^{4}He$ values (9.74 ± 0.12 Ra) than SZ A (7.89 ± 0.10 Ra), suggesting that SZ B samples have a higher concentration of cosmogenic ^{3}He trapped within grain matrices (*Kurz*, 1986; *Recanati et al*., 2012) and are slightly more enriched in ^{3}He than the typical MORB (*Anderson*, 1998; *Farley and Neroda*, 1998).

6. Conclusions

Although our numerical and conceptual models cannot exactly replicate the complex behavior of helium in SZs A and B, they do allow us to constrain the potential conditions of deformation and provide further insight into the processes causing helium enrichment. ^{4}He concentrations from shear zones in the Josephine Peridotite, combined with our numerical model of a 1D shear zone, allow us to analyze the variation in helium behavior in regions of high strain. Both SZs A and B demonstrate the correlation between high shear strain and elevated helium concentrations, suggesting that mantle deformation leads to increased noble gas concentrations. During deformation, localized velocities at the shear zone center increase the total shear strain of the system, placing the deformation regime within dislocation creep, which results in an overall grain size reduction. While the major control on helium diffusion is the presence of melt, diffusion is possibly aided slightly by the decrease in grain size and consequent increased in grain boundary volume, which may be wetted by the presence of the melt.

The narrow helium profiles of the Josephine shear zones suggest that helium diffusion was short-lived and potentially initiated by the injection of a small volume of mantle melt into the shear zone. The incompatibility of helium leads to the diffusion of helium into this melt phase, subsequently depleting the nearby country rock. We speculate that diffusion was followed shortly by rapid cooling, which effectively froze the helium concentrations into the dunite and harzburgite of the Josephine shear zones. The effect of deformation on the helium concentrations of mantle material suggests that samples erupted on the surface may not accurately represent their upper mantle source.

References

Anderson, D.L., 1998. A model to explain the various paradoxes associated with mantle noble gas geochemistry. Proc. Natl. Acad. Sci., 95, 9087–9092.

Austin, N.J., Evans, B., 2007. Paleowattmeters: A scaling relation for dynamically recrystallized grain size. Geology, 35(4), 343–346.

Ballentine, C.J., van Keken, P.E., Porcelli, D., Hauri, E.H., 2002. Numerical models, geochemistry, and the zero-paradox noble gas mantle. Phil. Trans. R. Soc. Lond., 360, 2611-2631; doi: 10.1098/rsta.2002.1083.

Baxter, E.F., Asimow, P.D., Farley, K.A., 2007. Grain boundary partitioning of Ar and He. Geochimica et Cosmochimica, Acta 71, 434–451.

Blard, P.H., Puchol, N., Farley, K.A., 2008. Constraints on the loss of matrix-sited helium during vacuum crushing of mafic phenocrysts. Geochimica et Cosmochimica Acta, 72 (15), 3788–3803.

Braun, J., Chéry, J., Poliakov, A., Mainprice, D., Vauchez, A., Tomassi, A., Daignières, M., 1999. A simple parameterization of strain localization in the ductile regime due to grain size reduction: A case study for olivine. Journal of Geophysical Research, 104, 25167-25181.

Burnard, P., 2004. Diffusive fractionation of noble gases and helium isotopes during mantle melting. Earth and Planetary Science Letters, 220, 287-295.

Burnard, P., Graham, D., Farley, K., 2004. Fractionation of noble gases (He, Ar) during MORB mantle melting: a case study on the Southeast Indian Ridge. Earth and Planetary Science Letters, 227, 457– 472.

Burnard, P.G., Demouchy, S., Delon, R., Arnaud, N.O., Marrocchi, Y., Cordier, P., Addad, A., 2015. The role of grain boundaries in the storage and transport of noble gases in the mantle. Earth and Planetary Science Letters, 430, 260–270.

Cherniak, D.J., Watson, E.B., 2012. Diffusion of helium in olivine at 1 atm and 2.7 GPa. Geochimica et Cosmochimica Acta, 84, 269–279.

Coulton, A.J., Harper, G.D., O'Hanley, D.S., 1995. Oceanic versus emplacement age serpentinization in the Josephine ophiolite: Implications for the nature of the Moho at intermediate and slow spreading ridges. Journal of Geophysical Research, 100, 22245-22260.

Cram, D.G., Zurob, H.S., Brechet, Y.J.M., Hutchinson, C.R., 2009. Modelling discontinuous dynamic recrystallization using a physically based model for nucleation. Acta Materialia, 57, 5218–5228.

Cross, A.J., Ellis, S., Prior, D.J., 2015. A phenomenological numerical approach for investigating grain size evolution in ductiley deforming rocks. Journal of Structural Geology, 76, 22-34.

Davies, G.F., 2010. Noble gases in the dynamic mantle. Geochemistry Geophysics Geosystems, 11(3); doi:10.1029/2009GC002801.

De Bresser, J.H.P., Peach, C.J., Reijs, J.P.J., Spiers, C.J., 1998. On dynamic recrystallization during solid state flow: effects of stress and temperature. Geophysical Research Letters, 25, 3457–3460.

De Bresser, J.H.P., Ter Heege, J.H., Spiers, C.J., 2001. Grain size reduction by dynamic recrystallization: can it result in major rheological weakening? International Journal of Earth Sciences, 90, 28–45.

Dodson, M.H., 1973. Closure temperature in cooling geochronological and petrological systems. Contributions to Mineralogy and Petrology 40(3), 259-274.

Dohmen, R. and Milke, R., 2010. Diffusion in polycrystalline materials: Grain boundaries, mathematical models, and experimental data. Reviews in Mineralogy & Geochemistry, 72, 921-970.

Evans, J.G., 1987. Deformation of the Josephine Peridotite, California and Oregon. U.S. Geological Survey Professional Paper 1378.

Faul, U.H., Fitz Gerald, J.D., Farla, R.J.M., Ahlefeldt, R., Jackson, I., 2011. Dislocation creep of fine-grained olivine. Journal of Geophysical Research, 116; doi:10.1029/2009JB007174.

Fisher, J.C., 1951. Calculation of diffusion penetration curves for surface and grain boundary diffusion. Journal of Applied Physics, 22, 74-77; doi: 10.1063/1.1699825.

Futagami, T., Ozima, M., Nagal, S., Aoki, Y., 1993. Experiments on thermal release of implanted noble gases from minerals and their implications for noble gases in lunar soil grains. Geochimica et cosmochimica acta, 57 (13), 3177-3194.

Graham, D.W., 2002. Noble gas isotope geochemistry of mid-ocean ridge and ocean island basalts: Characterization of mantle source reservoirs. Reviews in mineralogy and geochemistry, 47 (1), 247-317.

Hall, C.E., Parmentier, E.M., 2003. Influence of grain size evolution on convective instability. Geochemistry Geophysics Geosystems, 4(3); doi:10.1029/2002GC000308.

Hansen, L.N., Zimmerman, M.E., Kohlstedt, D.L., 2011. Grain boundary sliding in San Carlos olivine: Flow law parameters and crystallographic-preferred orientation. Journal of Geophysical Research, 116; doi:10.1029/2011JB008220.

Hansen, L. N., Warren, J.M., 2015. Quantifying the effect of pyroxene on deformation of peridotite in a natural shear zone. Journal of Geophysical Research: Solid Earth, 120, 2717–2738.

Harper, G.D., 1984. The Josephine ophiolite, northwestern California. Geological Society of America Bulletin 95, 1009-1026.

Harper, G.D., Bowman, J.R., Kuhns, R., 1988. A field, chemical, and stable isotope study of subseafloor metamorphism of the Josephine ophiolite, California-Oregon. Journal of Geophysical Research, 93, 4625-4656.

Harper, G.D., Saleeby, J.B., Heizler, M., 1994. Formation and emplacement of the Josephine ophiolite and the Nevadan orogeny in the Klamath Mountains, California-Oregon: U/Pb zircon and $^{40}Ar/^{39}Ar$ geochronology. Journal of Geophysical Research, 99, 4293-4321.

Hart, S. R., 1984. He diffusion in olivine. Earth and planetary science letters, 70 (2), 297-302.

Hart, S.R., Kurz, M.D., Wang, Z., 2008. Scale length of mantle heterogeneities: Constraints from helium diffusion. Earth and Planetary Science Letters, 269, 508-517.

Heber, V.S., Brooker, R.A., Kelley, S.P., Wood, B.J., 2007. Crystal–melt partitioning of noble gases (helium, neon, argon, krypton, and xenon) for olivine and clinopyroxene. Geochimica et Cosmochimica Acta, 71, 1041–1061.

Herwegh, M., Berger, A., Ebert, A., Brodhag, S., 2008. Discrimination of annealed and dynamic fabrics: Consequences for strain localization and deformation episodes of large-scale shear zones. Earth and Planetary Science Letters, 276, 52-61.

Hiraga, T., Anderson, I.M., Kohlstedt, D.L., 2004. Grain boundaries as reservoirs of incompatible elements in the Earth's mantle. Nature, 427, 699-703.

Hiraga, T., Kohlstedt, D.L., 2009. Systematic distribution of incompatible elements in mantle peridotite: importance of intra- and inter-granular melt-like components. Contrib. Mineral. Petrol., 158, 149–167.

Hirschmann, M. M., 2000. Mantle solidus: experimental constraints and the effects of peridotite composition. Geochemistry, Geophysics, Geosystems, 1(10).

Hirth, G., Kohlstedt, D., 2003. Rheology of the upper mantle and the mantle wedge: A view from the experimentalists. Geophysical Monograph, 138; doi:10.1029/138GM06.

Honda, M., Patterson, D.B., 1999. Systematic elemental fractionation of mantle-derived helium, neon, and argon in mid-oceanic ridge glasses. Geochimica et Cosmochimica Acta, 63(18), 2863-2874.

Jackson, R.M., Parman, S.W., Kelley, S.P., Cooper, R.F., 2013. Constraints on light noble gas partitioning at the conditions of spinel-peridotite melting. Earth and Planetary Science Letters, 384, 178–187.

Karato, S., Toriumi, M., Fujii, T., 1980. Dynamic recrystallization of olivine single crystals during high-temrpeature creep. Geophysical Research Letters, 7(9), 649-652.

Karato, S., 1989. Grain growth kinetics in olivine aggregates. Tectonophysics 168, 255-273.

Karato, S., and Wu, P., 1993. Rheology of the Upper Mantle: A Synthesis. Science 260, 771-778.

Katz, R. F., Spiegelman, M., & Langmuir, C. H., 2003. A new parameterization of hydrous mantle melting. Geochemistry, Geophysics, Geosystems, 4(9); doi: 10.1029/2002GC000433.

Kelemen, P.B., Dick, H.J.B., 1995. Focused melt flow and localized deformation in the upper mantle: Juxtaposition of replacive dunite and ductile shear zones in the Josephine peridotite, SW Oregon. Journal of Geophysical Research, 100, 423-438.

Kohlstedt, D. L., Goetze, C., Durham, W. B., Vander Sande, J., 1976. New technique for decorating dislocations in olivine. Science, 191(4231), 1045-1046.

Kurz, M. D., Garcia, M. O., Frey, F. A., O'Brien, P. A., 1987. Temporal helium isotopic variations within Hawaiian volcanoes: basalts from Mauna Loa and Haleakala. Geochimica et Cosmochimica Acta, 51(11), 2905-2914.

Kurz, M.D., Warren, J.M., Curtice, J., 2009. Mantle deformation and noble gases: Helium and neon in oceanic mylonites. Chemical Geology, 266, 10-18.

Linckens, J., Bruijn, R.H.C., Skemer, P., 2014. Dynamic recrystallization and phase mixing in experimentally deformed peridotite. Earth and Planetary Science Letters, 388, 134–142.

Miller, M.M., and Saleeby, J.B., 1995. U-Pb geochronology of detrital zircon from Upper Jurassic synorogenic turbidites, Galice Formation, and related rocks, western Klamath Mountains: Correlation and Klamath Mountains provenance. Journal of Geophysical Research, 100, 18045-18058.

Monroe, J. S., Wicander, R., & Hazlett, R. W., 2007. Physical Geology: Exploring the Earth. Belmont: Thomson Brooks/Cole.

Montési, L.G.J., Hirth, G., 2003. Grain size evolution and the rheology of ductile shear zones: from laboratory experiments to postseismic creep. Earth and Planetary Science Letters, 211, 97-110.

Parman, S.W., Grove, T.L., 2004. Harzburgite melting with and without H_2O: Experimental data and predictive modeling. Journal of Geophysical Research, 109; doi:10.1029/2003JB002566.

Parman, S.W., Kurz, M.D., Hart, S.R., Grove, T.L., 2005. Helium solubility in olivine and implications for high $^3He/^4He$ in ocean island basalts. Nature 437, 1140-1143.

Pinilla, C., Davis, S.A., Scott, T.B., Allan, N.L., Blundy, J.D., 2012. Interfacial storage of noble gases and other trace elements in magmatic systems. Earth and Planetary Science Letters 319-320, 287–294.

Poirier, J.P. "Creep of crystals: High-temperature deformation processes in metals, ceramics, and minerals." Cambridge, Cambridge University Press: 1985

Precigout, J., Gueydan, F., Gapais, D., Garrido, C.J., Essaifi, A., 2007. Strain localisation in the subcontinental mantle—a ductile alternative to the brittle mantle. Tectonophysics, 445, 318–336.

Ramsay, J.G., Graham, R.H., 1970. Strain variation in shear belts. Can. J. Earth Sci., 7, 786–813.

Recanati, A., Kurz., M.D., Warren, J.M., Curtice, J., 2012. Helium distribution in a mantle shear zone from the Josephine Peridotite. Earth and Planetary Science Letters, 359-360, 162-172.

Riedel, M.R., Karato, S., 1997. Grain-size evolution in subducted oceanic lithosphere associated with the olivine-spinel transformation and its effects on rheology. Earth and Planetary Science Letters, 148, 27-43.

Savelieva, G. N., Sobolev, A. V., Batanova, V. G., Suslov, P. V., & Brügmann, G. (2008). Structure of melt flow channels in the mantle. Geotectonics, 42(6), 430-447.

Shaw, A.M., Hilton, D.R., Fischer, T.P., Walker, J.A., de Leeuw, G.A.M., 2006. Helium isotope variations in mineral separates from Costa Rica and Nicaragua: Assessing crustal contributions, timescale variations and diffusion-related mechanisms. Chemical Geology, 230, 124-139.

Shaw, A.M., Hilton, D.R., Fischer, T.P., Walker, J.A., de Leeuw, G.A.M., 2006. Helium isotope variations in mineral separates from Costa Rica and Nicaragua: Assessing crustal contributions, timescale variations and diffusion-related mechanisms. Chemical Geology, 230, 124–139.

Shimizu, I., 1998. Stress and temperature dependence of recrystallized grain size: a subgrain misorientation model. Geophysical Research Letters, 25, 4237–4240.

Shimizu, I., 2008. Theories and applicability of grain size piezometers: The role of dynamic recrystallization mechanisms. Journal of Structural Geology, 30, 899-917.

Shuster, D.L., Farley, K.A., Sisterson, J.M., Burnett, D.S., 2004. Quantifying the diffusion kinetics and spatial distributions of radiogenic ^{4}He in minerals containing proton-induced ^{3}He. Earth Planet. Sci. Lett., 217, 19–32.

Skemer, P., Warren, J.M., Hansen, L.N., Hirth, G., Kelemen, P.B., 2013. The influence of water and LPO on the initiation and evolution of mantle shear zones. Earth and Planetary Science Letters, 375, 222-233.

Sundberg, M., Hirth, G., Kelemen, P.B., 2010. Trapped melt in the Josephine Peridotite: Implications for permeability and melt extraction in the upper mantle. Journal of Petrology; doi:10.1093/petrology/egp089.

Thomas, J.B., Cherniak, D.J., Watson, E.B., 2008. Lattice diffusion and solubility of argon in forsterite, enstatite, quartz and corundum. Chemical Geology, 253, 1–22.

Tolstikhin, I., Kamensky, I., Tarakanov, S., Kramers, J., Pekala, M., Skiba, V., Gannibal, M., Novikov, D., 2010. Noble gas isotope sites and mobility in mafic rocks and olivine. Geochimica et Cosmochimica, Acta 74, 1436–1447.

Trull, T. W., Kurz, M. D., & Jenkins, W. J., 1991. Diffusion of cosmogenic ^{3}He in olivine and quartz: implications for surface exposure dating. Earth and Planetary Science Letters, 103(1-4), 241-256.

Trull, T.W., Kurz, M.D., 1993. Experimental measurements of 3He and 4He mobility in olivine and clinopyroxene at magmatic temperatures. Geochimica et Cosmochimica Acta ,57, 1313-1324.

Turcotte, D.L., Schubert, G. “Geodynamics: Second edition.” Cambridge: 2002.

Twiss, R.J., 1977. Theory and Applicability of a Recrystallized Grain Size Paleopiezometer. Pageophys., 115, 227-244.

Urai, J.L., Means, W.D., Lister, G.S., 1986. Dynamic recrystallization of minerals. Geophysical Monograph, 36.

Van der Wal, D., Chopra, P., Drury, M., Fitz Gerald, J., 1993. Relationships between dynamically recrystallized grain size and deformation conditions in experimentally deformed olivine rocks. Geophysical Research Letters, 20(14),1479-1482.

Wang, K., Brodholt, J., Lu, X., 2015. Helium diffusion in olivine based on first principles calculations. Geochimica et Cosmochimica Acta, 156, 145–153.

Warren, J.M., Hirth, G., 2006. Grain size sensitive deformation mechanisms in naturally deformed peridotites. Earth and Planetary Science Letters, 248, 438–450.

Watson, E.B., Baxter, E.F., 2007. Diffusion in solid-Earth systems. Earth and Planetary Science Letters, 253, 307–327.

Yamasaki, T., 2004. Localized rheological weakening by grain-size reduction during lithospheric extension. Tectonophysics, 386, 117–145.

Yuen, D.A., Fleitout, L., Schubert, G., Froidevaux, C., 1978. Shear deformation zones along major transform faults and subducting slabs. Geophys. J. R. Astr. Soc., 54, 93-119.

Appendix

Appendix A. Modal mineral compositions and grain size

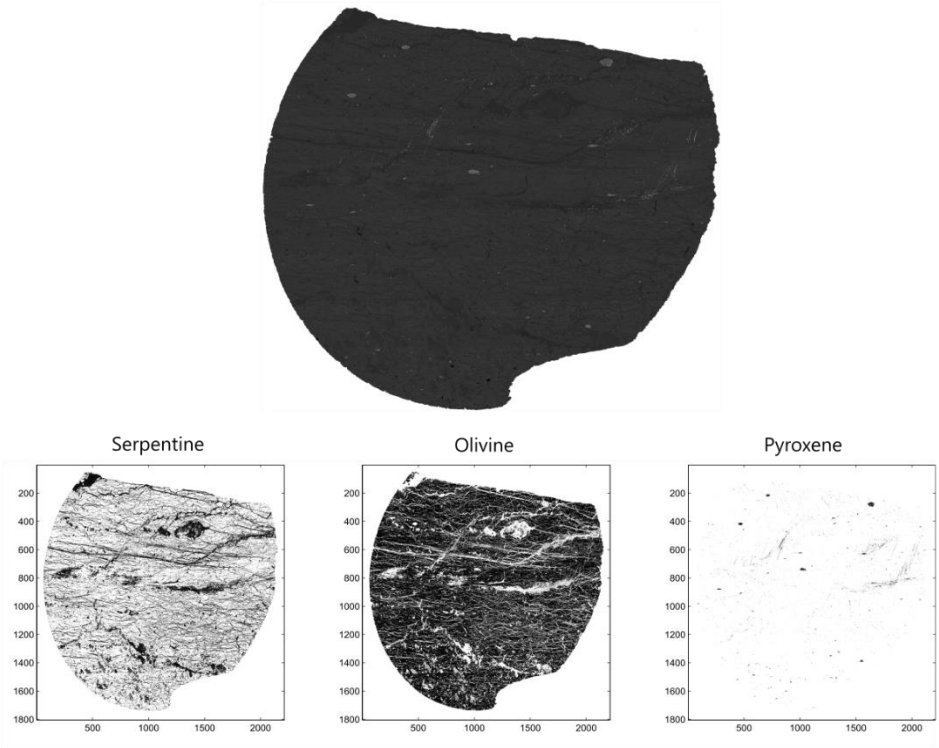

Figure A.1. JP15-KnE-01A back-scatter electron map and major mineral isolation maps.

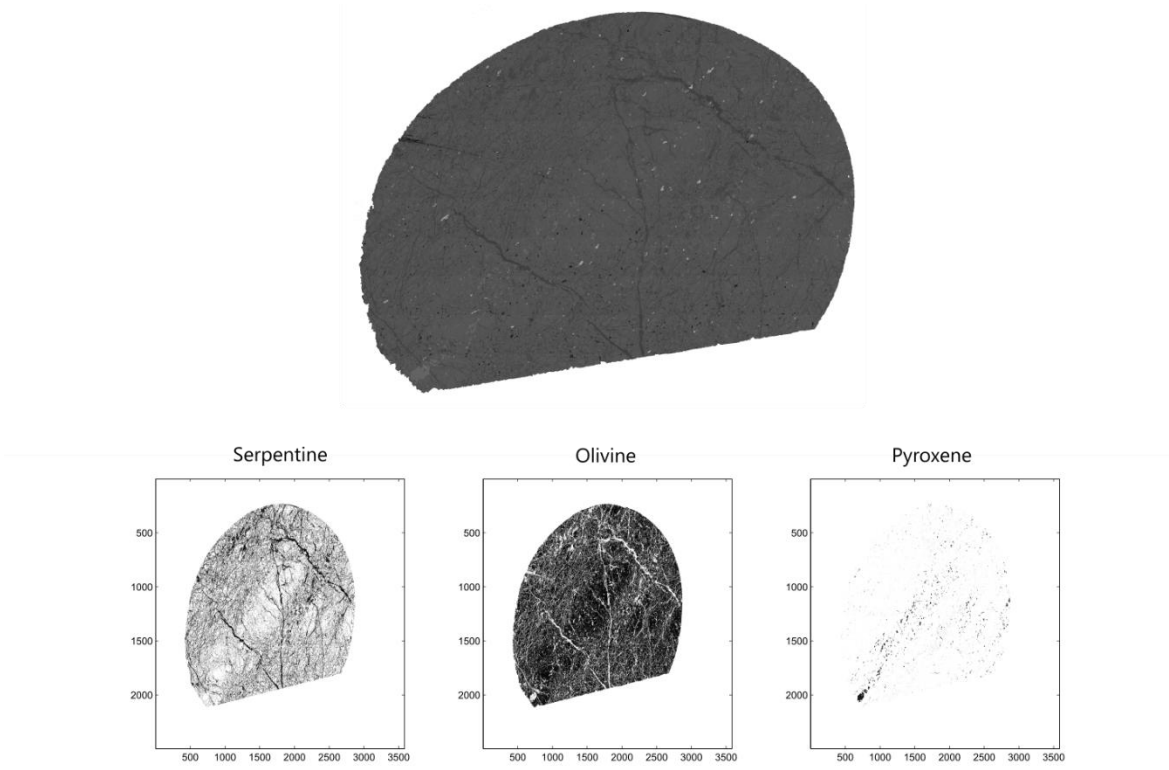

Figure A.2. JP15-KnE-02A back-scatter electron map and major mineral isolation maps.

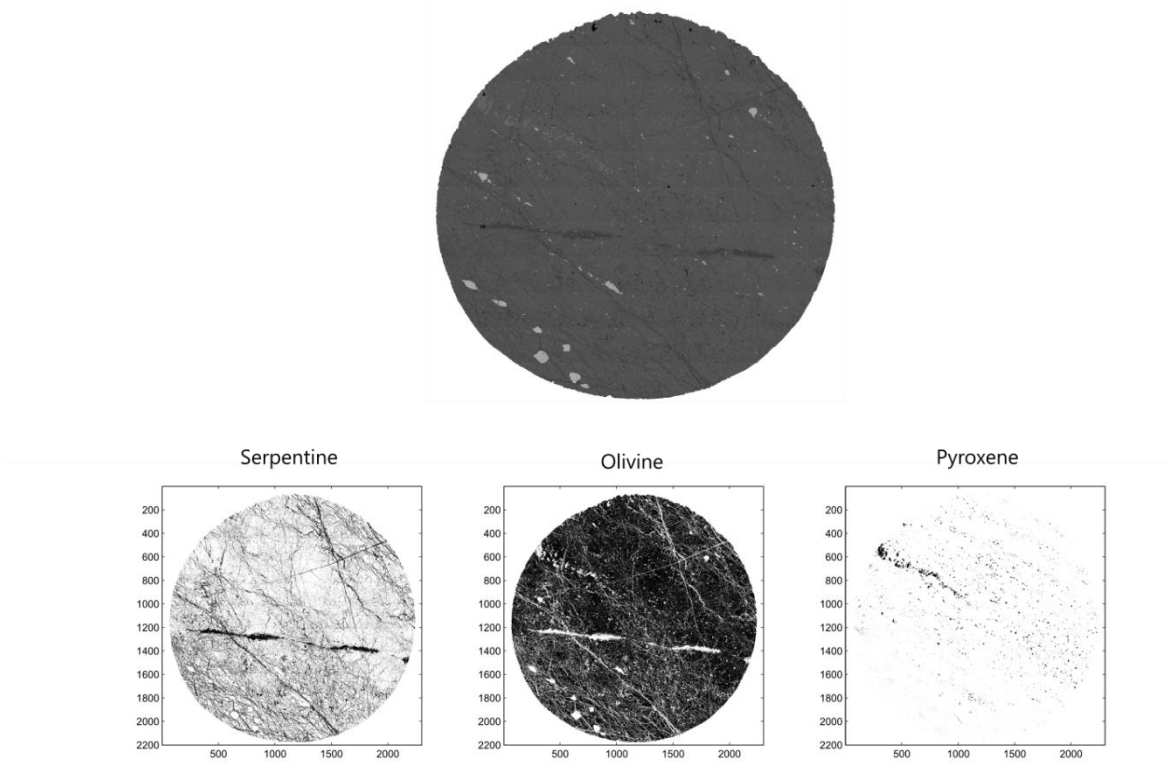

Figure A.3. JP15-KnE-04A back-scatter electron map and major mineral isolation maps.

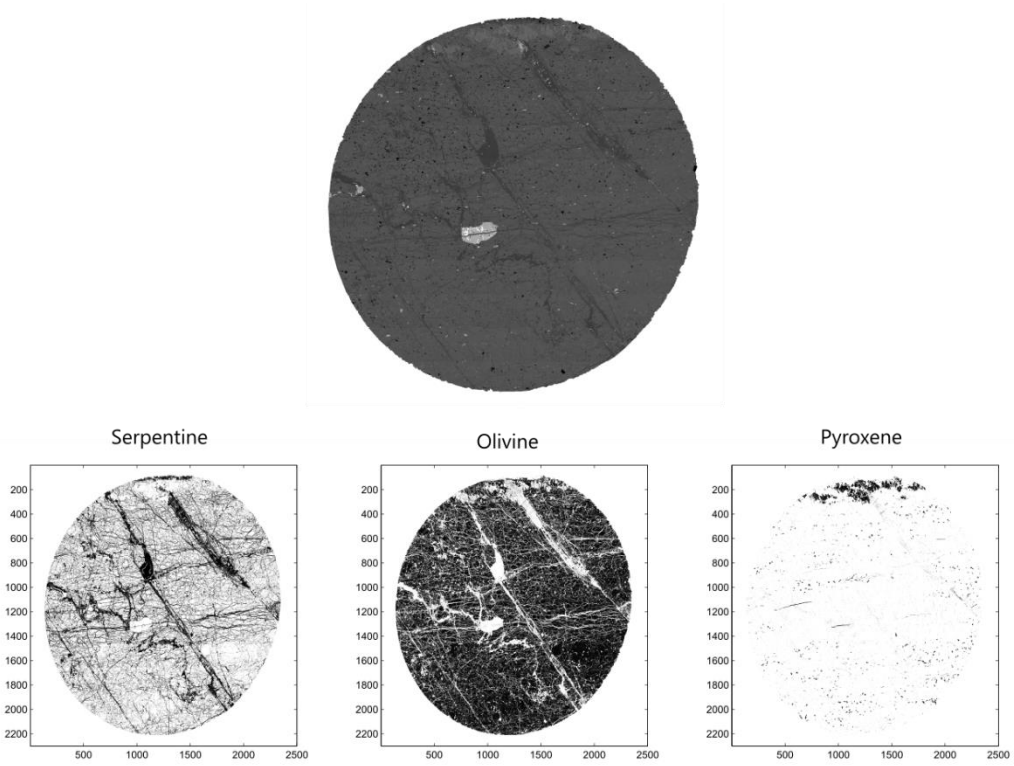

Figure A.4. JP15-KnE-06A back-scatter electron map and major mineral isolation maps.

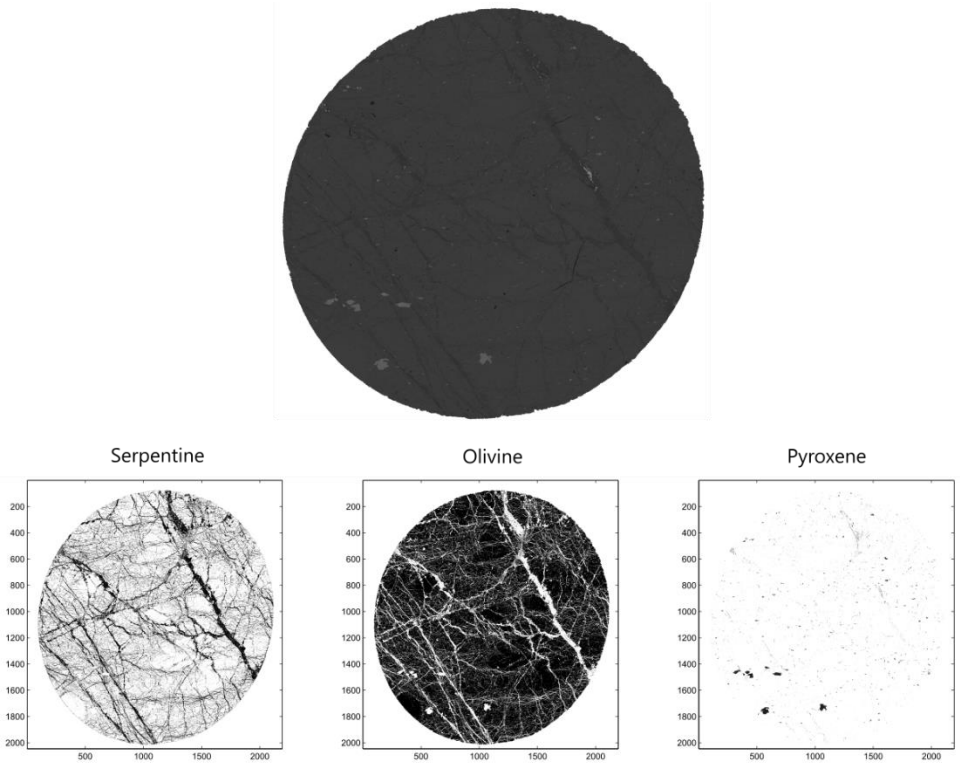

Figure A.5. JP15-KnE-07A back-scatter electron map and major mineral isolation maps.

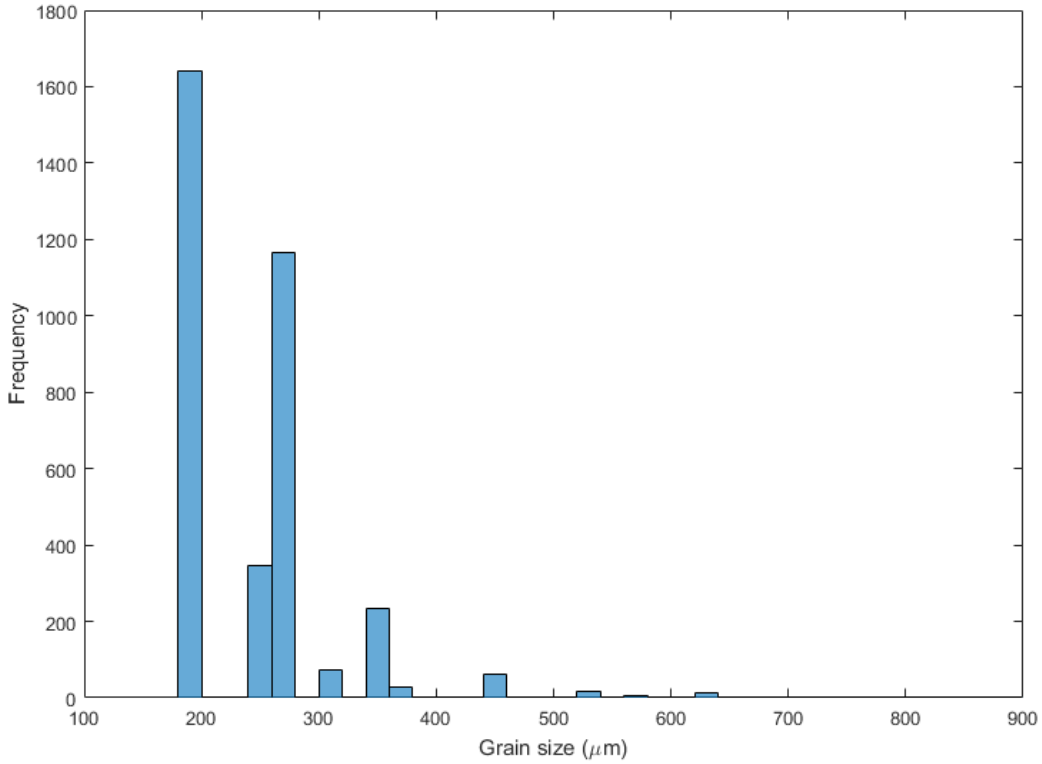

Figure A.6. Grain size distribution of JP15-KnE-01A.

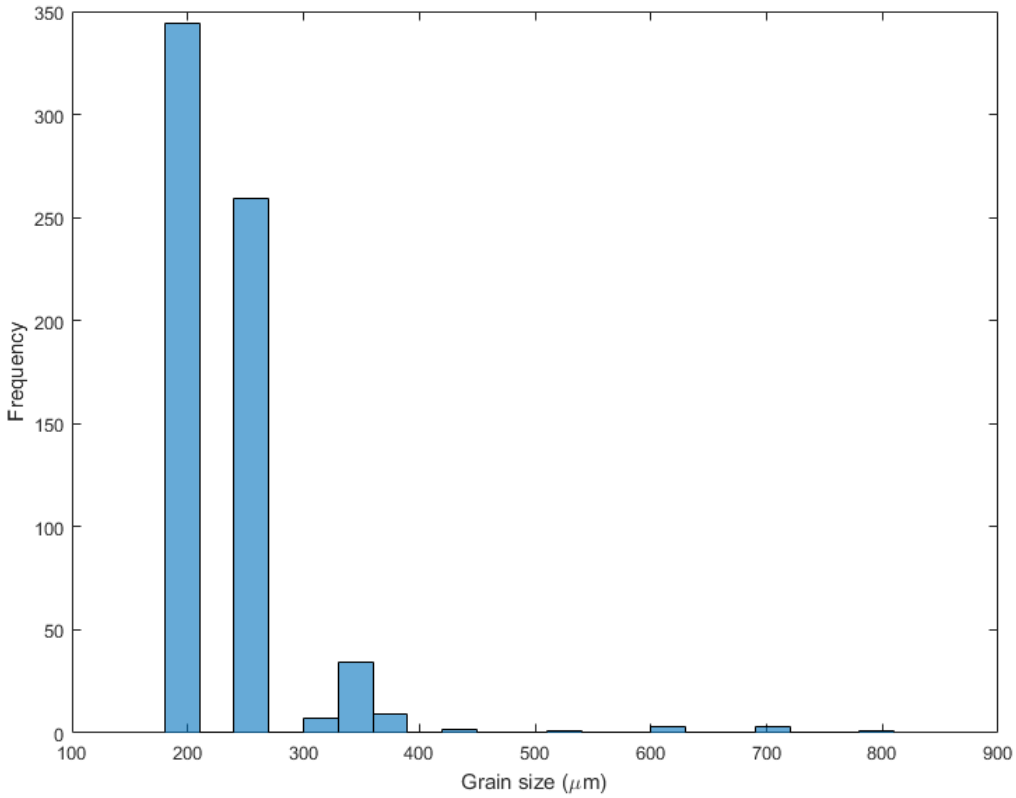

Figure A.7. Grain size distribution of JP15-KnE-02A.

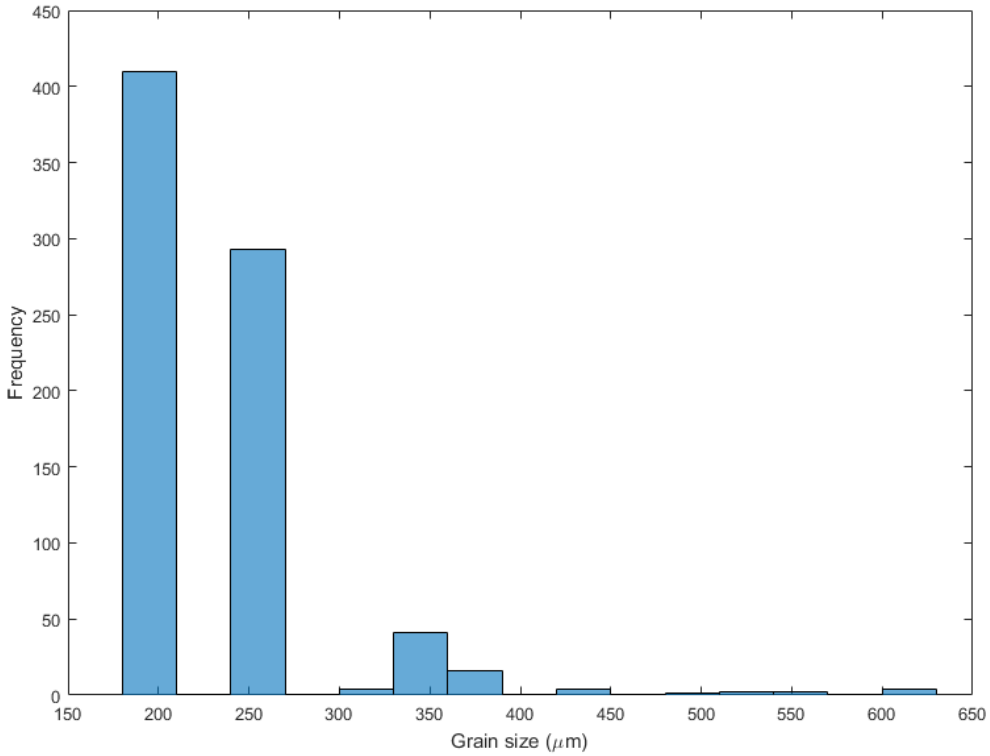

Figure A.8. Grain size distribution of JP15-KnE-04A.

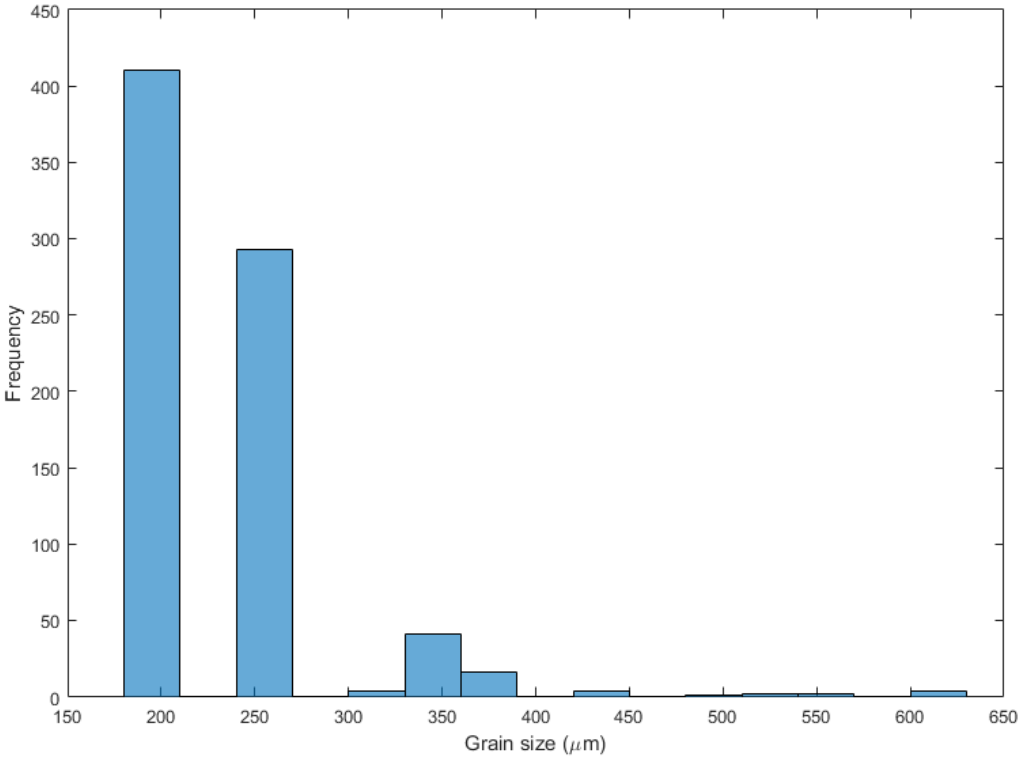

Figure A.9. Grain size distribution of JP15-KnE-06A.

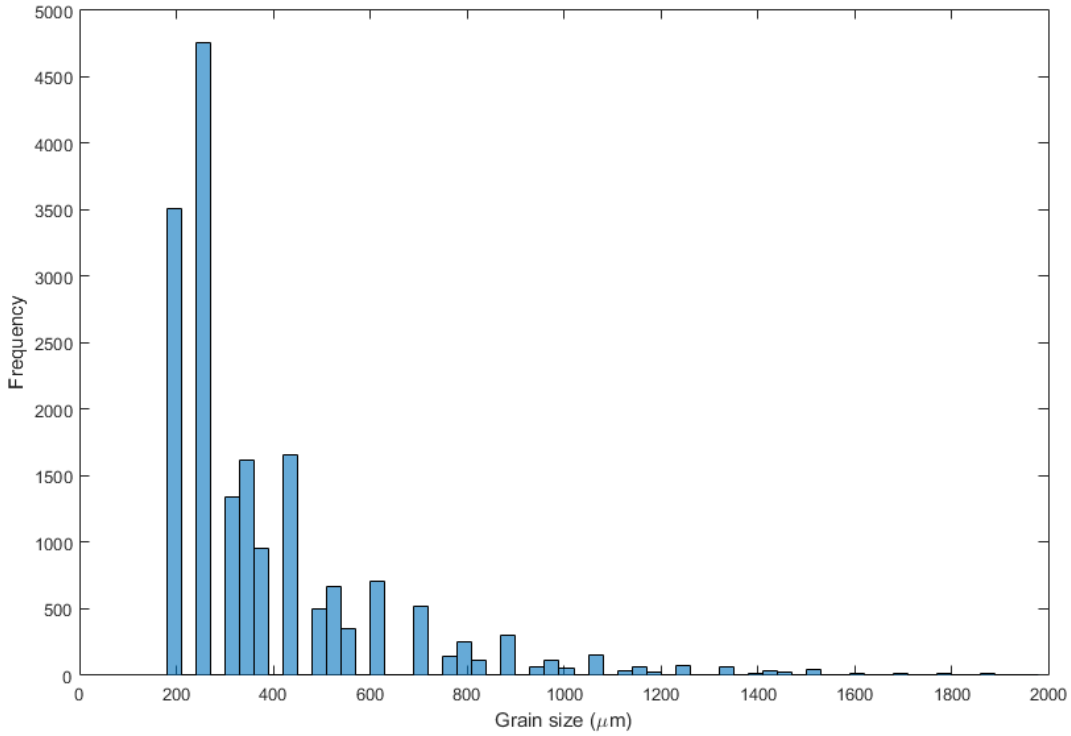

Figure A.10. Grain size distribution of JP15-KnE-07A.

Appendix B. Shear plane foliation measurements and calculations

Plotting samples in the kinematic reference frame requires spatial reorientation of samples and foliation data. This process rotates coordinates so the shear plane is oriented E-W and vertically and the thin section plane is oriented horizontally. Original spatial coordinates are initially input so that *x* is east, *y* is north, and *z* is up. These values correspond to, respectively, strike of angle θ (angle counter-clockwise from east), elevation angle φ, and R, set to equal 1 for all. For all following calculations, we use the plane normal to shear, not the shear plane itself; γ is the strike of this plane and β is the dip. All these data are imported into MATLAB using the structural data script by Jessica Warren ("Josephine Shear Zone Structural Data," 2006; edited 2014, Katie Kumamoto). Sample location data are entered into a matrix of the form

$$Q_0 = [\theta \quad \varphi \quad R] \qquad (B1)$$

Matrix P_0 is created from Q_0 by converting from spherical to Cartesian coordinates, rotating the data clockwise around the z-axis so the shear plane is oriented E-W, and counterclockwise around the y-axis so the thin section plane is horizontal. Then the rotated P_0 is multiplied by the rotation matrix

$$\begin{bmatrix} cos\,\gamma\,cos\,\beta & -sin\,\gamma\,cos\,\beta & sin\,\beta \\ sin\,\gamma & cos\,\gamma & 0 \\ -cos\,\gamma\,sin\,\beta & sin\,\gamma\,sin\,\beta & cos\,\beta \end{bmatrix} \quad (B2)$$

to get P_R. Q_0 is also multiplied by B2 to get Q_R , producing new rotated θ_R and φ_R.

The newly-rotated data is ready for projection, which is done by calculating the intersection of the pyroxene foliation plane with the thin section plane. We take the cross product of the plane normal to the pyroxene foliation plane and the plane normal to the thin section plane, to produce a third plane on which the rotated θ_R and φ_R lie. These final data can be output and used to create kinematic cross sections in the X-Z reference frame, in which X is parallel to the shear plane (θ_R) and Z is normal to the shear plane (φ_R).

Appendix C. Numerical model methods

C.1 Discretization

C.1.1 Conservation of energy

$$\nabla \cdot (k\nabla T) + \rho h = \rho c_p(\frac{\partial T}{\partial t} + u \cdot \nabla T) \quad (C1)$$

$$\frac{\partial}{\partial x}(k\nabla T) + \rho h = \rho c_p \left(\frac{\partial T}{\partial t} + u\left(\frac{\partial T}{\partial x}\right)\right) \quad (C2)$$

$$\frac{\partial}{\partial x}\left(k\frac{\partial T}{\partial x}\right) + \rho h = \rho c_p \left(\frac{\partial T}{\partial t}\right) \quad (C3)$$

$$\frac{\partial}{\partial x}\left(k\frac{T_{i+1}^{t+1} - T_i^{t+1}}{\partial x} - k\frac{T_i^{t+1} - T_{i-1}^{t+1}}{\partial x}\right) + \rho h = \rho c_p \left(\frac{T_i^{t+1} - T_i^t}{\partial t}\right) \quad (C4)$$

$$\left(\frac{\partial k}{\partial x}\frac{T_{i+1}^{t+1} - T_i^{t+1}}{\partial x} - \frac{\partial k}{\partial x}\frac{T_i^{t+1} - T_{i-1}^{t+1}}{\partial x}\right) + \rho h = \rho c_p \left(\frac{T_i^{t+1} - T_i^t}{\partial t}\right) \quad (C5)$$

$$k_A = \frac{k_{i+1} + k_i}{2}, \quad k_B = \frac{k_i + k_{i-1}}{2} \quad (C6)$$

$$\left(\frac{k_A}{\partial x}\frac{T_{i+1}^{t+1} - T_i^{t+1}}{\partial x} - \frac{k_B}{\partial x}\frac{T_i^{t+1} - T_{i-1}^{t+1}}{\partial x}\right) + \rho h = \rho c_p \left(\frac{T_i^{t+1} - T_i^t}{\partial t}\right) \quad (C7)$$

$$\left(\frac{k_A}{\partial x}\frac{T_{i+1}^{t+1} - T_i^{t+1}}{\partial x} - \frac{k_B}{\partial x}\frac{T_i^{t+1} - T_{i-1}^{t+1}}{\partial x}\right) + \rho h = \rho c_p \left(\frac{T_i^{t+1} - T_i^t}{\partial t}\right) \quad (C8)$$

$$T_{i+1}^{t+1}\left(\frac{k_A}{\partial x^2}\right) + T_i^{t+1}\left(\frac{-k_A}{\partial x^2}\right) + T_i^{t+1}\left(\frac{-k_B}{\partial x^2}\right) + T_{i-1}^{t+1}\left(\frac{k_B}{\partial x^2}\right) + \rho h = T_i^{t+1}\left(\frac{\rho c_p}{\partial t}\right) + T_i^t\left(\frac{-\rho c_p}{\partial t}\right) \quad (C9)$$

$$T_{i+1}^{t+1}\left(\frac{k_A}{\partial x^2}\right) + T_i^{t+1}\left(\frac{-k_A - k_B}{\partial x^2}\right) + T_{i-1}^{t+1}\left(\frac{k_B}{\partial x^2}\right) + \rho h = T_i^{t+1}\left(\frac{\rho c_p}{\partial t}\right) + T_i^t\left(\frac{-\rho c_p}{\partial t}\right) \quad (C10)$$

$$T_{i+1}^{t+1}\left(\frac{k_A}{\partial x^2}\right) + T_i^{t+1}\left(\frac{-k_A - k_B}{\partial x^2}\right) + T_{i-1}^{t+1}\left(\frac{k_B}{\partial x^2}\right) + T_i^{t+1}\left(\frac{-\rho c_p}{\partial t}\right) + \rho h = T_i^t\left(\frac{-\rho c_p}{\partial t}\right) \quad (C11)$$

$$T_i^t\left(\frac{\rho c_p}{\partial t}\right) = T_{i+1}^{t+1}\left(\frac{-k_A}{\partial x^2}\right) + T_i^{t+1}\left(\frac{k_A+k_B}{\partial x^2}\right) + T_{i-1}^{t+1}\left(\frac{-k_B}{\partial x^2}\right) + T_i^{t+1}\left(\frac{\rho c_p}{\partial t}\right) - \rho h \quad (C12)$$

$$T_i^t\left(\frac{\rho c_p}{\partial t}\right) + \rho h = T_{i+1}^{t+1}\left(\frac{-k_A}{\partial x^2}\right) + T_i^{t+1}\left(\frac{k_A+k_B}{\partial x^2} + \frac{\rho c_p}{\partial t}\right) + T_{i-1}^{t+1}\left(\frac{-k_B}{\partial x^2}\right) \quad (C13)$$

C.1.2 Conservation of momentum

$$\nabla \cdot \sigma + \rho \vec{g} = 0 \quad (C14)$$

$$\nabla \cdot \sigma = 0 \quad (C15)$$

$$\frac{\partial \sigma_1}{\partial x} + \frac{\partial \sigma_2}{\partial y} + \frac{\partial \sigma_3}{\partial z} = 0 \quad (C16)$$

$$\frac{\partial \sigma_1}{\partial x} = 0 \quad (C17)$$

$$\frac{\partial \sigma_{xx}}{\partial x} + \frac{\partial \sigma_{xy}}{\partial y} = 0 \quad (C18)$$

$$\frac{\partial \sigma_{xx}}{\partial x} = 0 \quad (C19)$$

$$\sigma = 2\eta\dot{\varepsilon}_{ij}\,, \qquad \dot{\varepsilon}_{ij} = \frac{1}{2}\left(\frac{\partial u_i}{\partial x_j}\right) \quad (C20)$$

$$\frac{\partial}{\partial x}\left(\eta\frac{\partial u}{\partial x}\right) = 0 \quad (C21)$$

$$\frac{\partial \eta}{\partial x}\frac{u_{i+1}^{t+1} - u_i^{t+1}}{\partial x} - \frac{\partial \eta}{\partial x}\frac{u_i^{t+1} - u_{i-1}^{t+1}}{\partial x} = 0 \quad (C22)$$

$$\eta_A = \frac{\eta_{i+1}+\eta_i}{2}\,, \quad \eta_B = \frac{\eta_i+\eta_{i-1}}{2} \quad (C23)$$

$$\frac{\eta_A}{\partial x}\frac{u_{i+1}^{t+1} - u_i^{t+1}}{\partial x} - \frac{\eta_B}{\partial x}\frac{u_i^{t+1} - u_{i-1}^{t+1}}{\partial x} = 0 \quad (C24)$$

$$u_{i+1}^{t+1}\left(\frac{\eta_A}{\partial x^2}\right) + u_i^{t+1}\left(\frac{-\eta_A}{\partial x^2}\right) + u_i^{t+1}\left(\frac{-\eta_B}{\partial x^2}\right) + u_{i-1}^{t+1}\left(\frac{\eta_B}{\partial x^2}\right) = 0 \quad (C25)$$

$$u_{i+1}^{t+1}\left(\frac{\eta_A}{\partial x^2}\right) + u_i^{t+1}\left(\frac{-\eta_A-\eta_B}{\partial x^2}\right) + u_{i-1}^{t+1}\left(\frac{\eta_B}{\partial x^2}\right) = 0 \quad (C26)$$

C.1.3 Conservation of volume

$$\nabla \cdot \vec{u} = 0 \quad (C27)$$

$$\frac{\partial u_1}{\partial x} + \frac{\partial u_2}{\partial y} + \frac{\partial u_3}{\partial z} = 0 \quad (C28)$$

$$\frac{\partial u_1}{\partial x} = 0 \quad (C29)$$

$$\frac{u_{i+1}^{t+1}-u_i^{t+1}}{\partial x}=0 \quad \text{(C30)}$$

C.1.4 Viscosity

$$\eta = A\left(\frac{d_0}{b}\right)^{\frac{m}{n}}(\dot{\varepsilon_{II}})^{\frac{1-n}{n}}exp(\frac{-E_a}{nRT}) \quad \text{(C31)}$$

$$\dot{\varepsilon}_{II}=\left[\frac{1}{2}\sum_{ij}\dot{\varepsilon}_{ij}\dot{\varepsilon}_{ij}\right]^{\frac{1}{2}} \quad \text{(C32)}$$

$$\dot{\varepsilon}_{II}=\frac{1}{2}\left(\varepsilon_{xx}^2+\varepsilon_{yy}^2+2\varepsilon_{xy}^2\right)^{\frac{1}{2}} \quad \text{(C33)}$$

$$\dot{\varepsilon}_{II}=\varepsilon_{xy}=\frac{\partial u}{\partial x} \quad \text{(C34)}$$

$$\eta_{eff}=\left(\frac{1}{\eta_{disl}}+\frac{1}{\eta_{diff}}\right)^{-1} \quad \text{(C35)}$$

C.1.5 Shear heating

$$h=\tau_{xy}\frac{\partial u}{\partial x} \quad \text{(C36)}$$

$$\tau=\eta\frac{\partial u}{\partial x} \quad \text{(C37)}$$

$$h=\eta\left(\frac{\partial u}{\partial x}\right)^2 \quad \text{(C38)}$$

$$h=\eta\left(\frac{u_{i+1}^{t+1}-u_{i-1}^{t+1}}{2\partial x}\right)^2 \quad \text{(C39)}$$

C.1.6 Steady-state diffusion

$$\frac{\partial C}{\partial t}=D\frac{\partial^2 C}{\partial x^2} \quad \text{(C40)}$$

$$\frac{C_i^{t+1}-C_i^t}{\partial t}=D\left(\frac{C_{i+1}^{t+1}-C_i^{t+1}}{\partial x^2}-\frac{C_i^{t+1}-C_{i-1}^{t+1}}{\partial x^2}\right) \quad \text{(C41)}$$

$$\frac{C_i^{t+1}-C_i^t}{\partial t}=D\left(\frac{C_{i+1}^{t+1}-2C_i^{t+1}+C_{i-1}^{t+1}}{\partial x^2}\right) \quad \text{(C42)}$$

$$\frac{-C_i^t}{\partial t}=D\left(\frac{C_{i+1}^{t+1}-2C_i^{t+1}+C_{i-1}^{t+1}}{\partial x^2}\right)-\frac{C_i^{t+1}}{\partial t} \quad \text{(C43)}$$

$$\frac{C_i^t}{\partial t} = D\left(\frac{-C_{i+1}^{t+1}+2C_i^{t+1}-C_{i-1}^{t+1}}{\partial x^2}\right) + \frac{C_i^{t+1}}{\partial t} \quad (C44)$$

$$C_i^t = D\partial t\left(\frac{-C_{i+1}^{t+1}+2C_i^{t+1}-C_{i-1}^{t+1}}{\partial x^2}\right) + C_i^{t+1} \quad (C45)$$

$$C_i^t = C_{i+1}^{t+1}\left(\frac{-D\partial t}{\partial x^2}\right) + C_i^{t+1}\left(\frac{2D\partial t}{\partial x^2}+1\right) + C_{i-1}^{t+1}\left(\frac{-D\partial t}{\partial x^2}\right) \quad (C46)$$

C.2 Benchmarking

We benchmark our heat and composition diffusion equations by comparing our results with the solution for instantaneous heating of a semi-infinite half-space (*Turcotte and Schubert*, 2002; 4.15) to test the accuracy of our thermal and helium diffusion terms. Because both terms are calculated using the same mathematical structure, we can also apply the instantaneous heating model to diffusion of helium. We solve for each variable over a domain of 5000 nodes.

C.2.1 Thermal diffusion

Similar to the conservation of energy, the law governing instantaneous heating of a half-space is

$$\frac{\partial\theta}{\partial t} = \kappa\frac{\partial^2\theta}{\partial x^2} \quad (C47)$$

where t is time, κ is thermal diffusivity, x is distance, and θ is nondimensional temperature, defined as

$$\theta = \frac{T-T_1}{T_0-T_1}, \quad (C48)$$

where T_1 is the initial temperature, T_0 is the maximum temperature, and T is the current temperature. The characteristic thermal diffusion distance, $\sqrt{\kappa t}$, appears in the similarity variable

$$\xi = \frac{x}{2\sqrt{\kappa t}}. \quad (C49)$$

We can relate nondimensional temperature θ and ξ by

$$\theta = 1 - erf(\xi) = \text{erfc}(\xi). \quad (C50)$$

Substituting the definition of θ into equation C50, we have

$$\frac{T-T_1}{T_0-T_1} = \text{erfc}\left(\frac{x}{2\sqrt{\kappa t}}\right). \quad (C51)$$

Rearranging equation C50 to solve for T, we have

$$T = (T_0 - T_1)\text{erfc}\left(\frac{x}{\sqrt{\kappa t}}\right) + T_1, \qquad \text{(C52)}$$

which allows us to solve for the expected temperature across domain *x* for time *t*.

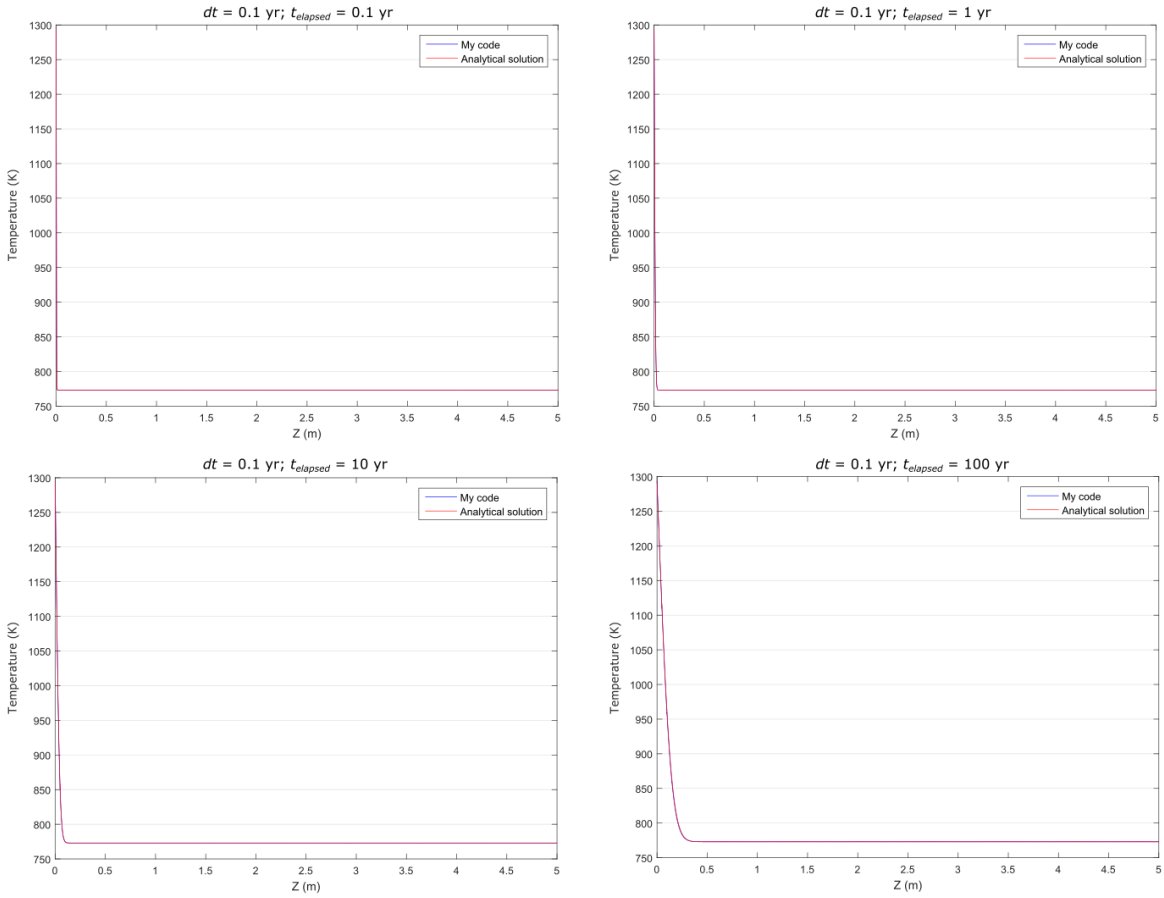

Figure C.1. Thermal solution of Turcotte and Schubert (2002) compared to our thermal solver at a distance of 5 m from the shear zone center over varying time scales.

C.2.2 Helium diffusion

The procedure in C.2.1 can be applied to helium diffusion if we assign

$$\varsigma = \frac{C - C_1}{C_0 - C_1}, \qquad \text{(C53)}$$

where C_1 is the initial helium concentration, C_0 is the maximum concentration, and C is the current concentration. Then

$$\frac{\partial \varsigma}{\partial t} = D\frac{\partial^2 \sigma}{\partial x^2} \qquad \text{(C54)}$$

The remaining equations are similar, using the appropriate variables:

$$\varphi = \frac{x}{2\sqrt{Dt}}, \tag{C55}$$

$$\varsigma = 1 - erf(\varphi) = \text{erfc}(\varphi), \tag{C56}$$

$$\frac{C - C_1}{C_0 - C_1} = \text{erfc}\left(\frac{x}{2\sqrt{Dt}}\right), \tag{C57}$$

and

$$C = (C_0 - C_1)\text{erfc}\left(\frac{x}{\sqrt{Dt}}\right) + C_1. \tag{C58}$$

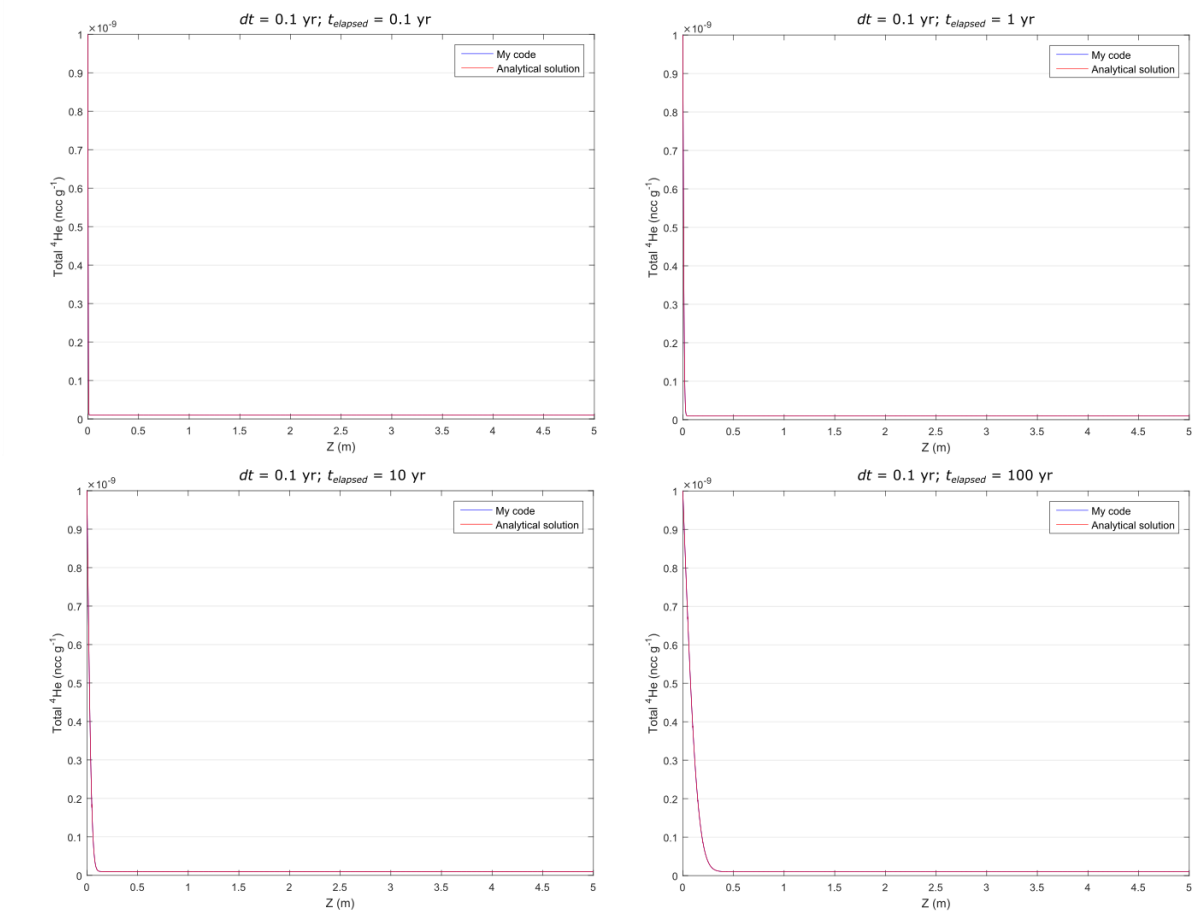

Figure C.2. Diffusion solution based on Turcotte and Schubert (2002) compared to our diffusion solver at a distance of 5 m from the shear zone center over varying time scales.

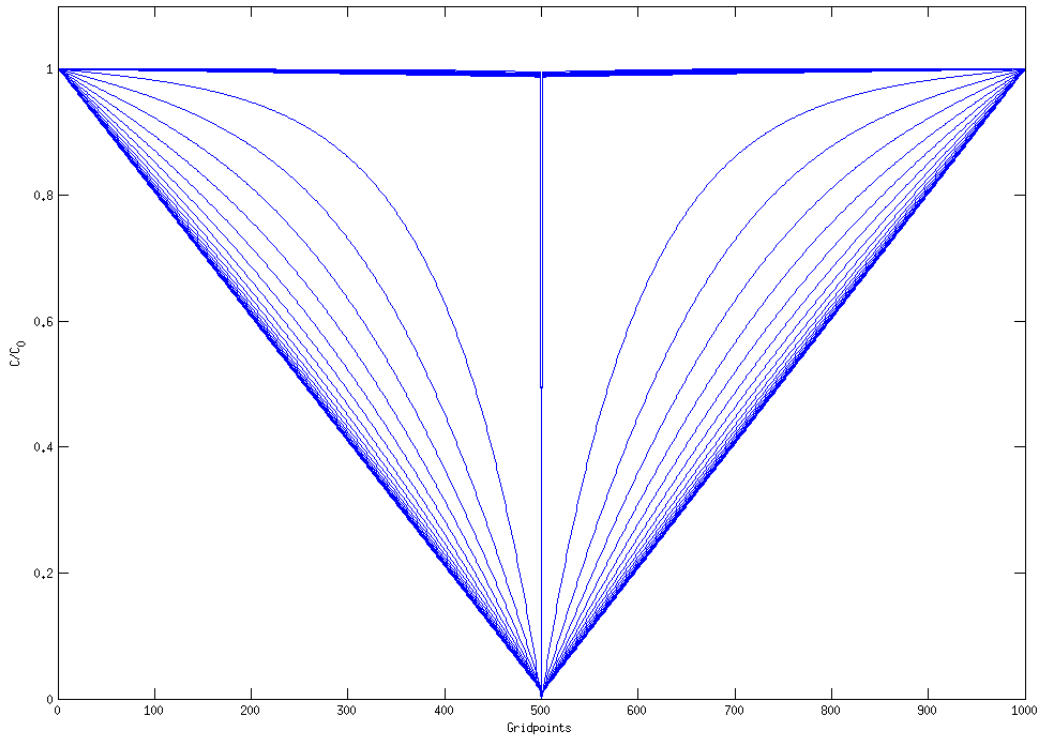

Figure C.3. Total ^{4}He during one Picard iteration (u_x = 1.5 m yr^{-1}) to evaluate the behavior of total helium diffusion. This experiment demonstrates that total ^{4}He localizes during each iteration to produce the steadily decreasing profile seen in model runs (Fig. 36).

Appendix D. Helium data and parameters

Table D.1. Total helium data and concentrations from SZ A and SZ B.

Sample	Weight (g)	Date and Time	^{4}He (ncc)	^{3}He/^{4}He (R/Ra)	Sigma	^{4}He (cc STP)	^{4}He (cc STP/g)
SZ A							
Crs1-JP15-KnE-01A-25349	0.25349	9/1/2015 19:45	0.96159	6.484	0.119	9.616E-10	3.793E-09
Crs2-JP15-KnE-02A-26948	0.26948	9/1/2015 20:21	0.49246	6.378	0.145	4.925E-10	1.827E-09
Crs3-JP15-KnE-03A-24881	0.24881	9/1/2015 20:55	0.35089	6.479	0.167	3.509E-10	1.410E-09
Crs1-JP15-KnE-04A-cp-21881	0.21881	9/4/2015 19:53	2.89895	6.736	0.098	2.899E-09	1.325E-08
Crs2-JP15-KnE-05A-cp-21629	0.21629	9/4/2015 20:29	0.75731	6.276	0.135	7.573E-10	3.501E-09
Crs3-JP15-06A-cp-25520	0.2552	9/4/2015 21:04	0.71853	6.394	0.122	7.185E-10	2.816E-09
Crs1-JP15-KnE-07A-23919	0.23919	9/11/2015 11:47	1.49256	6.557	0.109	1.493E-09	6.240E-09
Fur-p2-JP15-KnE-01A-24716	0.24716	9/23/2015 10:22	15.90944	7.396	0.091	1.591E-08	6.437E-08
Fur-p3-JP15-KnE-02A-25913	0.25913	9/23/2015 13:52	6.26074	9.496	0.119	6.261E-09	2.416E-08
Fur-p4-JP15-KnE-03A-24049	0.24049	9/24/2015 7:22	7.17061	9.004	0.115	7.171E-09	2.982E-08
Fur-p5-JP15-KnE-04A-21317	0.21317	9/24/2015 9:07	19.79574	7.632	0.093	1.980E-08	9.286E-08
Fur-p6-JP15-KnE-05A-26721	0.26721	9/24/2015 12:37	12.89802	6.514	0.081	1.290E-08	4.827E-08
Fur-p7-JP15-KnE-06A-24669	0.24669	9/24/2015 14:22	8.75845	9.008	0.113	8.758E-09	3.550E-08
Fur-p8-JP15-KnE-07A-22842	0.22842	9/25/2015 9:02	15.62265	7.891	0.097	1.562E-08	6.839E-08
SZ B							
Crs1-JP13-D35-24293	0.24293	9/29/2015 3:21	1.49027	6.808	0.111	1.490E-09	6.135E-09
Crs2-JP13-D37-25654	0.25654	9/29/2015 3:57	1.52564	6.591	0.107	1.526E-09	5.947E-09
Crs3-JP13-D39-27651	0.27651	9/29/2015 4:32	1.09188	6.447	0.117	1.092E-09	3.949E-09
Crs1-JP13-D34-25871	0.25871	9/30/2015 2:42	0.38076	5.422	0.163	3.808E-10	1.472E-09
Crs2-JP13-D36-25543	0.25543	9/30/2015 3:17	0.4819	6.605	0.152	4.819E-10	1.887E-09
Crs3-JP13-D38-29732	0.29732	9/30/2015 3:53	1.0508	6.278	0.118	1.051E-09	3.534E-09
Crs1-JP13-D41-26602	0.26602	9/30/2015 20:12	0.58374	6.119	0.131	5.837E-10	2.194E-09
Crs2-JP13-D43-29059	0.29059	9/30/2015 20:48	0.55794	6.129	0.140	5.579E-10	1.920E-09
Crs3-JP13-D44-27466	0.27466	9/30/2015 21:23	0.71655	5.973	0.124	7.166E-10	2.609E-09
Crs1-JP13-D40-24460	0.2446	10/2/2015 18:20	0.50223	6.567	0.150	5.022E-10	2.053E-09
Crs2-JP13-D42-26054	0.26054	10/2/2015 18:54	0.63872	5.845	0.132	6.387E-10	2.452E-09
Crs3-JP13-D45-30785	0.30785	10/2/2015 19:29	1.00623	6.113	0.115	1.006E-09	3.269E-09
Fur-p2-JP13-D34-24817	0.24817	10/5/2015 15:11	2.9342	13.715	0.178	2.934E-09	1.182E-08
Fur-p3-JP13-D35-23227	0.23227	10/5/2015 16:56	8.35181	9.620	0.119	8.352E-09	3.596E-08
Fur-p4-JP13-D36-24800	0.248	10/6/2015 9:51	3.81192	14.193	0.180	3.812E-09	1.537E-08
Fur-p5-JP13-D37-24605	0.24605	10/6/2015 11:36	9.75783	9.043	0.112	9.758E-09	3.966E-08
Fur-p6-JP13-D38-28674	0.28674	10/6/2015 13:22	21.02161	5.316	0.065	2.102E-08	7.331E-08
Fur-p7-JP13-D39-26610	0.2661	10/6/2015 15:07	9.18532	8.075	0.102	9.185E-09	3.452E-08
Fur-p8-JP13-D41-25765	0.25765	10/7/2015 15:02	6.40296	9.824	0.125	6.403E-09	2.485E-08
Fur-p9-JP13-D44-26563	0.26563	10/8/2015 11:39	6.00253	9.660	0.122	6.003E-09	2.260E-08
Fur-p2-JP13-D40-23534	0.23534	10/20/2015 10:19	3.8571	11.669	0.151	3.857E-09	1.639E-08
Fur-p3-JP13-D42-25099	0.25099	10/20/2015 13:49	11.0427	7.891	0.095	1.104E-08	4.400E-08
Fur-p4-JP13-D43-27684	0.27684	10/20/2015 16:09	5.23585	10.967	0.136	5.236E-09	1.891E-08
Fur-p5-JP13-D45-29708	0.29708	10/21/2015 9:40	7.54912	10.968	0.137	7.549E-09	2.541E-08

Table D.2. Diffusion properties of helium in olivine from various analytical studies.

Source	**Helium partition coefficient K_{He}**	**Activation Energy E** (kJ/mol)	**Diffusion coefficient D_0** ($m^2 s^{-1}$)	**Calculated diffusion coefficient D** at 1373 K ($m^2 s^{-1}$)	**Grain boundary width δ** (nm)
Baxter et al., 2007	4E-6 - 4E-5				0.38, 1-5
Blard et al., 2008		127	8.2E-7 - 9.6E-7	8.11E-7 - 9.49E-7	
Cherniak and Watson, 2012		135	3.73E-08	3.69E-08	
Dohmen and Milke, 2010					1
Futagami et al., 1993		130	1.40E-08	1.38E-08	
Hart, 1984		502	1.00E-06	9.57E-07	
Heber et al., 2007	3.5E-4 - 1.4E-3	420	1.70E-02	1.80E-18	0.75
Jackson et al., 2013	3.8E-5 - 9.8 E-4				
Parman et al., 2005	7E-4 - 2.5E-3				
Shuster et al., 2004		140-154	6.10E-07	6.20E-07	
Tolstikhin et al., 2010		133	2.40E-06	2.37E-06	
Trull et al., 1991	6.00E-06	105	2.00E-08	1.98E-08	
Trull and Kurz, 1993	1.00E-05	420	9.08E-08	8.75E-08	
Wang et al., 2015		128	2.42E-07	2.39E-07	

Table D.3. Nondimensionalized values of parameters in Table 2 used in our model.

Symbol	Nondimensionalized units	Scaling Factor
A_{disl}	9×10^{3} Pa s^{-ndisl}	$x_0\ \eta_0^{-1}\ u_0^{-1}\ (u_0\ x_0^{-1})^{-ndl}$
A_{diff}	7.8×10^{-1} Pa s	η_0^{-1}
B_{disl}	1×10^{5} Pa^{-ndisl} s^{-1}	$x_0\ u_0^{-1}\ (u_0\ \eta_0\ x_0^{-1})^{ndl}$
B_{diff}	7.6×10^{-9} m^{mdiff} Pa^{-ndiff} s^{-1}	$x_0^{-m}\ x_0\ u_0^{-1}\ (u_0\ \eta_0\ x_0^{-1})^{ndl}$
b	6×10^{-10} m	x_0^{-1}
C_i	1×10^{-11} cc kg^{-1}	C_0^{-1}
cp	1300 J kg^{-1} K^{-1}	$T_0\ u_0^{-2}$
d_0	1000 µm	x_0^{-1}
d	m s^{-1}	u_0^{-1}
D_0	1×10^{-7} m^2 s^{-1}	$x_0^{-1}\ u_0^{-1}$
$D_{0\ LAT}$	1.15×10^{-8} m^2 s^{-1}	$x_0^{-1}\ u_0^{-1}$
$D_{0\ GB}$	2.5×10^{-12} m^2 s^{-1}	$x_0^{-1}\ u_0^{-1}$
D	m s^{-1}	u_0^{-1}
D_{LAT}	m s^{-1}	u_0^{-1}
D_{GB}	m s^{-1}	u_0^{-1}
δ	$1 - 5 \times 10^{-9}$ m	x_0^{-1}
ε	$10^{-10} - 10^{-14}$ s^{-1}	$x_0\ u_0^{-1}$
ε_{II}	s^{-1}	$x_0\ u_0^{-1}$
G	8×10^{-27} m^n s^{-1}	$x_0^{-p}\ x_0\ u_0^{-1}$
h	W m^{-3}	$x_0^2\ \eta_0^{-1}\ u_0^{-2}$
k	3.3×10^{-4} W m^{-1} K^{-1}	$T_0\ \eta_0^{-1}\ u_0^{-2}$
κ	7.92×10^{-11} m^2 s^{-1}	$x_0^{-1}\ u_0^{-1}$
η	10^{21} Pa s	η_0^{-1}
ρ	3200 kg m^{-3}	$u_0\ x_0^{-1}\ \eta_0^{-1}$
σ	Pa	$x_0\ \eta_0^{-1}\ u_0^{-1}$
T_0	773 K	T_0^{-1}
t	s	$u_0\ x_0^{-1}$
u	m s^{-1}	u_0^{-1}
μ	8.13×10^{10} Pa	$x_0\ \eta_0^{-1}\ u_0^{-1}$
V_{GB}	5.8×10^{-12} m^3	x_0^{-3}
V_{LAT}	5.2×10^{-10} m^3	x_0^{-3}
x	m	x_0^{-1}

Appendix E. Helium closure temperature

We calculate the closure temperature of helium to estimate the conditions at which helium becomes immobile within a material. The Dodson equation (*Dodson*, 1973) describes the closure temperature as a time-dependent range of temperatures and can be applied to any gas species within any mineral phase (in our case, helium in olivine):

$$T_c = \frac{E_a/R}{\ln\left(\frac{ART_c^2(D_0/a^2)}{E_a\left(\frac{dT}{dt}\right)}\right)},$$

where E_a is activation energy of helium in the specified mineral, R is the universal gas constant, A is a geometric factor (55, assuming a spherical grain), D_0 is the diffusion coefficient of helium, a is the effective diffusion radius (i.e. grain radius), dT/dt is the cooling rate in ºC Ma^{-1} (*Baxter*, 2010). We use an effective E_a of 1.37×10^5 J mol^{-1} and D_0 of 1×10^7 m^2 s^{-1} (table 2) and estimate an initial cooling rate of 20 ºC Ma^{-1}. Grain radius a will vary depending on extent of deformation and proximity to the shear zone center; grain size of 230 μm has a closure temperature of 224 ºC and grain size of 1000 μm has a closure temperature of 273 ºC.